Fundamental and functional properties associated to exotic phase transitions in novel rare earth based intermetallic compounds and Heusler alloys

By

MANTU MODAK

Enrolment No: PHYS05201504003

Saha Institute of Nuclear Physics, Kolkata

A thesis submitted to the

Board of Studies in Physical Sciences

In partial fulfillment of requirements

for the Degree of

DOCTOR OF PHILOSOPHY

of

HOMI BHABHA NATIONAL INSTITUTE

August, 2020

Homi Bhabha National Institute

Recommendations of the Viva Voce Committee

As members of the Viva Voce Board, we certify that we have read the dissertation prepared by **Mantu Modak** entitled **Fundamental and functional properties associated to exotic phase transitions in novel rare earth based intermetallic compounds and Heusler alloys** and recommend that it maybe accepted as fulfilling the dissertation requirement for the Degree of Doctor of Philosophy.

....**Date:**
Chairman - Prof. Satyaranjan Bhattacharyya

....**Date:** 12/11/20
Guide - Prof. Sangam Banerjee

Biswajit Karmakar...**Date:** 12/11/20
Member 1 - Prof. Biswajit Karmakar

....**Date:**
Member 2 - Prof. Bilwadal Bandyopadhyay

Gayathri N...**Date:** 12/11/2020
Member 3 - Dr. Gayathri N. Banerjee

....**Date:**
Examiner - Prof. A. Srinivasan

Final approval and acceptance of this dissertation is contingent upon the candidate's submission of the final copies of the dissertation to HBNI.

I hereby certify that I have read this dissertation prepared under my direction and recommend that it may be accepted as fulfilling the dissertation requirement.

Date: 12/11/20

Place: SINP, Kolkata Guide: Prof. Sangam Banerjee

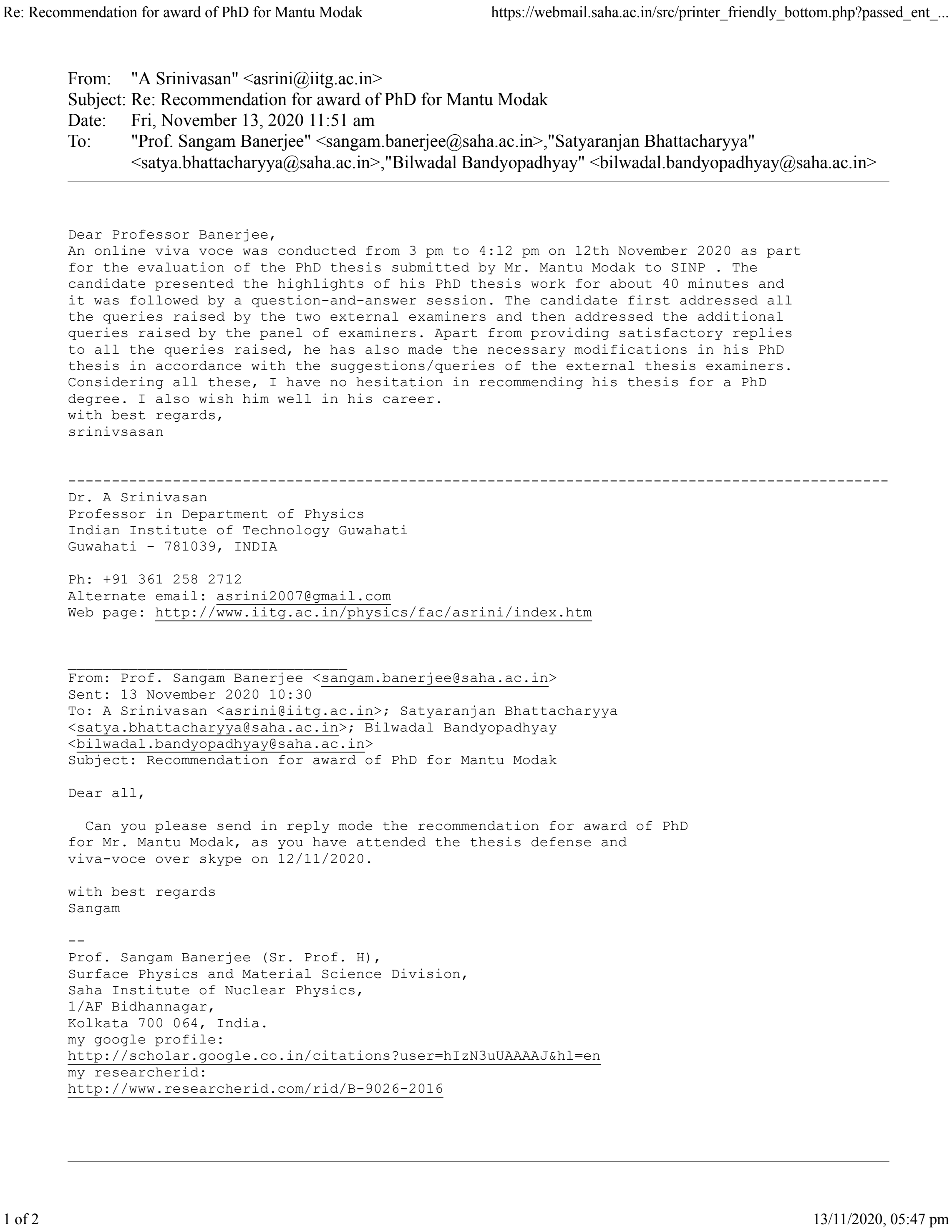

Re: Recommendation for award of PhD for Mantu Modak https://webmail.saha.ac.in/src/printer_friendly_bottom.php?passed_ent_...

From: "A Srinivasan" <asrini@iitg.ac.in>
Subject: Re: Recommendation for award of PhD for Mantu Modak
Date: Fri, November 13, 2020 11:51 am
To: "Prof. Sangam Banerjee" <sangam.banerjee@saha.ac.in>,"Satyaranjan Bhattacharyya" <satya.bhattacharyya@saha.ac.in>,"Bilwadal Bandyopadhyay" <bilwadal.bandyopadhyay@saha.ac.in>

Dear Professor Banerjee,
An online viva voce was conducted from 3 pm to 4:12 pm on 12th November 2020 as part for the evaluation of the PhD thesis submitted by Mr. Mantu Modak to SINP . The candidate presented the highlights of his PhD thesis work for about 40 minutes and it was followed by a question-and-answer session. The candidate first addressed all the queries raised by the two external examiners and then addressed the additional queries raised by the panel of examiners. Apart from providing satisfactory replies to all the queries raised, he has also made the necessary modifications in his PhD thesis in accordance with the suggestions/queries of the external thesis examiners. Considering all these, I have no hesitation in recommending his thesis for a PhD degree. I also wish him well in his career.
with best regards,
srinivsasan

Dr. A Srinivasan
Professor in Department of Physics
Indian Institute of Technology Guwahati
Guwahati - 781039, INDIA

Ph: +91 361 258 2712
Alternate email: asrini2007@gmail.com
Web page: http://www.iitg.ac.in/physics/fac/asrini/index.htm

From: Prof. Sangam Banerjee <sangam.banerjee@saha.ac.in>
Sent: 13 November 2020 10:30
To: A Srinivasan <asrini@iitg.ac.in>; Satyaranjan Bhattacharyya <satya.bhattacharyya@saha.ac.in>; Bilwadal Bandyopadhyay <bilwadal.bandyopadhyay@saha.ac.in>
Subject: Recommendation for award of PhD for Mantu Modak

Dear all,

Can you please send in reply mode the recommendation for award of PhD for Mr. Mantu Modak, as you have attended the thesis defense and viva-voce over skype on 12/11/2020.

with best regards
Sangam

--
Prof. Sangam Banerjee (Sr. Prof. H),
Surface Physics and Material Science Division,
Saha Institute of Nuclear Physics,
1/AF Bidhannagar,
Kolkata 700 064, India.
my google profile:
http://scholar.google.co.in/citations?user=hIzN3uUAAAAJ&hl=en
my researcherid:
http://www.researcherid.com/rid/B-9026-2016

1 of 2 13/11/2020, 05:47 pm

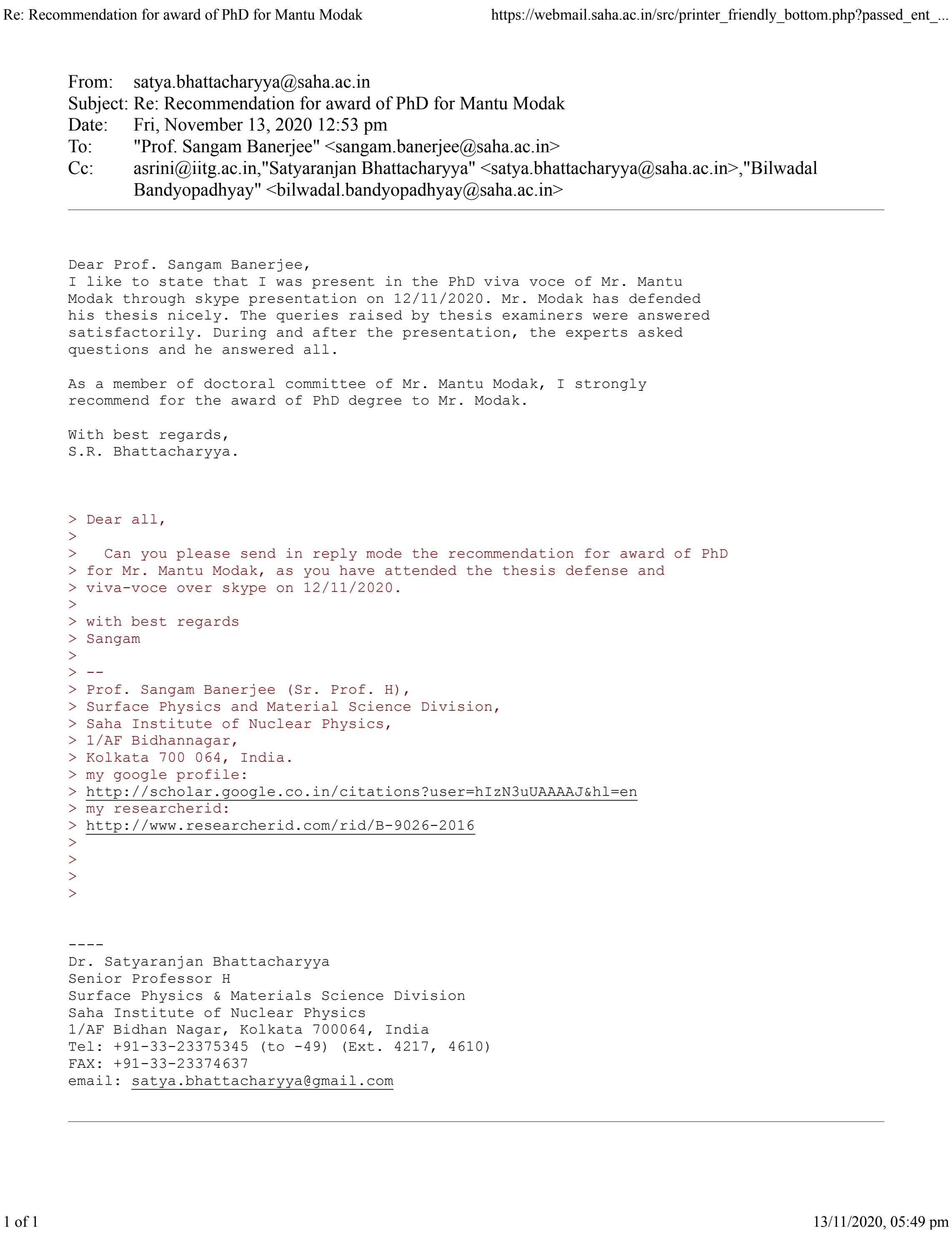

Re: Recommendation for award of PhD for Mantu Modak https://webmail.saha.ac.in/src/printer_friendly_bottom.php?passed_ent_...

From: satya.bhattacharyya@saha.ac.in
Subject: Re: Recommendation for award of PhD for Mantu Modak
Date: Fri, November 13, 2020 12:53 pm
To: "Prof. Sangam Banerjee" <sangam.banerjee@saha.ac.in>
Cc: asrini@iitg.ac.in,"Satyaranjan Bhattacharyya" <satya.bhattacharyya@saha.ac.in>,"Bilwadal Bandyopadhyay" <bilwadal.bandyopadhyay@saha.ac.in>

Dear Prof. Sangam Banerjee,
I like to state that I was present in the PhD viva voce of Mr. Mantu Modak through skype presentation on 12/11/2020. Mr. Modak has defended his thesis nicely. The queries raised by thesis examiners were answered satisfactorily. During and after the presentation, the experts asked questions and he answered all.

As a member of doctoral committee of Mr. Mantu Modak, I strongly recommend for the award of PhD degree to Mr. Modak.

With best regards,
S.R. Bhattacharyya.

> Dear all,
>
> Can you please send in reply mode the recommendation for award of PhD
> for Mr. Mantu Modak, as you have attended the thesis defense and
> viva-voce over skype on 12/11/2020.
>
> with best regards
> Sangam
>
> --
> Prof. Sangam Banerjee (Sr. Prof. H),
> Surface Physics and Material Science Division,
> Saha Institute of Nuclear Physics,
> 1/AF Bidhannagar,
> Kolkata 700 064, India.
> my google profile:
> http://scholar.google.co.in/citations?user=hIzN3uUAAAAJ&hl=en
> my researcherid:
> http://www.researcherid.com/rid/B-9026-2016

Dr. Satyaranjan Bhattacharyya
Senior Professor H
Surface Physics & Materials Science Division
Saha Institute of Nuclear Physics
1/AF Bidhan Nagar, Kolkata 700064, India
Tel: +91-33-23375345 (to -49) (Ext. 4217, 4610)
FAX: +91-33-23374637
email: satya.bhattacharyya@gmail.com

1 of 1 13/11/2020, 05:49 pm

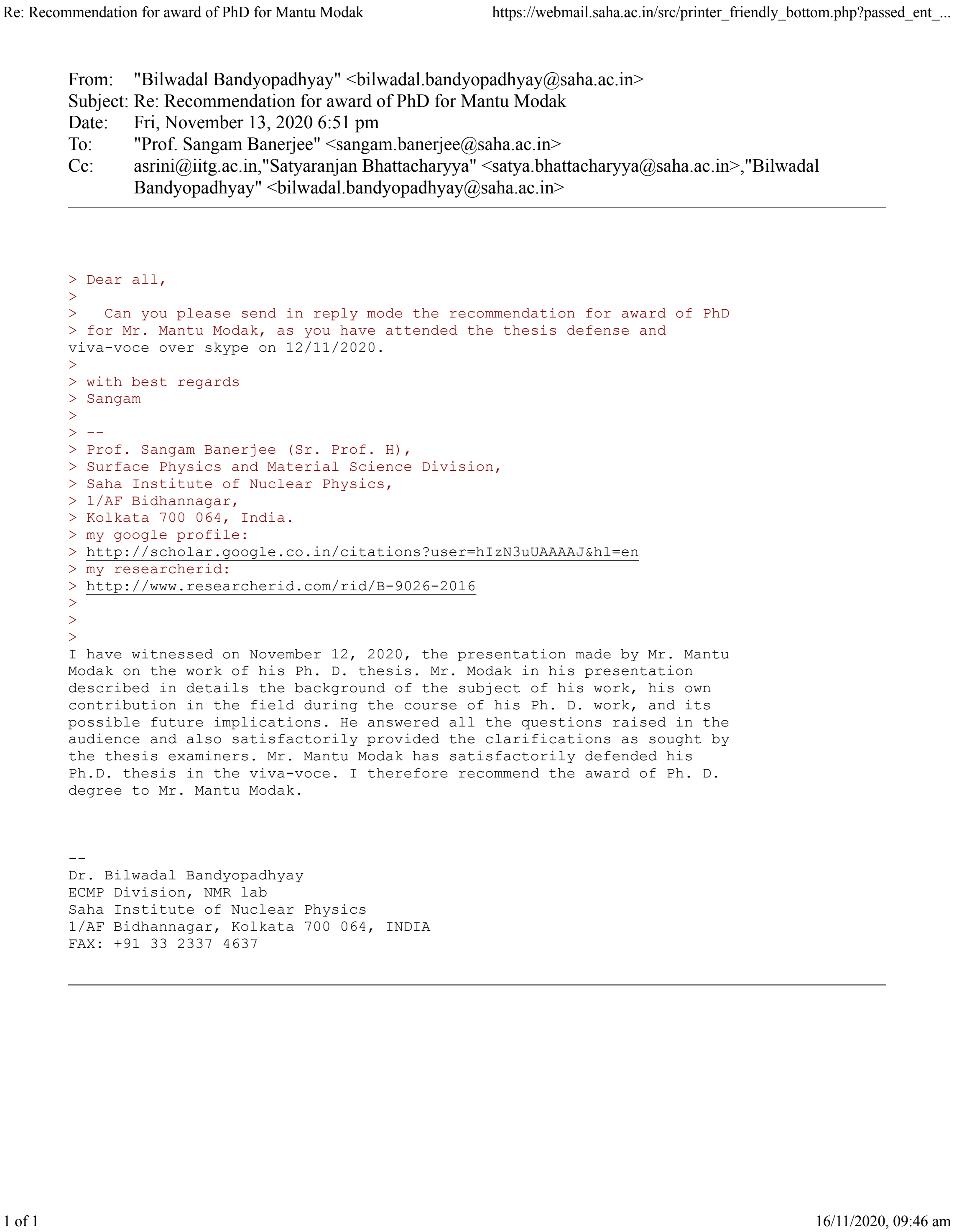

Re: Recommendation for award of PhD for Mantu Modak https://webmail.saha.ac.in/src/printer_friendly_bottom.php?passed_ent_...

From: "Bilwadal Bandyopadhyay" <bilwadal.bandyopadhyay@saha.ac.in>
Subject: Re: Recommendation for award of PhD for Mantu Modak
Date: Fri, November 13, 2020 6:51 pm
To: "Prof. Sangam Banerjee" <sangam.banerjee@saha.ac.in>
Cc: asrini@iitg.ac.in,"Satyaranjan Bhattacharyya" <satya.bhattacharyya@saha.ac.in>,"Bilwadal Bandyopadhyay" <bilwadal.bandyopadhyay@saha.ac.in>

> Dear all,
>
> Can you please send in reply mode the recommendation for award of PhD
> for Mr. Mantu Modak, as you have attended the thesis defense and
viva-voce over skype on 12/11/2020.
>
> with best regards
> Sangam
>
> --
> Prof. Sangam Banerjee (Sr. Prof. H),
> Surface Physics and Material Science Division,
> Saha Institute of Nuclear Physics,
> 1/AF Bidhannagar,
> Kolkata 700 064, India.
> my google profile:
> http://scholar.google.co.in/citations?user=hIzN3uUAAAAJ&hl=en
> my researcherid:
> http://www.researcherid.com/rid/B-9026-2016
>
>
>

I have witnessed on November 12, 2020, the presentation made by Mr. Mantu Modak on the work of his Ph. D. thesis. Mr. Modak in his presentation described in details the background of the subject of his work, his own contribution in the field during the course of his Ph. D. work, and its possible future implications. He answered all the questions raised in the audience and also satisfactorily provided the clarifications as sought by the thesis examiners. Mr. Mantu Modak has satisfactorily defended his Ph.D. thesis in the viva-voce. I therefore recommend the award of Ph. D. degree to Mr. Mantu Modak.

--
Dr. Bilwadal Bandyopadhyay
ECMP Division, NMR lab
Saha Institute of Nuclear Physics
1/AF Bidhannagar, Kolkata 700 064, INDIA
FAX: +91 33 2337 4637

---

1 of 1 16/11/2020, 09:46 am

To
My Parents

STATEMENT BY AUTHOR

This dissertation has been submitted in partial fulfillment of requirements for an advanced degree at Homi Bhabha National Institute (HBNI) and is deposited in the Library to be made available to borrowers under rules of the HBNI.

Brief quotations from this dissertation are allowable without special permission, provided that accurate acknowledgment of source is made. Requests for permission for extended quotation from or reproduction of this manuscript in whole or in part may be granted by the Competent Authority of HBNI when in his or her judgment the proposed use of the material is in the interests of scholarship. In all other instances, however, permission must be obtained from the author.

Mantu Modak

Mantu Modak

DECLARATION

I, hereby declare that the investigation presented in the thesis has been carried out by me. The work is original and has not been submitted earlier as a whole or in part for a degree / diploma at this or any other Institution / University.

Mantu Modak

....

Mantu Modak

List of Publications arising from the thesis

Journal

1. Origin of magnetoresistance across the martensitic transformation: formation of phase fraction, **M. Modak**, M. K. ray, S. Mondal, B. Maji, M. K. Ray K. Bagani, A. Bhattacharyya and S. Banerjee, *J. Phys. D: Appl. Phys.*, **2020**, 53, 205301.
2. Cr doping mimicking the field induced magnetic transition in $ErRu_{2-x}Cr_xSi_2$, **M. Modak**, B. Maji, S. Mondal, M. K. Ray and S. Banerjee, *Physica B: Condensed Matter*, **2019**, 572, 195.
3. Magnetic properties and large reversible magnetocaloric effect in Er_3Pd_2, Bibekananda Maji, Mayukh K. Ray, **M. Modak**, S. Mondal, K. G. Suresh and S. Banerjee, *Journal of Magnetism and Magnetic Materials*, **2018**, 456, 236.
4. Spin-orbital magnetic moment compensation in (Sm,Gd)Ag, **M. Modak**, S. Mondal, B. Maji, M. K. Ray and S. Banerjee *(under preparation)*.

Chapters in books and lectures notes

1. None

Others (not related to thesis)

1. Magnetic behavior of nanostructured $NiTiO_3$ and NiO material: Anomalous increase in coercivity, **M. Modak**, N.Pal, S. Mondal, M. Sardar

and S. Banerjee,
Journal of Magnetism and Magnetic Materials, **2018**, 448, 221.

2. Role of $f - d$ exchange interaction and Kondo scattering in the Nd-doped pyrochlore iridate $(Eu_{1-x}Nd_x)_2Ir_2O_7$, Sampad Mondal, **M. Modak**, B. Maji, Mayukh K. Ray, S. Mandal, Swapan K. Mandal, M. Sardar, S. Banerjee, *Physical Review B*, **2020**, 102, 155139.

3. Spin glass state and field induced ultra-sharp magnetic transitions in Nd_5Ge_2Si, Bibekananda Maji, **M. Modak**, S. Mondal, M. K. Ray and K. G. Suresh, *Physica B: Condensed Matter*, **2019**, 570, 182.

4. Magnetic ground state and giant spontaneous exchange bias in $Ni_{46}Mn_{43}In_{11}$ alloy, Mayukh K. Ray, Bibekananda Maji, **M. Modak** and S. Banerjee, *Journal of Magnetism and Magnetic Materials*, **2017**, 429, 110.

5. Magnetocaloric as a sensitive tool to study magnetic phase in $Ca_4Mn_3O_{10}$, Sampad Mondal, **M. Modak**, M.K. Ray, Swapan K. Mandal, M. Sardar, S. Banerjee,
Journal of Magnetism and Magnetic Materials, **2018**, 448, 292.

6. Can one introduce long range ferromagnetism by doping transition metal in wide band gap semiconducting ZnO? B. Ghosh, K. Bagani, S. Majumder, **M. Modak**, M.K. Ray, M. Sardar, S. Banerjee,
Results in Physics, **2019**, 12, 623.

7. Magnetic and Transport properties of inverse Heusler compound Cr_2CoAl, A. Datta, **M. Modak**, P. Paul, M. M. Patidar, T. V. Chandrasekhar

Rao, V. Ganesan, S. Banerjee, (*accepted in Journal of Magnetism and Magnetic Materials*)

8. Highly Air-Stable Single-Crystalline β-$CsPbI_3$ Nanorods: A Platform for Inverted Perovskite Solar Cells, S. Mahato, A. Ghorai, S. K. Srivastava, **M. Modak**, S. Singh, S. K. Ray,
Advanced Energy Materials, **2020**, 2001305

Conferences

1. Negative Magnetization in Inverse Heusler Alloy Cr_2CoAl, A. Datta, **M. Modak**, M. Kundu, S. Banerjee, *AIP Conference Proceedings*, **2019**, 2115, 030489.
2. Magnetic properties of $Co_{2-x}Cr_{1+x}Al$ (x=0,0.4), A. Datta, **M. Modak**, S. Banerjee, *AIP Conference Proceedings*, **2020**, 2220, 110034.
3. Evidence of half-metallicity in full Heusler compound $(Co_{1-x}Cr_x)_2CrAl$; x =0,0.2, A. Datta, **M. Modak**, M. M. Patidar, V. Ganesan, S. Banerjee, *AIP Conference Proceedings*, **2020**, 2265, 030455.

Mantu Modak

Mantu Modak

Acknowledgement

First and foremost, I wish to thank my Ph.D. supervisor Prof. Sangam Banerjee, for giving me the opportunity to work under his guidance on interesting and fascinating properties of rare earth based intermetallics, Heusler alloy and making me to understand that research is a privilege, which deserves passion and devotion.

My sincere thanks to Dr. Bibekananda Maji of A. J. C. Bose College, Kolkata, for tremendous help with his expertise, experience and deep understandings in my subject. There is no doubt whatsoever, that my work would not have been possible without his active cooperation and invaluable support.

I would like to thank Dr. Gayatri N. Banerjee, Mr. Argha Dutta, Mr. Santu Dey of VECC, Kolkata, Dr. Biswarup Satpati of SINP, Kolkata, Dr. Surajit Saha of IISER, Bhopal, Dr. Anil Kumar Sinha of RRCAT, Indore for giving me the opportunity to use various experimental facilities in their respective institutes and Dr. Manas Sardar of IGCAR, Kalpakkam for his immense support with various physics related discussions. I also thank to Dr. Arpan Bhattacharyya for his help during synchrotron measurements. Without their help and support it would be difficult for me to complete the present work.

I wish to express my deep sense of gratitude to my doctoral committee members for critically evaluating my annual progress report and seminars during my Ph.D. work. Their crucial suggestions and comments helped me a lot to improve my understanding of the subject.

I am thankful to Goutamda, Ramakrishnada, Mukulda, Gobardhanda and other staff members in our division for their help during my Ph.D. work.

I gratefully acknowledge the financial support provided by DAE, DST, SERB for fellowship, travel support for pursuing experiments, research expenses etc. during my Ph.D. program.

I would like to express my special gratitude and thanks to Sampadda, Mayukhda, Kousikda who have trained me to several experimental facilities and data analysis techniques. I am very much thankful to my other lab-mates Sumitda, Bishnuda, Souravda, Amrita for their cooperation.

My thanks and appreciations also go to all of my friends and special thanks to Sourav, Dibyendu, Pintu, Arinda, Hossain, Hasem, Sayantika, Swapan, Rahul, Sandip whose friendship I will cherish forever for making my life enjoyable and also Anway, Sumanda, Sajad, Avijit, Gourav, Tamaghnada, Sukhenduda, Ram Chandra, Parimal, Bhaggyadhar for their precious friendship.

I must acknowledge my girlfriend Amrita for her patience with love and encouragement during my thesis work.

Last but not the least I owe my deepest gratitude to my beloved Parents, Mejda, Mama and other family members for all their affection, constant care, inspiration, and blessing throughout my life.

I sincerely apologies to those I missed out in this list but whose help have privileged me.

Kolkata Mantu Modak

August, 2020

Contents

List of Figures

List of Tables

Chapter 7

Summary and future scope

In this chapter, the results obtained from the study are summarized with a outlook on the future scope.

7.1 Summary and conclusions

A prominent minimum in the $M(T)$ curve has been observed inside the ferromagnetic ordered state for the $x = 0.02$ compound in the $Sm_{1-x}Gd_xAg$ series. It's a sign of magnetic moment compensation in the magnetically ordered state and can be explained in terms of the different temperature dependencies of antiparallelly coupled spin and orbital moments of the Sm^{3+} ions. This exotic feature has been further analyzed by structural, AC susceptibility, heat capacity, electronic transport, magneto-transport and thermal transport studies, from which no other magnetic or structural transition have been detected except the ferromagnetic transition.

We have observed that upon Cr doping in $ErRu_{2-x}Cr_xSi_2$ system, $\chi(T)$ mimics the field dependent magnetic susceptibility behavior of the parent

$ErRu_2Si_2$ compound. Increase of Cr amount modifies the c/a ratio, which affects the exchange interaction between the magnetic ions and induces weak ferromagnetic correlation in the system, and justifies the mimicking of $\chi(T)$ behavior. Above a certain Cr concentration, the order of magnetic transition also tending to SOMT instead of existing FOMT. Our findings also reveal the obtained magnetocaloric value $(-\Delta S_M^{max})$ in $x = 0.3$ compound is slightly higher than the parent one, which is also comparable to the other materials performing SOMT in the similar transition temperature region.

Er_3Pd_2 exhibits no thermal and magnetic hysteresis around its antiferromagnetic transition temperature $(T_N =)$ 10 K, which is confirmed as SOMT by nature. Obtained -$\Delta S_M(T)$ curves from both the magnetization and heat capacity data are in good agreement over the measured temperature region. Absence of any hysteresis around the transition temperature qualifies the sample to produce large and reversible MCE.

A detail estimation of the martensite, austenite and field induced austenite phase fractions, as a function of temperature and field within the MT region of $Ni_{44}Cu_2Mn_{43}In_{11}$ compound, have been represented. The obtained f_{IA} at any particular temperature depends on the availability and instability of f_M at that temperature. It has been evident that the f_{IA} has major contribution for the large MR than the other factors. However, the MR does not hold a linear relationship with the f_{IA}, rather it follows a power law. Furthermore, the temperature dependent XRD data supports the growth of austenite and martensite phases with temperature while warming and cooling, respectively, within the MT region of the studied compound.

7.2 Future scope

For better understanding of the observed spin-orbit magnetic compensation phenomena in the (Sm,Gd)Ag compound, magnetic Compton scattering and X-ray magnetic circular dichroism (XMCD) experiment need to be carried out. These could help to get the proper spin indication and more prominent explanation. Instead of Gd, the role of other $4f$ rare earth elements in the magnetic compensation behavior of SmAg series can be studied in future. Various critical exponents can be studied across the AFM transition temperature in the Er_3Pd_2 compound. Not only changing the doping element or doping concentration in the Er based systems, Er based other new magnetocaloric compounds can also be studied to achieve better magnetic entropy change. From the structural point of view, the growth dynamics of the martensite and austenite phases over temperature, with time or with magnetic field at a certain temperature, inside the MT region can be carried out.

Abstract

In this thesis, the structural, magnetic, transport and thermal properties have been carried out on polycrystalline intermetallic compounds, based on rare earth and transition metal elements. The aim of the present work is to understand the fundamental aspects of magnetism and to correlate among the magnetic, magnetocaloric and magneto-transport properties of rare earth based three different intermetallic series namely $Sm_{1-x}Gd_xAg$, $ErRu_{2-x}Cr_xSi_2$, Er_3Pd_2, and one Heusler alloy $Ni_{44}Cu_2Mn_{43}In_{11}$. Temperature dependencies of magnetization, AC susceptibility, heat capacity and transport behavior reveal the exotic thermomagnetic behavior in Gd doped SmAg system. A prominent minimum in the $M(T)$ curve has been observed inside the ferromagnetically ordered state for one of the doped compound. This feature has been explained in terms of the different temperature dependencies of antiparallelly coupled spin and orbital moments of the Sm^{3+} ions. Additionally, the polarized conduction electrons play an important role in the overall magnetic behavior of the system. Upon increase of Cr doping in the $ErRu_{2-x}Cr_xSi_2$ system, existing antiferromagnetic transition in the parent compound results to doping induced ferromagnetic transition. Above certain concentration, the nature of the transition is also modified to second order from first order. Slightly greater magnetic entropy change than the parent compound has been achieved for one of the doped member in the series. A large reversible magnetocaloric effect has been observed around 10 K, related to a second order magnetic transition from paramagnetic to antiferromagnetic state in the Er_3Pd_2 compound. Obtained magnetocaloric

data are well compared with the same obtained from heat capacity data. The influence of martensite and austenite phase volume fractions on the magnetoresistance have been studied across the first order martensite transformation of the $Ni_{44}Cu_{2}Mn_{43}In_{11}$ compound. The different phase volume fractions are calculated by measuring the resistivity as a function of temperature and magnetic field. It has been reveled that the field-induced austenite phase fraction at any temperature depends on the availability and instability of the martensite phase fraction at that temperature. This field-induced austenite phase fraction has been found to make a major contribution to the large magnetoresistance compared to the other factors. Furthermore, temperature dependent XRD data supports the growth of austenite and martensite phases with temperature within the martensite transition region of the studied compound.

Chapter 1

Introduction

1.1 General introduction

In current technological world immense use of devices, essential to our daily life, would have been nonexistent without the forefront research in magnetic materials. From the beginning of mariners' compass, throughout the history, magnetism is closely related to the appliances for making our life easier and enjoyable. Each magnetic device is designed on the basis of some fundamental or functional magnetic behavior of various precious materials. In this context, one of the most fascinating examples is the read heads in magnetic hard disks with tremendous storage capacity. They are based on the Giant Magnetoresistance (GMR) effect, discovered by P. Gr̈unberg and A. Fert in 1988. Another significant outcome related to the magnetic materials is the possibility of using some of them as magnetic refrigerants for magnetic cooling applications. This refrigeration technology is being seriously considered as an effective alternative to the conventional gas cooling technology. Magnetocaloric effect (MCE), discovered in 1881 by E. Warburg, is the underlying physical property, which determines the efficiency of a magnetic refrigerant. It has become an important topic of research for the last few years, both from the fundamental as well as application points of view. Magnetic materials are also used as components in a wide range of medical equipments and industrial purposes. Other important and interesting applications of the magnetic materials include high energy density permanent magnets, transformer cores, magneto-mechanical devices, magneto-electronic devices, magneto-optical devices, spin resolving devices using spin polarized materials, etc. Additionally, there are many other remarkable developments in the field of nanomagnetism, biomagnetism, molecular magnetism, photo magnetism with quite impressive application potential.

In consistency with the development of various functional materials for direct applications, many interesting novel fundamental phenomenon have also been observed. Some of the noteworthy examples are exchange bias, martensite transformation (magneto-structural transition), ferromagnetic shape memory effect, metamagnetism, superparamagnetism, spin glass/liquid state, spin-orbital compensation, spin reorientation transitions, etc. Therefore, any study about the development on the field of fundamental magnetism and magnetic materials would be incomplete without reference to such phenomenon.

The present thesis is devoted to the study of certain materials, which are of potential importance either from the application point of view or some phenomena with interesting underlying physics, as discussed above. All the studies have been carried out on magnetic and related functional properties, specially concentrated on magnetocaloric effect and magnetoresistance across the ferromagnetic/antiferromagnetic and martensite phase transitions, respectively of intermetallic systems based on rare earth and/or $3d$ and $4d$ transition metal elements. Additionally, spin-orbital compensation in magnetically ordered region in rare earth Sm based compounds have been investigated. Hereby, the thesis is divided into seven chapters. The **chapter 1** i.e. this chapter covers a brief introduction to the essentials of fundamental magnetism and phase transition. A discussion is also there for understanding of the experimental results of spin-orbital compensation, magnetocaloric effect, martensite transformation, etc. with introduction of the respective materials, presented in the subsequent chapters. The details of sample preparation, characterization techniques and working principle in short of all the experimental set up used in the present study have been discussed in **chapter 2**. **Chapter 3** deals with the study of magnetic, electronic, thermal, magneto-transport properties of $\mathrm{Sm}_{1-x}\mathrm{Gd}_x\mathrm{Ag}$ compounds to reveal its spin-orbital compensation behavior. **Chapter 4** presents the interesting change in magnetic and magnetocaloric properties of $\mathrm{ErRu}_{2-x}\mathrm{Cr}_x\mathrm{Si}_2$ compounds upon increase of Cr doping. **Chapter 5** contains the study of magnetic properties and magnetocaloric effect of $\mathrm{Er}_3\mathrm{Pd}_2$ compound. In **Chapter 6** the influence of martensite and austenite phase volume fractions on the magnetoresistance have been studied across the first order martensite transformation of the $\mathrm{Ni}_{44}\mathrm{Cu}_2\mathrm{MN}_{43}\mathrm{In}_{11}$ compound. The **Chapter 7** gives the summary of the results and conclusions. This Chapter also provides a short discussion on the possible future plans.

1.2 Fundamental magnetism

The magnetic properties of a material depend on the presence of a magnetic moment (μ) in the material even in the absence of an applied magnetic field and also upon its response to an external applied magnetic field. In classical concept, a magnetic moment is considered to a current loop equivalent [1]. However, The Bohr-van Leeuwen theorem reveals the existence of a magnetic moment in a classical system of electrons [1]. From the Quantum mechanical point of view, the magnetic properties of a material originate from the net magnetic moment, considering the contribution of electrons and nucleons in the atoms of that material. But the magnetic moment of nucleons is three orders of magnitude smaller than that of electrons, thus neglected in most of the systems. For electronic contribution in μ, one component is associated with the intrinsic spin angular momentum (sometimes simply referred as spin) of the electron is known as spin magnetic moment (μ_s). On the other hand, the component arises due to the orbital angular momentum of the electron, denoted as orbital magnetic moment (μ_o). Both the μ_s and μ_o are related to the respective angular momentum as $\mu_s = g_s S$ and $\mu_o = g_o L$. Where S and L are the spin angular momentum and orbital angular momentum, respectively; g is the gyromagnetic ratio and has different values for the spin and orbital motion of the electron. Hence, the spin and orbital angular momentum combine to form a net angular momentum which gives rise to the net magnetic moment to the atom. The magnetization (M) is defined as the net magnetic moment per unit volume of the material. Sometimes in solid, particularly in $3d/4f$ materials, electrons can not draw a definite orbit due to

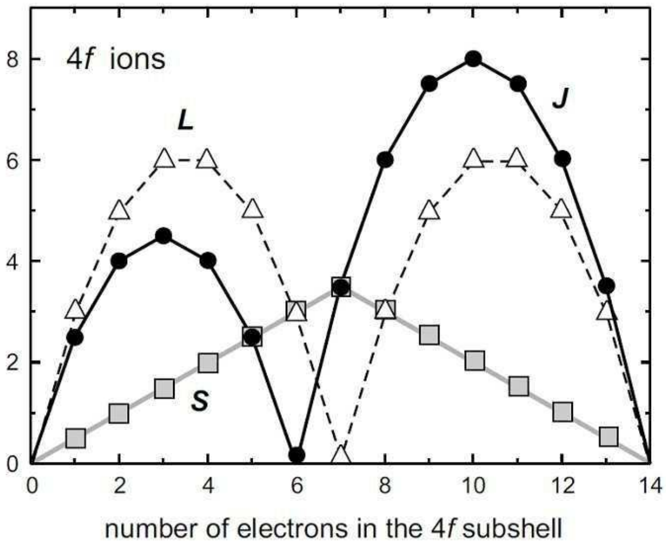

Figure 1.1: The values of L, S, and J for the series of trivalent $4f$ ions (taken from Ref. [3]).

the interactions between them (exchange interactions) and this leads to the negligible orbital contribution to the net magnetic moment ($\mu = \mu_s$). Various aspects of magnetism in materials are introduced briefly in the following sections.

1.2.1 Magnetism of rare earths (R)

The group of elements with atomic numbers $57 - 71$ (lanthanides) and 39 (Yttrium) in the periodic table are called rare earth elements. It should be noted for these elements that the outermost electron shells, which determine the number and nature of the valence electrons, are identical. Therefore, the physical properties of the rare earth trivalent ions are very similar. However, the magnetic properties of these elements are quite fascinating as the ions exhibit a systematic variation and intelligible complexity. Furthermore, the magnetic behavior of one ion becomes distinct from another according to the number of $4f$ electrons present in the inner shell [2]. This is due to the large degree of localization of $4f$ electrons, even in the metallic state, the $4f$ core retains its integrity and its atomic properties. Thus, no other group of elements in the periodic table are as interesting as rare earth group, as far as magnetism is concerned.

The magnetic ground states of the rare earth ions have been well explained using the Hunds rules [2,3]. The predictions of the orbital angular momentum quantum number L, the spin angular momentum quantum number S and the total angular momentum quantum number J for the $4f$ ions using Hunds rules are illustrated in Figure 1.1. The effective magnetic moment (μ_{eff}) per ion can be calculated theoretically using Hunds rule as,

$$\mu_{eff} = \mu_B g_J \sqrt{J(J+1)} \tag{1.1}$$

Where μ_B is Bohr magneton and g_J is called the Lande spectroscopic g-factor as

$$g_J = \frac{3}{2} + \frac{S(S+1) - L(L+1)}{2J(J+1)} \tag{1.2}$$

It should be kept in mind that the μ_{eff} can point only at certain discrete angles to the applied field due to the spatial quantization. The component of μ_{eff} in the direction of the applied field H is

$$\mu_H = g_J M_J \mu_B \tag{1.3}$$

The allowed values of M_J are, J, $J-1$, $J-2$, ..., $-(J-2)$, $-(J-1)$, $-J$.

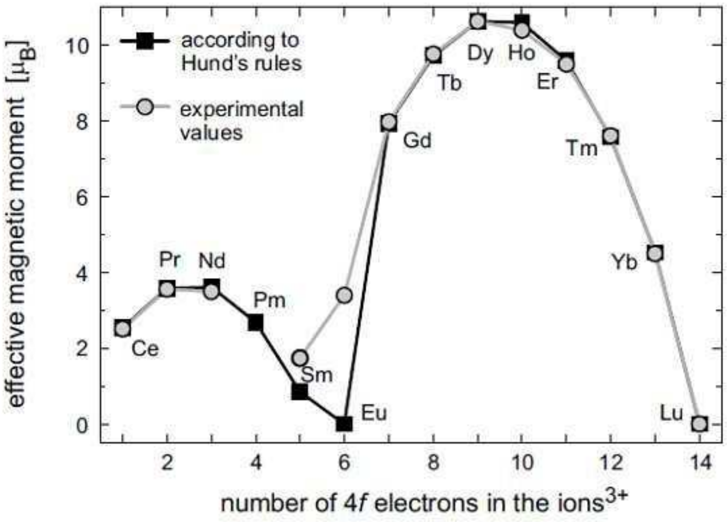

Figure 1.2: μ_{eff} in unit of μ_B of $4f^{3+}$ ions according to Hunds rules in comparison with the experimental values (adapted from Ref. [3]).

The maximum value of μ_H i.e the saturation magnetic moment is

$$\mu_H^{sat} = g_J J \mu_B \tag{1.4}$$

The μ_{eff} can also be calculated experimentally from the susceptibility measurement using the formula

$$\chi = \frac{n\mu_{eff}^2}{3k_B T} \tag{1.5}$$

where χ is the volume susceptibility, n is the number of contributory magnetic ions per unit volume, and k_B is the Boltzmann constant. A good agreement has been observed between theoretically and experimentally calculated μ_{eff} values for the $4f$ ions except for the Sm^{3+} and Eu^{3+}, shown in Figure 1.2. For these ions the ground state calculation needs to consider the influence of the higher states of the $L-S$ multiplet, because the separation between the successive multiplets is comparable to k_B at room temperature [2,3]. A multiplet is the set of levels of different J values arising out of a given L and S. The levels of a multiplet split by the strong spin-orbit interaction.

1.2.2 Magnetism of transition metals (T)

The elements with incomplete inner d electron shells are defined as transition metal elements. For this thesis work, some of the $3d$ and $4d$ T elements have been used. Starting from Scandium (Sc) to Zinc (Zn) are $3d$ transition metal and Yttrium (Y) to Cadmium (Cd) are $4d$ transition metals elements. Though Zn and Cd have complete d sub-shell but they show similar properties with the others in the same group. $3d/4d$ elements have an incomplete inner electron shell and therefore carry nonvanishing magnetic moments in the metallic and ionic forms. Unlike the rare earth ions, the experimental μ_{eff} for the transition metal ions are in poor agreement with equation (1.1). The experimental values often agree quite well with $\mu_{eff} = 2\mu_B\sqrt{S(S+1)}$, calculated using $L = 0$. Usually, the $4f$ shell has been found responsible for the magnetism in the rare earth ions and lies deep inside the $5s$ and $5p$ shells. Whereas in the transition metals ions, the d shell is responsible for magnetism, which is the outermost shell. Because of the large spatial spread, the d electrons experience a strong inhomogeneous electric field produced by neighboring ions. This inhomogeneous electric field is called crystalline electric field (CEF). Therefore, in the case of d ions, the CEF often causes quenching of orbital angular momentum, thereby giving rise to almost pure-spin magnetism. Large spatial spread of d electron wave functions also giving rise to the itinerant character to these electrons. The magnetism in these systems are therefore contributed by itinerant d-electrons, participating in the Fermi surface. Therefore, unlike the rare earth, the transition metal magnetism is itinerant. As a consequence of this, the magnetic properties in these systems have to be treated under the preview of the band model.

1.3 Exchange interactions in solid

In solids, the overlapping of electronic orbitals of the neighboring atoms leads to electrostatic interaction of the electrons. This originates the interatomic exchange interaction, which is quantum mechanical in nature and subject to the correlation of atomic moments. It makes the total energy of the crystal dependent on the relative orientation of spins, localized on the neighboring atoms. The exchange interaction for a many electron systems is expressed using Heisenberg exchange Hamiltonian [1]

$$H_{ij} = -2 \sum_{i>j} J_{ij} S_i \cdot S_j \tag{1.6}$$

where J_{ij} is the exchange constant between the ith and jth spins (S_i and S_j). Exchange interaction is the strongest magnetic interaction in solids (~ 1 eV) and it should be noted that it is usually much stronger than the magnetic dipole-dipole interaction in ordered magnetic materials. This is responsible for the existence of parallel (ferromagnetic), and antiparallel (antiferromagnetic) spin alignment depending upon the sign of the exchange constant of the neighboring spins. Positive J_{ij} favors the parallel configuration of spins,

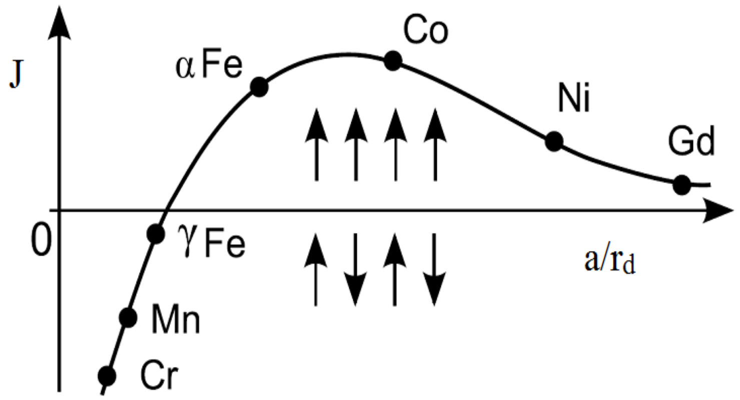

Figure 1.3: Direct exchange integral (J) as a function of the ratio of interatomic distance (a) and the radius of the d orbital (r_d). The curve is known as the Bethe-Slater curve (taken from ref. [7]).

while for a negative J_{ij} the antiparallel configuration is lower in energy. Some of the most important exchange mechanisms have been described below [4,5] among the various types of exchange interaction.

1.3.1 Direct exchange

The direct exchange involves the overlapping of electron wave functions from the two neighboring atoms, the Coulomb electrostatic interaction and the Pauli exclusion principle, which requires different symmetry properties from the spatial and spin parts of the electronic wave function. According to Bethe and Slater, depending on the interatomic distances (i.e. orbital overlap) and with balance between the Coulomb interaction and kinetic energies of the electrons, the values of J might have a positive or negative sign [6]. When the interatomic distance is small, antiparallel alignment (antiferromagnetic) between the spins of the neighboring atoms is favorable. Whereas, the Pauli exclusion principle keeps the electrons with parallel spin away from each other, thereby reducing the Coulomb repulsion it gives rise to parallel alignment or positive exchange (ferromagnetism). In Figure 1.3 the Bethe-Slater curve represents the magnitude of direct exchange as a function of a/r_d, where a is the interatomic distance and r_d is the radius of the d orbital. The direct exchange is a short-range interaction. If the interatomic distance is too large (i.e. the wave function overlap becomes too small) the direct exchange coupling will not be strong enough to overcome the thermal excitations, giving rise to paramagnetism. It should be noted that in case of $4f$ electrons, they are so strongly localized that the direct exchange interaction is unlikely in rare-earth elements.

1.3.2 Itinerant exchange

The magnetic properties of metallic $3d$ electronic elements, like Fe, Co or Ni, can not be described in terms of direct exchange of intersite atomic or ionic moments. The magnetic moment of these metals arises due to the itinerant electrons, and one has to invoke the exchange interaction in the band model. As a consequence of the Coulomb repulsion of the electrons and their kinetic energy, the bands with opposite spin orientation are exchange split (see Figure 1.4), giving rise to a non-zero total magnetic moment, which appears as ferromagnetism. This exchange splitting can be described using the Stoner model. According to the Stoner criteria, ferromagnetism is possible only when $IN(E_F) > 1$, where I is the exchange energy per pair of $3d$ electrons and $N(E_F)$ is the density of states at the Fermi level [1,8]. A high density of

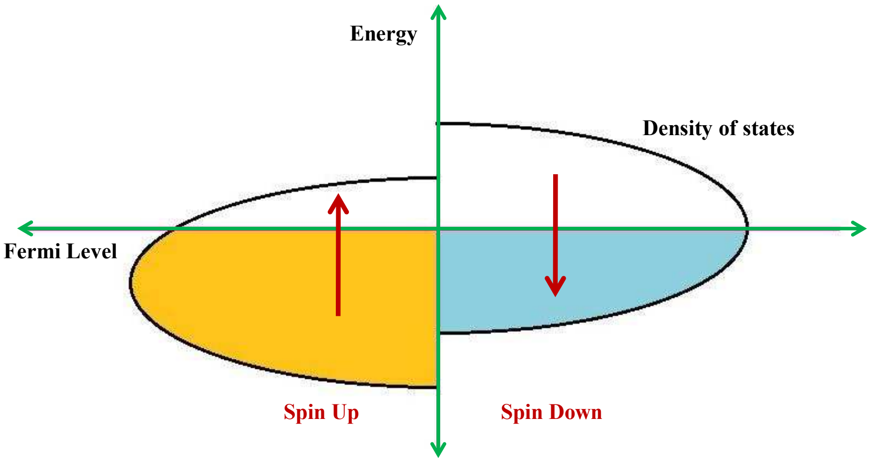

Figure 1.4: A schematic band structure for the Stoner model, showing the spontaneous splitting of energy bands of opposite spins without an applied magnetic field and the states near the Fermi level are spin-polarized.

states at the Fermi level and a strong exchange splitting thus favor metallic ferromagnetism. If the Stoner criteria is not satisfied, the spontaneous ferromagnetism will not occur. But, it can help for a large enhancement in the susceptibility by a factor of $1/(1 - IN(E_F))$. This phenomenon is known as Stoner enhancement or exchange enhanced Pauli paramagnetism.

1.3.3 RKKY exchange

In the rare earth, because of the highly localized character of the $4f$ wave functions, the direct interaction between the $4f$ moments is not possible, rather it is mediated by the polarization of conduction electrons. A localized moment polarizes the conduction electrons and successively this polarization couples with the neighboring localized moments at a distance r. This indirect interaction is known as Ruderman-Kittel-Kasuya-Yosida (RKKY) interaction [10]. The distance dependent exchange interaction $J_{RKKY}(r)$ for large r is

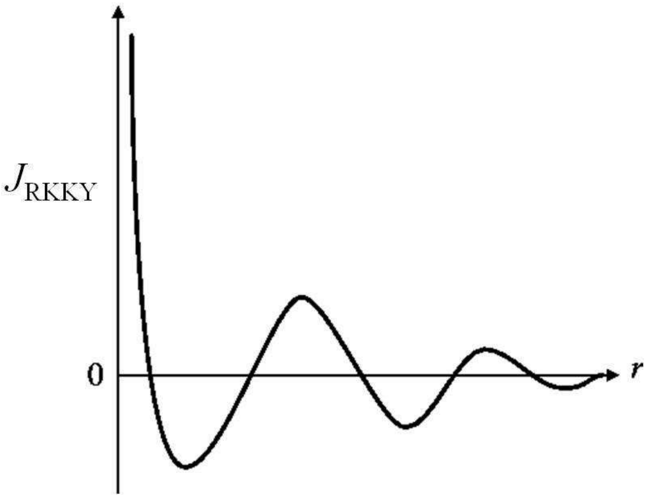

Figure 1.5: Variation of exchange integral J_{RKKY} as a function of distance r.

given by

$$J_{RKKY} \propto \frac{cos(2k_F r)}{r^3}, \tag{1.7}$$

assuming a spherical Fermi surface of radius k_F. Unlike the direct exchange interaction, this interaction is long range and possesses an oscillatory dependence on the distance between the localized moments, as shown in Figure 1.5. Depending upon the distance following J_{RKKY}, the type of coupling can be either ferromagnetic or antiferromagnetic. Though the RKKY interaction can interpret the magnetic properties of many rare earth compounds and alloys but found insufficient to describe some of the experimental results correctly [9]. This may be due to the rough approximations used and the other possible interactions which are neglected in this model. On the other hand, for the rare earth elements, a completely different interaction has been proposed by Campbell [10], the $5d$ electrons of Actinoids are less localized than the $4f$ rare earth electrons and a considerable overlap is possible between the

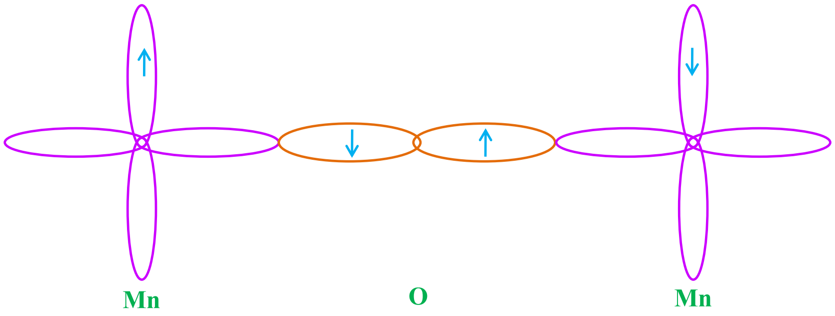

Figure 1.6: Schematic illustration of the super exchange interaction between two magnetic ions (Mn^{2+}) separated by a non magnetic ion (O^{2-}). The arrows show the spin directions of the four electrons and the distribution over the Mn and O ions.

$5d$ electron wave functions of neighboring atoms. Thus $4f$ electrons induce a positive local $5d$ moment through the ordinary intra-atomic $4f-5d$ exchange and then the interaction between the $4f$ electrons take place via the direct $5d-5d$ interaction. This direct $5d-5d$ interaction being positive, the overall indirect interaction between the $4f$ moments is always ferromagnetic.

1.3.4 Superexchange

Super exchange interaction is an indirect exchange interaction between two magnetic ions separated by a nonmagnetic ion and mediated through it. It describes the magnetic ground state of some of the ionic solids, including oxides and fluorides, antiferromagnetic insulators like MnO, NiO etc. The coupling between the moments on a pair of metal cations (Mn^{2+} or Ni^{2+}) is mediated by a diatomic anion (O^{2-}) through the overlap of the metals $3d$ and oxygens $2p$ orbitals, and a partial delocalization of the involved electrons, as illustrated in Figure 1.6. It has been observed that antiferromagnetic cou-

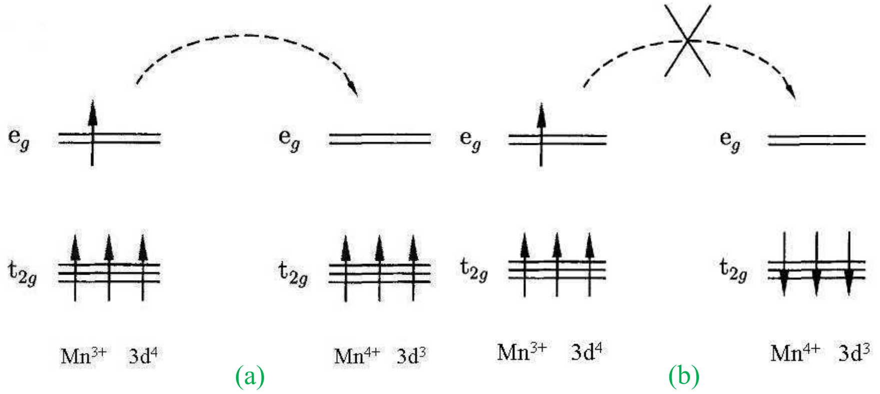

Figure 1.7: In double exchange interaction, (a) electron delocalization (hopping) is possible in ferromagnetic configuration, (b) electron hopping is not possible in antiferromagnetic configuration (picture taken from Ref. [1]).

pling reduces the energy of the system by allowing larger delocalization (over the bond length), thus lowering the kinetic energy. However, the strength of the superexchange depends on the magnitude of the moments on the metal atom, the degree of overlap of orbitals and the bond angle.

1.3.5 Double exchange

It is possible to have a ferromagnetic exchange interaction between the magnetic ions of mixed valence via nonmagnetic ions. Examples of this are the compounds containing Mn in mixed valence states as Mn^{3+} or Mn^{4+} i.e. the oxidation states are 3 or 4. Double exchange mechanism can be understood from Figure 1.7, where the neighbor of Mn^{3+} is a Mn^{4+} ion which has no electron in its e_g shell. The e_g electron on a Mn^{3+} ion can hop to a neighboring site only if there is a vacancy of the same spin. The double exchange predicts that this electron hopping from donating ion to receiving ion will be easier if the electrons do not need to spin flip, i.e., to change spin direction in order to conform with Hunds rules. Therefore, it is not energetically favorable for an e_g electron to hop to a neighboring ion in which the t_{2g} electrons' spins are antiparallel to the e_g electron (see Figure 1.7(b)). Generally hopping of electrons reduces the kinetic energy, the overall energy saving can lead to a ferromagnetic alignment of neighboring ions. Furthermore, the ferromagnetic alignment allows the e_g electrons to hop through the crystal and the material can show metallic behavior.

It is ought to be mentioned that in superexchange interaction, a ferromagnetic or antiferromagnetic alignment occurs between two atoms with the same valence. On the other hand, in double exchange, the interaction occurs only when one atom has an extra electron compared to the other (mix valency).

1.4 Magnetic anisotropy

Another important characteristic of any magnetically ordered material is the magnetic anisotropy. In an isotropic material its physical properties should be independent of direction. However, most of the magnetic materials show some preferred direction of magnetization and are said to be anisotropic in nature. For example, in a single crystalline ferromagnet, the magnetization (M) tends to lie along certain crystallographic axes called directions of easy magnetization (easy axis). Hereby, the anisotropy is defined as the amount of energy required to turn M into any direction from its preferred axes. It originates from the dependence of the energy of the system on the orientation of the magnetization with respect to the crystal axes. Anisotropy is an important subject to study, because it is exploited in the design of most magnetic materials with commercial importance. The magnetic anisotropy can be intrinsic to the system e.g. magnetocrystalline anisotropy, or it can be extrinsic also e.g. magnetoelastic anisotropy, shape anisotropy, exchange anisotropy etc. [11]. These contributions are discussed in the following subsections.

1.4.1 Magnetocrystalline anisotropy (MCA)

The magnetocrystalline anisotropy originates from the crystal field effect and the spin-orbit interaction. The former removes the degeneracy associated with the orbital angular momentum quantum number. Because of the spin-orbit coupling, when an external field tries to reorient the spin of an electron, the orbit of that electron also tends to be reoriented. But, the electron orbitals are strongly coupled to the lattice and therefore resist the attempt to rotate the spin axis. Therefore, the energy required to turn the spin away from the easy direction, which is called anisotropy energy, is just the energy required to overcome the spin-orbit coupling. Although the magnetocrystalline energy is usually small compared to the exchange energy, the direction of the magnetization is only decided by the anisotropy. The exchange interaction just tries to align the magnetic moments parallel, no matter in which direction. The magnetocrystalline anisotropy energy can be expressed in terms of power series expansion of the direction cosines of M

with respect to the crystal axes

$$E_{crys} = E_0 + \sum_{ij} b_{ij}\alpha_i\alpha_j + \sum_{ijkl} b_{ij}\alpha_i\alpha_j\alpha_k\alpha_l. \tag{1.8}$$

This is the general equation where α_i, α_j, α_k and α_l are the direction cosines of M with respect to the crystal axes. Type of the magnetocrystalline anisotropy and expression for it depends on the crystal structure. For cubic systems equation (1.8) can be expressed as

$$E^{cubic}_{crys} = K_0 + K_1(\alpha_1^2\alpha_2^2 + \alpha_2^2\alpha_3^2 + \alpha_3^2\alpha_1^2) + K_1\alpha_1^2\alpha_2^2\alpha_3^2 + ... \tag{1.9}$$

where K_i are the magnetocrystalline anisotropy constants which are the functions of the coefficients b.

For tetragonal systems

$$E^{tetra}_{crys} = K_0 + K_1\cos^2\theta + K_2\cos^4\theta + K_3\sin^4\theta(\sin^4\phi + \cos^4\phi) \tag{1.10}$$

where the direction cosines α_i are replaced by the angle θ and ϕ (in spherical polar coordinate).

For hexagonal systems

$$E^{hexa}_{crys} = K_0 + K_1\sin^2\theta + K_2\sin^4\theta + K_3\sin^6\theta + K_4\sin^6\theta\cos 6\phi. \tag{1.11}$$

The magnetocrystalline anisotropy constants (K_i) depend on the material and the temperature. The easy magnetization direction is determined by sign and ratio of the anisotropy constants and it can be identified by calculating the minimum energy of E_{crys} [3].

1.4.2 Magneto-elastic (or stress) anisotropy

Anisotropy originates from the mechanical deformation in a magnetic system is known as magneto-elastic or stress anisotropy. It is well known that the spin moments are coupled to the lattice through the orbital motion (mediated by the spin-orbit and orbit-lattice coupling). In any case, if the lattice is deformed, the distances between the magnetic atoms are altered and hence the interaction energies get vary. Thereafter, alignment of the magnetic moments along a certain direction may lower the energy as compared to the alignment along the other directions, this produces the magneto-elastic anisotropy. This is the inverse of magnetostriction, in which the magnetic system gets deformed when it is magnetized. For an elastically isotropic medium with isotropic magnetostriction λ_m, the magneto-elastic energy per unit volume under stress σ can be expressed as

$$E_{me} = -\frac{3}{2}\lambda_m \sigma \cos^2\phi = K_\sigma \cos^2\phi \tag{1.12}$$

where ϕ is the angle between the magnetization and stress directions, and K_σ represents the stress anisotropy constant. It should be mentioned that when λ_m is negative (K_σ is positive), as example, for nickel under tension, the stress axis becomes a hard axis. On the other hand, stress axis is easy axis for the system with positive λ_m (positive K_σ) as in case of iron.

1.4.3 Shape anisotropy

In case of a ferromagnetic material of arbitrary shape, the internal energy is different for the magnetization lying along the different axes of the sample. This effect is termed as the shape anisotropy. Usually, it appears as a result of the magnetostatic energy due to the magnetic free poles at the outer surface of the sample. Thus it is also known as magnetic dipolar anisotropy. To represent this effect in better, a demagnetizing scalar factor N has been introduced along three perpendicular directions in such a way that it follows $N_x + N_y + N_z = 1$. Now, the magnetostatic energy, which originates due to the magnetic free poles, can be expressed as $E_{ms} = NM^2V$, where M is the magnetization, N is the direction and shape dependent demagnetizing factor, and V is the volume of the sample.

For example, in a thin film, N is zero along the plane of the film and is 1 along the normal to the film. This results a preferred orientation of M in the plane of the film. For a spherical sample $N_x = N_y = N_z = 1/3$, so no direction is preferable from the shape anisotropy. Furthermore, the demagnetizing field due to the free poles in a particular orientation of the sample is given by $H_D = -NM$. Here N is the demagnetizing factor for that orientation of the sample.

1.4.4 Exchange anisotropy

Unlike the uniaxial MCA, exchange anisotropy is unidirectional. It arises due to the exchange coupling at the interface between an AFM and FM material [12–14]. It results a shift in the hysteresis loop along the negative field direction, known as exchange bias (EB). The EB effect was first observed in partially oxidized Co nano particles by Meiklejohn and Bean [12]. Later on EB has been observed in many multilayer systems having FM/AFM interface such as fine particles, inhomogeneous materials and thin films [13,15–18]. The EB is of tremendous utility in magnetic recording devices and permanent magnets [19].

1.5 Crystalline Electric Field (CEF) effects

One of the important sources of anisotropy in R ions is the crystalline electric field (CEF), which is generated through neighboring ions in the crystal. It causes a distortion in the spherical $4f$ charge density. Usually, this deformation is considerably small at high temperatures, however, it increases on reducing the kinetic energy of the $4f$ electrons by decreasing temperature. Therefore, at low temperature, the movement of the electrons are influenced by the nonspherical CEF potential. Thus, the resulting magnetic moment, generated by this movement contains an anisotropic behavior. It should be mentioned that the CEF interaction is relatively weak in the $4f-$R series, because the $4f$ shell is buried deep inside the atom; so that the crystal-field (CF) potential is sufficiently screened by the outer electrons. Therefore, spin-orbit Hamiltonian ($\mathcal{H}_{so}$) must be considered before CF Hamiltonian ($\mathcal{H}_{cef}$) in any perturbation scheme for evaluating the energies of $4f$ ions. The energy difference between the multiplets, caused by the CF interaction is of the order of 10^2 cm^{-1}. This is weaker than the spin-orbit interaction that leads to the multiplets energy separation $\sim 10^3$ cm^{-1} [20]. The Hamiltonian of an R ion in a solid, consisting of spin-orbit coupling, CEF, Zeeman and exchange field terms, can be represented as

$$\mathcal{H} = \mathcal{H}_0 + \lambda \vec{L} \cdot \vec{S} + \mathcal{H}_{cef} + \mathcal{H}_Z + \mathcal{H}_{ex} \tag{1.13}$$

where $\mathcal{H}_0$ is the Hamiltonian corresponding to the kinetic and potential energy. The energy and eigen function of the ion can be obtained by diagonalizing the above Hamiltonian. In general the CEF Hamiltonian ($\mathcal{H}_{cef}$) can be expressed as [21, 22]

$$\mathcal{H}_{cef} = \sum_l \sum_m B_l^m O_l^m \tag{1.14}$$

where B_l^m are the CF parameters and O_l^m are the Stevens equivalent operators which measure the strength of the crystal field [8, 20, 23]. The eigenfunction and energies, corresponding to the crystal field split of the ground state J multiplet, can be calculated by diagonalization of $\mathcal{H}_{cef}$. Calculation of crystal field effects in T is quite difficult because it has large band widths associated with the $3d$ electrons. It has been found that this contribution is smaller than that of the R in most of the R-T intermetallic compounds. On the other hand, the CEF associated with T ions in ionic (ceramic) compounds is quite strong and its calculation is more straightforward.

1.6 Phase transition

A phase is usually defined as a region of homogeneous macroscopic properties of a material, such as density, atomic arrangements/crystal structure, chemical composition, magnetic order etc. However, a material can be in different phases at different values of the various control parameters like temperature, pressure, magnetic field etc. A phase transition is the transformation from one phase to another with changing the control variable.

1.6.1 Classification of phase transitions using Ehrenfest scheme

When a thermodynamic phase transition occurs in a material from a high temperature phase to a low temperature phase, the free energies of both the phases remains equal at the thermodynamical phase transition temperature (T_C). However, a certain order of the derivative of the free energy with respect to a control variable may differ. In the Ehrenfest's scheme, the order of a phase transition is defined by the lowest order of the derivative of free energy which is discontinuous across the phase transition [16, 24, 25]. If we consider $G1$ and $G2$ are the free energies of the two phases corresponding to a thermodynamical phase transition, then the phase transition will be of nth order if

$$\left.\begin{array}{l} \frac{d^nG_1}{dT^n}|_{T_c} \neq \frac{d^nG_2}{dT^n}|_{T_c} \\ \\ \frac{d^mG_1}{dT^m}|_{T_c} = \frac{d^mG_2}{dT^m}|_{T_c} \end{array}\right\} \tag{1.15}$$

where m and n both are integers and $0 \leq m < n$. Some of the physical parameters are described in terms of the derivatives of free energy with respect to the various control variables, as

$$\left.\begin{aligned}Entropy\ (S) = -(\tfrac{dG}{dT})_P\\ Volume\ (V) = (\tfrac{dG}{dp})_T\\ Magnetization\ (M) = -(\tfrac{dG}{dH})_{T,P}\\ Heat\ Capacity\ (C) = T\tfrac{dS}{dT} = -T(\tfrac{d^2G}{dT^2})\\ Isothermal\ compressibility\ (K_T) = -\tfrac{1}{V_0}(\tfrac{dV}{dP})_T = -\tfrac{1}{V_0}(\tfrac{d^2G}{dP^2})_T\\ Susceptibility\ (\chi) = (\tfrac{dM}{dH}) = -(\tfrac{d^2G}{dH^2}).\end{aligned}\right\} \quad (1.16)$$

As per the Ehrenfests criterion, discontinuous change in the first derivative of free energy i.e. volume, entropy, magnetization etc., across the phase transition qualifies as first order (see Figure 1.8). On the other hand, a continuous first order derivative but a discontinuous second order derivative, e.g. heat capacity, susceptibility and compressibility, serve the phase transition as second order (see Figure 1.8(d)). In a first order phase transition (FOPT), a discontinuity in entropy signifies to the presence of latent heat (L_Q), L_Q = $T_C\Delta S$ where $\Delta S = (S_2 - S_1)_{T_C}$ is the difference in entropy between the two phases at T_C. All the higher order phase transitions do not have a latent heat. Furthermore, it has been observed experimentally that in most of the phase transitions which do not have a latent heat, the heat capacity either diverges or exhibits a cusp, and hence do not fit in Ehrenfests scheme [16].

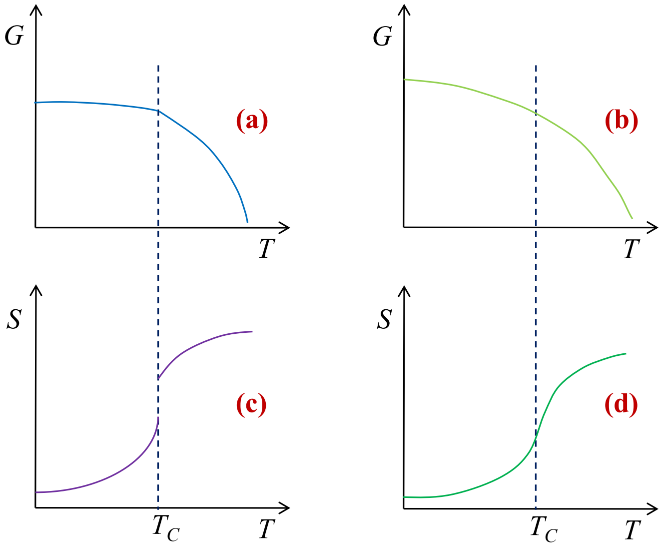

Figure 1.8: Ehrenfests scheme of phase transition. Free energy (G) as a function of temperature (T) across (a) a first order phase transition and (b) for higher order phase transition. Temperature dependence of entropy (S) is also shown for (c) a first order phase transition and (d) a higher order phase transition.

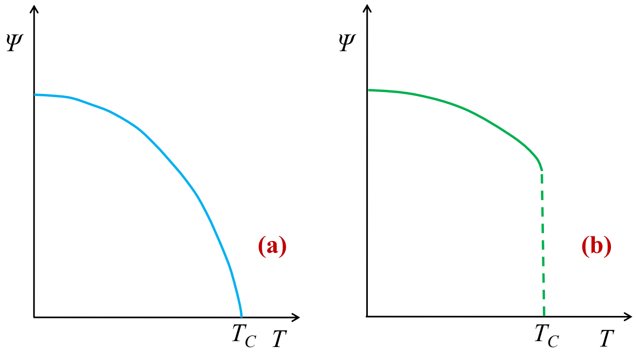

Figure 1.9: Temperature dependence of the order parameter (ψ) for (a) a second order phase transition (SOPT) and (b) a first order phase transition (FOPT).

1.6.2 Modern classification of phase transitions

A phase transition is termed as discontinuous (first order) if it has a latent heat. All other phase transitions which do not have a latent heat are known as continuous phase transitions (it includes the second to higher order phase transition in Ehrenfests sense).

Order parameter: Order parameter is an entity or observable, which is considered as zero in the high temperature phase and is non-zero in the low temperature phase [26], the concept was introduced by L. D. Landau. Some of the example of order parameter corresponding to various phase transition are given in table 1.1. By definition, if the order parameter is zero at the T_C and gradually grows with decreasing temperature, the transition is second order phase transition (SOPT). On the other hand if it suddenly increases to a finite value from zero with a discontinuity at the transition temperature, the transition is called FOPT [26], as depicted in Figure 1.9.

Table 1.1: Order parameters for phase transition for various system

Phase transition	Order Parameter
Ferromagnetic	Spontaneous magnetization
Antiferromagnetic	Sublattice magnetization
Ferro-electric	Polarization

1.6.3 Landau theory of phase transition

Second order phase transition (SOPT)

Landau theory of phase transition assumes that the order parameter (ψ) is small and uniform across the phase transition and the free energy density

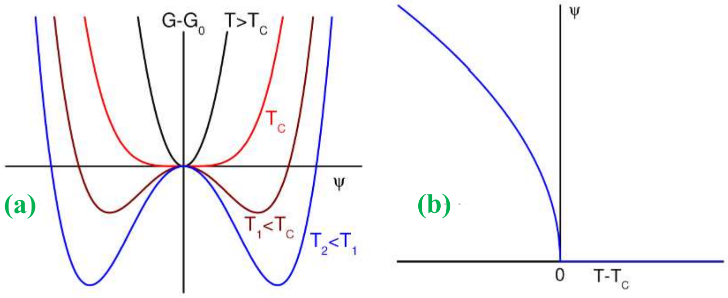

Figure 1.10: (a) Variation of Landau free energy (G) with order parameter (ψ) at different temperatures (T) for SOPT as per equation (1.17) (b) Temperature dependence of the order parameter. (Picture taken from Ref. [27]).

is considered to be an analytical function of the order parameter. For an SOPT the expansion of free energy (G) as power series of ψ can be expressed as [26].

$$G = G_0 + a(T - T_c)\psi^2 + D\psi^4 + ... \tag{1.17}$$

Here G_0 is the free energy of the system associated with the degrees of freedom of the system but not a function of ψ. However, the coefficients a and D are system dependent. As discussed previously, T_C is the thermodynamical phase transition temperature, the temperature where both the phases have equal free energies. The plot of free energy as a function ψ, using equation (1.17) at various temperatures, are shown in Figure 1.10(a). With decreasing temperature, down to T_C, $\psi = 0$ is the only minimum, i.e., the high temperature phase with $\psi = 0$ is stable down to $T = T_C$. Whereas, at $T < T_C$, $\psi = 0$ becomes a maximum and there exist two minima at the positive and negative sides of ψ with equal magnitude. The order parameter evolves continuously across the transition, as shown in Figure 1.10(b) and there is no latent heat involved [26].

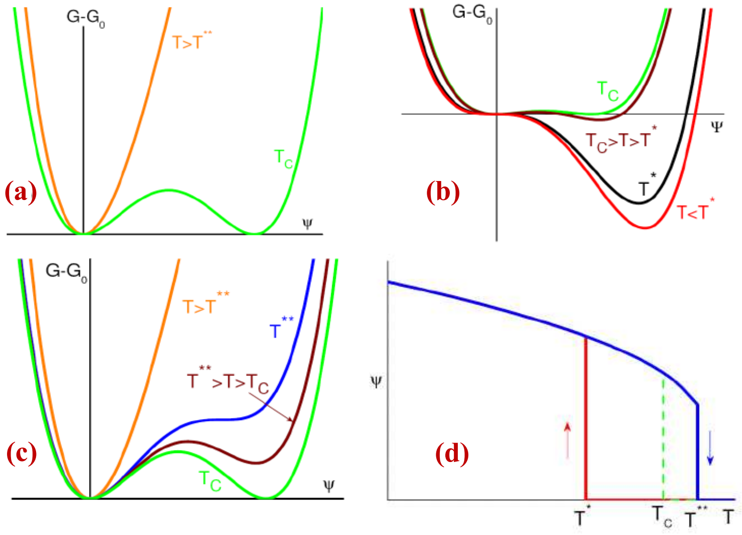

Figure 1.11: Variation of Landau free energy (G) with order parameter (ψ) for FOPT in equation (1.18) at (a) $T >> T_C$ and at $T = T_C$, (b) $T \leq T_C$ while cooling and (c) $T \geq T_C$ while heating. The temperatures T^* and T^{**} are the limits of metastability while cooling and heating respectively. (d) ψ as a function of T for cooling and heating (picture taken from Ref. [27]).

First order phase transition (FOPT)

Across a FOPT the change in order parameter is assumed to be discontinuous, so the order parameter jumps to a finite value at the transition temperature. If symmetry considerations allow a third order term in the expression of the free energy, then the free energy can be written as a function of ψ, likely

$$G = G_0 + a(T - T^*)\psi^2 - C\psi^3 + D\psi^4 + ... \tag{1.18}$$

Here T^* is the temperature where the free energy at $\psi = 0$ ceases to be a minimum. This free energy function is plotted in Figure 1.11.

supercooling and superheating: It is evident from the equation (1.18) and Figure 1.11 that the free energy has multiple maxima/minima in certain temperature range. While decreasing temperature, at T_C there are two minima, with $\psi = 0$ and $\psi \neq 0$ having equal free energy values. This temperature is known as the thermodynamical transition temperature of the phase transition from $\psi = 0$ phase to $\psi \neq 0$ phase. Accordingly, the order parameter ψ increases discontinuously at T_C, as indicated by the red cooling curve in Figure 1.11(d). However, $\psi = 0$ remains a local minimum down to T^* while cooling. Similarly, with increasing temperature the free energy minimum at $\psi > 0$ persists up to T^{**}. This predicts a thermal hysteresis between the cooling and heating cycle across the transition temperature (see Figure 1.11(d)). Thermal hysteresis is a generic feature of FOPT and treated as a qualifying criterion for a FOPT in the cases where latent heat is difficult to ascertain [28].

It should be noted that thermodynamically the phase transition should occur at T_C. However during cooling, the high temperature phase remains stable against small energy fluctuations down to T^*. Whereas a sufficiently large energy fluctuation can convert this high temperature $\psi = 0$ phase to low temperature $\psi > 0$ phase. Therefore, the high temperature phase is a metastable phase and the temperature T^* is the limit of metastability of the high temperature phase, while cooling. Thus the higher temperature phase can be supercooled down to T^*. Similarly, the low temperature phase can remain as a metastable phase up to T^{**} while heating. Thus, the system can be treated as superheated up to T^{**}. It can be shown that the equation (1.18) predicts a change in entropy across the phase transition and hence the phase transition has a latent heat [26].

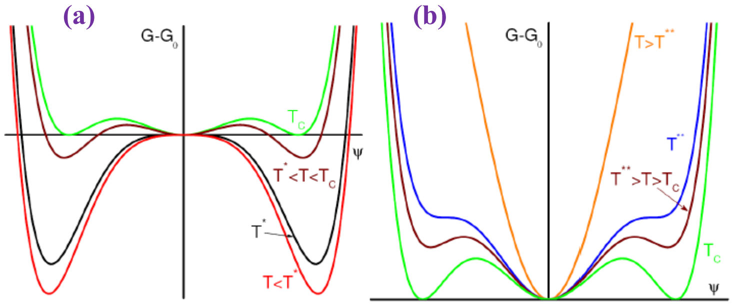

Figure 1.12: Variation of G with order parameter (ψ) in equation (1.19) at (a) temperature $T \leq T_C$ and (b) $T \geq T_C$. T_C, T^* and T^{**} are already defined (picture taken from Ref. [27]).

FOPT with a negative fourth order term in the free energy expansion

An FOPT can also occur in Landau scheme even if a third order term is prohibited by symmetry. The following free energy expression, symmetric in order parameter also describes an FOPT.

$$G = G_0 + a(T - T^*)\psi^2 - D\psi^4 + F\psi^6 + ... \tag{1.19}$$

The function is plotted in Figure 1.12. In this case the free energy also has multiple minima in a certain temperature range. This free energy function has minima on both sides of $\psi = 0$. Here the high temperature phase ($\psi = 0$) can exist as a metastable phase down to the temperature T^* (see Figure 1.12(a)) and the low temperature phase ($\psi \neq 0$) can exist as a metastable phase up to the temperature T^{**} (see Figure 1.12(b)). Furthermore, equation (1.19) also predicts a discontinuous change in order parameter similar to that shown in Figure 1.11(d) with an entropy jump and a latent heat across the

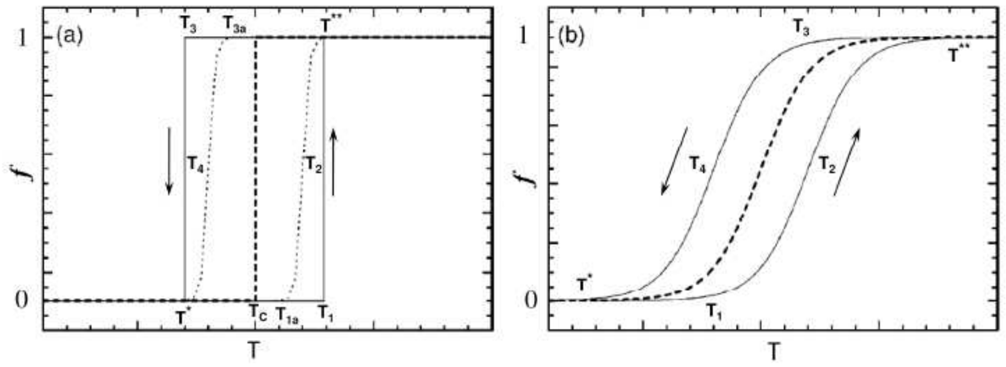

Figure 1.13: Temperature (T) dependence of phase fraction in terms of high temperature phase (f) across a FOPT. (a) The temperature cycle $T_3 - T^* - T_1 - T^{**}$ represents a transition in a pure system with sharp transition with supercooling and superheating. The temperature cycle $T_{3a} - T_4 - T^* - T_{1a} - T_2 - T^{**}$ corresponds to a diffuse transition. (b) Landscape of thermodynamical transition temperature leads to a situation where the temperature of onset of phase transition during cooling cycle (T_3) is higher than the temperature of onset of phase transition during heating cycle (T_1) (from Ref. [31]).

phase transition [26].

Disorder broadened FOPT

In an extremely pure system, an FOPT should occur at a single thermodynamical transition temperature T_C, as guided by the thick dashed line in schematic Figure 1.13(a). As discussed in earlier, such a system can be supercooled through careful cooling. In that case the phase transition follows the solid line marked by $T_3 - T^*$. Similarly, the system can be superheated and the superheated phase would follow the solid line $T_1 - T^{**}$. Still these transitions are single shot, i.e., the entire phase transforms at the same temperature; in that case, $T_3 = T^*$ and $T_1 = T^{**}$. Presence of inherent disorder or impurities in the system makes the FOPT diffused, as a result the supercooled and superheated phases will follow the dotted curves $T_{3a}-T_4-T^*$ and $T_{1a}-T_2-T^{**}$ respectively. It should be noted that in such case the two phases can coexist over a certain temperature range. Microscopic random-quenched disorder in a sample leads to a landscape of transition temperature across the volume of the sample. This can mess the sharpness of the FOPT and the transition takes place over a finite range of temperature [29, 30]. The thick dashed line of Figure 1.13(b) represents such a transition. In the presence of supercooling and superheating, the complete phase transition will follow the solid curves $T_3 - T_4 - T^*$ and $T_1 - T_2 - T^{**}$ respectively. In such broadened FOPT, the onset of nucleation of the low-temperature phase during cooling can take place at a temperature higher than the onset of nucleation of the high-temperature phase during warming [31] (see Figure 1.13(b)). It is worth to mention here that the latent heat across this typical FOPT might be difficult to be observed experimentally, and thus thermal hysteresis is also used as one of the qualifying criterion for a FOPT, as stated previously [28].

1.7 Intermetallic compounds

Intermetallic compounds are defined as the materials composed of two or more metallic elements, which exist as homogeneous, composite substances and may differ in structure from that of the constituent metals. Their physical properties need not have anything in common with those of the constituent elements. It should be noted that, alloying two or more metals may not always give rise to an intermetallic compound. First possibility is that, they may not mix in solid state reaction and remains as separate phases. Such situation occurs if the heat of mixing of the constituent elements is positive [32]. Secondly, they may produce a solid solution over a certain composition range, where the physical properties of the final product generally expected, based on linear interpolation between the properties of the parent metals. In the third case, the two metals may mix to form an intermetallic compound. Furthermore, additional intermetallic compounds' phases may grow and the system is composed of a mixture of those components. In general, the intermetallic compounds have a well defined stoichiometric composition and crystal structure. Such compounds (consisting of two elements) have general formula A_xB_y, where x and y are integers. It is to be mentioned that intermetallic compounds are different from solid solutions, where x and y may be nonintegral. Sometimes, mixing of more than two elements may form non-stoichiometric intermetallic compounds with worthy physical properties. In any intermetallic compound (stoichiometric/non-stoichiometric) the atoms of the composing elements are not distributed in a random manner over the atomic sites in the crystal lattice; rather, they are restricted to particular crystallographic sites, which are being different for each kind of atom.

1.8 Magnetism in rare earth - transition metal (R-T) intermetallic compounds

Because of the chemical similarities between rare earth (R) ions, roughly uniform behavior is observed when they form compounds with other metals. Usually, it is assumed that if one member of the rare earth series forms an intermetallic compound with certain composition and crystal structure, all the other members will follow the same. Intermetallic compounds composed of R and $3d/4d$ T have attracted huge attention due to their interesting physical properties with large number of applications, mentioned earlier [8]. The magnetic properties of these materials are analyzed by taking into account the high magnetic moments with strong magneto-crystalline anisotropy originating from the well localized R sublattice moments and strong magnetic coupling strength originating from the itinerant $3d/4d$ T sublattice.

In R-T compounds, it is well accepted that three types of exchange interactions are occurred between three different pair of ions, (i) the R-R interactions between the moments within the R sublattice; (ii) the T-T interactions between magnetic moments of the T sublattice, and (iii) the R-T inter-sublattice interactions. In general, in a compound where the T elements carry a magnetic moment, the T-T interaction becomes the strongest interaction among the above three types. But, the R-T interaction plays the most important role, it essentially determines the magnetic behaviors of the R sublattice. Furthermore, it has been found that the $4f$ spin moment of R and $3d/4d$ spin moment of T are coupled antiparallel [8, 32–34]. Therefore, the total moment of the atoms will be parallel if the orbital moment of the R is greater than the spin moment and they are opposite to each other. As a result, R-T coupling is ferromagnetic (FM) in the case of light rare earth (where $J = L - S$) and antiferromagnetic (AFM) in the case of heavy rare earth ($J = L + S$) [32]. The fact that the $4f$ spin moments couple antiparallelly to the $3d$ moments has been explained by Wallace (1968) [35]. The polarization of the conduction electrons (s or p electrons) is parallel to the more localized $3d$ spins. But, the polarization is antiparallel to the $4f$ spins, which automatically leads to an AFM $4f - 3d$ coupling . Whereas, Campbell proposed that $5d$ electrons of the R component (for Actinoids) play a significant role in the exchange interaction between the R and T [10]. According to him, the $4f$ electron spins induce a positive local moment at $5d$ electron site through ordinary $4f - 5d$ exchange. A direct $3d - 5d$ interaction obtains, which exists in normal metals. Campbell also argued that the R can be considered as belonging to the first half of a T series taking into account their d-electron character, whereas Fe, Co and Ni belong to the second half. Accordingly, the $5d - 3d$ interaction is negative so that one expects an antiferromagnetic $4f - 3d$ coupling.

1.9 Spin-orbital compensation

Among the $4f$ series rare earth based intermetallic alloys, Sm based systems have attracted special attention since most of them exhibit exotic thermomagnetic behavior. Particularly, Adachi *et al* reported a remarkable phenomenon of magnetic compensation in a specific variety of Sm systems [36],

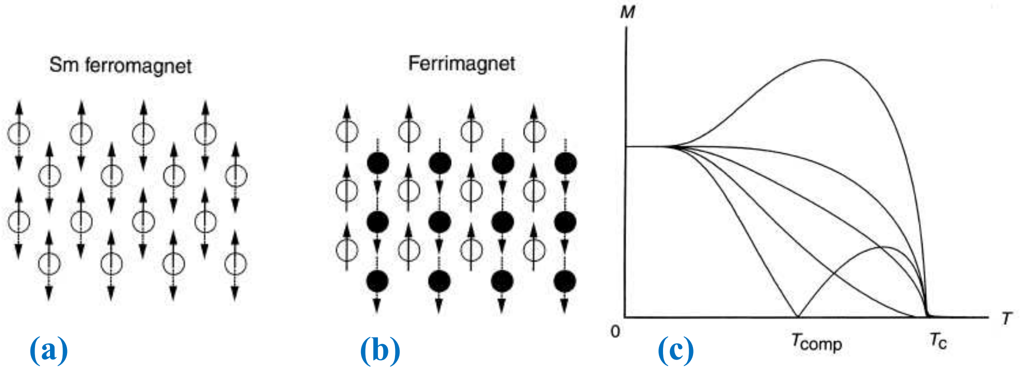

Figure 1.14: Schematic diagrams of moment alignments for (a) Sm ferromagnet and (b) usual ferrimagnet. In (a) the solid and dotted arrows denote the spin and orbital parts of the Sm^{3+} moment respectively. Figure (b) indicates the ferrimagnetic arrangements magnetic moments of two kinds of ions using open circles and filled circles. (c) The various types of the magnetization (M) vs. temperature (T) curves expected for a Sm ferromagnet and a ferrimagnet. T_C is the ordering temperature, and T_{comp} is the compensation temperature. Pictures are reproduced from Ref. [36]

which can even be driven to the zero magnetic state when a tiny fraction of Sm^{3+} ions are substituted by Gd^{3+} or Nd^{3+} ions. This exceptional property of magnetic compensation can be attributed to the unique property of Sm^{3+} ion ($4f^5$, L=5, S=5/2), in which the $4f$-spin (μ_s) and the $4f$-orbital (μ_o) counterparts of the total magnetization (M) carry comparable contributions $\sim 4\mu_B$, but coupled antiparallelly to each other. Furthermore, the complex thermal mixing of different low lying J multiplets of Sm^{3+} ions give rise to the different temperature dependency of the spin and orbital components. Thus, the combination of these two components, having different temperature dependency, make the thermomagnetic curve unique, as compared to the other rare earth based alloys. The total magnetization (M) in the Sm based systems are usually very small as the antiparallelly coupled μ_s and μ_o

almost cancel each other. Therefore the contribution of the conduction electron polarization (CEP) becomes quite prominent, compared to the total $4f$ moments of Sm^{3+} ions. It has been verified experimentally that the polarized conduction electron spin moments (μ_{cep}) align parallelly with the μ_s of the Sm^{3+} ions in metallic Sm systems [37]. The crucial role of μ_{cep} together with the complex crystalline electric field make the magnetism of Sm and its compound of interest to study. Sometimes, a complete magnetic compensation termed as spin-orbital compensation occurs at a certain temperature (T_{comp}) inside the magnetic ordered region, where the net magnetization attains zero, though the compound remains in the ferromagnetic state. These compounds are less sensitive to the applied magnetic field i.e., would provide very less dipole field and contains appreciated spin polarization, which are essential to enhance the properties of spin resolving devices (spin analyzers or polarizers), magnetic tunnel junctions etc; also attract potential interests for the underlying physics behind the compensation phenomena.

1.10 Magnetocaloric effect

In recent days, magnetic refrigeration is one of the most important applications of magnetic materials [38–43]. It has potential to become the alternative cooling process of conventional vapour compression based cooling technology, being used today. Use of environment friendly material rather than toxic gas, more energy-efficient, better adaptability, solid state nature, etc. are the advantages of magnetic refrigeration. The cooling technology of magnetic refrigeration is based on the phenomenon called magnetocaloric ef-

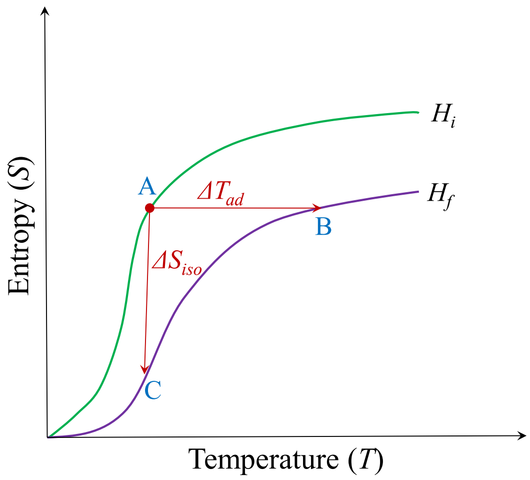

Figure 1.15: Schematic representation of entropy vs. temperature for two different magnetic field, showing the MCE and adiabatic temperature change.

fect (MCE), which is an intrinsic phenomenon of (some) magnetic materials, discovered in 1881 by E. Warburg [44]. Later, the fundamental principle of MCE for practical use was interpreted by Debye (1926) and Giauque (1927), separately [45,46]. When a magnetic material is exposed to a sufficiently high magnetic field, the magnetic moments of the constituent atoms become reoriented along the field direction. If the magnetic field is applied adiabatically, their magnetic moments become ordered and magnetic entropy decreases. Therefore, the crystalline lattice entropy should increase to compensate the lose of magnetic entropy in order to keep the total entropy constant in the adiabatic process. As a result, the temperature of the material rises. In opposite, If magnetic field has been removed adiabatically from a magnetized specimen, the temperature decreases. This warming and cooling procedure in response to the subsequent application and removal of an external magnetic field is called the magnetocaloric effect (MCE).

Now, the total entropy (S) of a magnetic material at constant pressure can be represented as

$$S(T, H) = S_M(T, H) + S_l(T) + S_e(T) \tag{1.20}$$

where S_M, S_l and S_e represent the magnetic entropy, lattice entropy due to the vibrations of crystal lattice and electronic entropy of the materials free electrons, respectively [40, 47]. In general, at constant pressure S_M is highly dependent on magnetic field and temperature but S_l and S_e depend on temperature only (negligible magnetic field dependency). It is well established that $S(T, H)$ of a usual ferromagnet increases with increasing temperature while keeping the magnetic field unchanged. However, $S(T, H)$ of a ferromagnet decreases with increasing magnetic field for fixed temperature. Figure 1.15 schematically describes the total entropy ($S(T, H)$) of a ferromagnet as a function of temperature for two different magnetic fields H_i and H_f ($H_f > H_i$). When the magnetic field is applied isothermally to a FM material ($H_i \rightarrow H_f$), followed by the path **AC** in the diagram of Figure 1.15, S decreases for the increase in magnetic ordering. The isothermal entropy change upon the field change from H_i to H_f is determined by

$$\Delta S_{iso}(T, \Delta H) = S(T, H_f) - S(T, H_i). \tag{1.21}$$

If the field is applied adiabatically in a reversible process, the S_M decreases, while the total entropy remains constant. This leads to an increase in the temperature of the material, termed as adiabatic temperature change (ΔT_{ad}), represented by the path **AB**. According to Figure 1.15, for magnetic field variation of ΔH (i.e. $H_f - H_i$), ΔT_{ad} is measured by

$$\Delta T_{ad}(T, \Delta H) = T(S, H_f) - T(S, H_i). \tag{1.22}$$

Instead of calculating from the $S(T, H)$ curves, the MCE parameters ΔS_M, ΔT_{ad} can be analytically determined in terms of magnetization (M), magnetic field (H) and temperature (T) through the Maxwell's relation

$$\left(\frac{\partial S}{\partial H}\right)_T = -\left(\frac{\partial M}{\partial T}\right)_H. \tag{1.23}$$

The magnetic entropy change (ΔS_M) is thus calculated by

$$\Delta S_M(T, \Delta H) = S(T, H_f) - S(T, H_i). \tag{1.24}$$

For a isothermal, isobaric process the above equation gives

$$\Delta S_M(T, \Delta H) = \int_{H_i}^{H_f} \left(\frac{\partial M(T, H)}{\partial T}\right)_H dH. \tag{1.25}$$

On the other hand, ΔS_M can also be approximately calculated from the magnetization data, recorded at discrete field and temperature interval using the following expression

$$\Delta S_M(T, H) = \sum_i \frac{M_{i+1}(T_{i+1}, H) - M_i(T_i, H)}{T_{i+1} - T_i} \Delta H. \tag{1.26}$$

Furthermore, one can estimate $\Delta S_M(T, H)$ from field dependent calorimetric measurements (heat capacity) at different magnetic field by the following integration

$$\Delta S_M(T, \Delta H) = \int_0^T \left(\frac{C(T,H) - C(T,0)}{T} \right) dT \tag{1.27}$$

where $C(T, H)$ and $C(T, 0)$ are the values of the heat capacity measured under an applied magnetic field H and in zero field ($H = 0$), respectively. Therefore, the adiabatic temperature change (ΔT_{ad}) can be evaluated by integrating equation (1.27) over the magnetic field range

$$\Delta T_{ad}(T, \Delta H) = -\int_0^H \frac{T}{C(T,H)} \left(\frac{\partial M}{\partial T} \right)_H dH. \tag{1.28}$$

It should be noted that ΔT_{ad} can also be calculated from equation (1.22).

From equations (1.25) and (1.27) it is worthy to state that a material should have large MCE (i.e., large ΔS_M and ΔT_{ad}) when $\left(\frac{\partial M}{\partial T}\right)_H$ is large and additionally, $C(T, H)$ has a large deviation from $C(T, 0)$ at the same temperature [48, 49]. This is due to the fact that $\left(\frac{\partial M}{\partial T}\right)_H$ peak occurs at the magnetic ordering temperature and a large MCE is often expected closed to this magnetic phase transition. It is ought to be mentioned that evaluation of ΔS_M using equation (1.26), from isothermal $M(H)$ measurements at different temperature, has been useful for a rapid screening of potential magnetocaloric materials. But for a precise comparison of the MCE among the existing magnetocaloric materials can be completely realized by the value of ΔT_{ad}, which is the measure of temperature change of a material when it is placed in a magnetic field, adiabatically.

Relative cooling power (RCP): The RCP reflects the amount of heat that can be transferred from the cold body to the hot body, in an ideal refrigeration cycle. The magnetic cooling efficiency of a magnetocaloric material for a certain magnetic field is evaluated by considering the maximum magnitude of $\Delta S_M(T)$ curve (i.e. ΔS_M^{max}) or $\Delta T_{ad}(T)$ curve (ΔT_{ad}^{max}) (keeping the magnetic field constant) and the full width half maximum (δT_{FWHM}) of the corresponding curves [40]. Based on the magnetic entropy change, RCP is the product of ΔS_M^{max} and δT_{FWHM}, as

$$RCP(S) = \Delta S_M^{max} \times \delta T_{FWHM}. \tag{1.29}$$

Similarly, the product of the maximum adiabatic temperature change (ΔT_{ad}^{max}) and the full-width at half-maximum (δT_{FWHM}) is expressed as

$$RCP(T) = \Delta T_{ad}^{max} \times \delta T_{FWHM} \tag{1.30}$$

which is the measure of RCP based on the adiabatic temperature change.

1.11 Martensite transformation and Heusler alloy

Heusler alloys are named after Friedrich Heusler who observed ferromagnetism in Cu-Mn-Al alloy, whereas all of constituent elements are non-magnetic [50]. Such ternary intermetallic compounds with stoichiometry X_2YZ are known as full Heusler alloy and the stoichiometry XYZ are known as half

Heusler alloys, where X and Y are the $3d$ T elements and Z is the group IIIA-VA element of the periodic table. The full and half Heusler alloys cystallize into $L2_1$ and $C1_b$ structure, respectively. Apart from the stoichiometry, Ni-Mn based nonstoichiometric Heusler alloys have drawn attention to the researchers leading to many interesting magnetic/transport properties, such as shape memory effect (SME), giant MCE, EB, large MR, etc. with significant technological applications associated to complex magnetism [51–57]. All the striking properties and complexity in its magnetic and transport behaviors are directly or indirectly correlated to the martensite transformation (MT). MT in Heusler alloys is a solid to solid first order magnetostructural phase transition (the change in coupling between magnetic and structural degrees of freedom), occurs from high temperature austenite to low temperature martensite phases. The martensite phase may have molulated/non modulated tetragonal, orthorhombic or monoclinic structures while the austenite is cubic $L2_1$ phase [58–65]. It has been observed that the martensite phase is more resistive than the austenite and a giant MR has been reported to be observed across the MT of Ni-Mn based Heusler compounds. As a part of this thesis work, the study of the influence of martensite and austenite phase volume fractions on the magnetoresistance have been focused across the MT of these compound. Therefore, we have avoided discussions about the other observed properties.

1.12 A brief introduction to the compounds studied in this thesis

The compounds investigated in this thesis belong to rare earth based three different intermetallic series namely $Sm_{1-x}Gd_xAg$, $ErRu_{2-x}Cr_xSi_2$, Er_3Pd_2, and one Heusler alloy $Ni_{44}Cu_2Mn_{43}In_{11}$.

1.12.1 (Sm,Gd)Ag for spin-orbital compensation

In the set of binary intermetallics, compiled with $4f$ series rare earth (R) and magnetic/nonmagnetic metal, Sm based alloys such as $SmAl_2$ [36,66,67], SmZn [68], SmCd [69, 70], $SmNi_2$ [71] exhibit unexpected magnetic behaviors, particularly when Sm^{3+} ion is partially substituted by other R ions. The observed phenomena of magnetization reversal, magnetization compensation thereto zero or negative magnetization in the magnetically ordered region, have been immensely studied for those systems. The appreciated magnetic reversal are the result of the presence of multiple antiferromagnetically or ferrimagnetically coupled magnetic sub-lattices as discussed previously. Among the various worthy system, Gd dopped $SmAl_2$ and $SmNi_2$ has been enormously studied in which T_{comp} is found to be depending upon the Gd concentration in the system [36, 71]. The temperature dependence of the spin-orbital density [72] along with the anomalies at T_{comp} [66], tunnel magnetoresistance as an FM electrode [73], ultrasonic behaviors [74], complete magnetization behavior of bulk [75–79], as well as thin films [67, 80, 81] have been revealed in ferromagnetic (Sm,Gd)Al_2 series. The study of new spin polarized material, representing very small or zero magnetization state can open a new way to maximize or to play with the degree of spin polarization. We have found that the compound SmAg undergoes FM transition around 50 K and its thermo-magnetization curve depicts partial spin-orbital compensation like behaviour. Now, a solid substitution of Gd^{3+} ($4f^7$, L=0, S=7/2) onto the Sm site in SmAg, introduces a comparable large spin moment ($7.6\mu_B$) and increases the CEP in the system. This can affect the existing CEF and perturb the RKKY interaction, cause the localized $4f$-spin moments of Sm^{3+} are coupled to the spins of Ag conduction electrons via indirect RKKY interaction. As a result the J states are renormalized, which modifies the temperature dependencies of $4f$-spin and orbital moments from those of parent SmAg and could get different magnetization behavior for various Gd concentrations.

1.12.2 $\mathbf{ErRu_{2-x}Cr_xSi_2}$ compound

In order to search for new and better magnetocaloric materials, ternary intermetallic RT_2X_2 (where R is rare earth, T is transition metal and X is Si/ Ge) series are found interesting for the interplay between $4f$ and $4d/3d$ magnetism. It has been evident that the structures of RT_2X_2 compounds are composed of a sequences of parallel planes along the tetragonal c axis, likely R-X-T-X-R-X-T-X-R-..., where each plane is constructed with identical atoms (as shown in Figure 1.16). It is also a well established fact for those compound that the existing magnetic interactions are strongly correlated with the inter layer spacing of R-R or T-T planes [82,83]. Additionally,

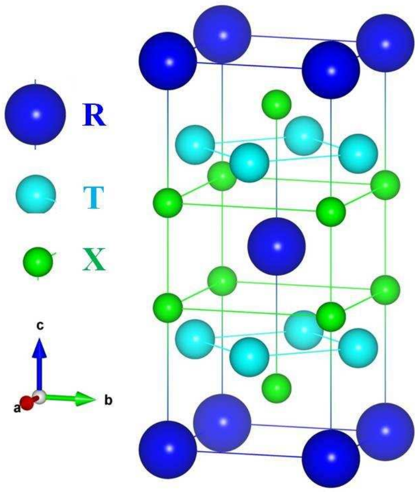

Figure 1.16: Crystal structure of RT_2X_2 compounds.

the presence of frustrated magnetic (RKKY) interactions and large uniaxial magnetic anisotropy, originated from the crystalline electric field (CEF) effect [84, 85], have also drawn special attention, because it yields a complex magnetic structure in low temperature [86,87]. Apart from the magnetocaloric effect (MCE) [88–90], the materials often exhibit various interesting physical properties, such as exchange bias effect (EBE), magnetoresistance (MR), Kondo effect [91], heavy fermionic behaviours [92], superconductivity [93–95] etc. along with multi step metamagnetic processes and mixed magnetic structures [84, 85]. Among the series, $ErRu_2Si_2$ has been reported earlier as one of the desired compound to exhibit considerable MCE around it's antiferromagnetic (AFM) transition temperature ($T_N =$) 6 K (T_N: Néel temperature), which is first order magnetic transition (FOMT) by nature. It does not contain any thermal hysteresis in the thermomagnetization data $M(T)$ [90,96]. Neutron diffraction at low temperature (upto 1.8 K) confirms the AFM nature [97,98] of the compound. Further studies revealed that, with the application of magnetic field the AFM interaction weakens, consequently the transition temperature reduces and the resistivity value also decreases in that temperature region, possibly due to the disappearance of magnetic super zone gap [96]. Beyond a certain field $H = 4$ kOe the AFM ordering is being reduced down to 2 K and resulting a field induced ferromagnetic transition [90]. To improve the MCE properties, we intend to revise the interaction of the $4f$ R (Er) with $4d$ T (Ru) upon partial replacing of one $3d$ T (Cr) in position of Ru, this would alter the inter layer spacing of R-R or T-T planes along the c axis and expects a modification in the existing AFM interaction.

1.12.3 Er_3Pd_2 compound

In case of MCE related research, the materials having FOMT have been extensively studied because of its large magnetic entropy change (-ΔS_M) value across the transition region, as example $Gd_5Si_{4-x}Ge_x$, $LaFe_{13-x}Si_xH$ and MnFeP (As, Ge), $ErRu_2Si_2$ [90, 99–105]. However, the feasible applications of such materials has been constrained for the narrow transition width, i.e. usually FOMT occurs with a sharp manner in a small temperature region. This detoriates the adiabatic temperature change (ΔT_{ad}) value, which determines the effective working temperature region of the samples. Another discrepancy is that FOMT usually accompanies by thermal and magnetic hysteresis losses, and hence leads to the irreversibility in -ΔS_M and ΔT_{ad} curves. This can drastically reduce the relative cooling power (RCP) value of the materials. Therefore, it becomes necessary to research about new magnetocaloric materials, having broad magnetic transition with no thermal or magnetic hysteresis and providing considerable -ΔS_M value. In this respect, it has been evident that materials, associated to SOMT, display comparatively low (with FOMT materials) but highly reversible MCE throughout its broadened magnetic transitions. This makes the effective working temperature region large, in other ways enhance the RCP value as well as the efficiency of the desired MCE properties. Various rare-earth based compounds have been vigorously studied in recent past for active magneto-refrigerant materials, some of them have proved their capability to become the potential applicants such as ErRuSi, $TbMn_2Si_2$, $TmMn_2Si_2$, TmZn, TmZnAl, TmAgAl, Gd_2Cu_2Cd, Er_2Cu_2Cd, etc. [106–112]. Beside that, another notable category with table shaped MCE, where the -ΔS_M value remains almost unchanged over a wide temperature regime, has been reported in some compounds with multiple phase transitions and sometimes in composite materials [113–117]. Consequently those materials exhibit large RCP values, though -ΔS_M is not so large in some specific cases. Targeting to discover new Er based MCE materials having SOMT at low temperature, we have found that the binary intermetallic Er_3Pd_2 was known for a long time having AFM transition near 10 K but less studied of it magnetic properties. The study has attracted our attention as the compound exhibits a large reversible MCE associated with a SOMT at low temperatures (around 10 K). The results have been further compared with Heat capacity study.

1.12.4 MR with various phase fractions across the martensitic transformation

It has been evident that the existing MT in a system can be tuned by several external parameters such as annealing temperature, pressure and magnetic field apart from tuning the stoichiometry in Ni-Mn based Heusler compounds [52, 53, 55, 118–123]. The presence of inherent disorder in the parent austenite phase makes the MT occur over a range of temperature, rather than a sharp value; this range is termed as transition width (TW). Thus, within the TW of MT, both the austenite and martensite phases coexist in a metastable state [124, 125]. It has been discussed earlier that the martensite phase is more resistive than the austenite and a GMR has been observed across the MT of these compounds, like the multilayer systems. Though the later has a different origin for its large MR [54, 58, 126]. To compete with the existing technology, based on GMR of multilayers systems, one has to improve the MR behavior of these martensite Heusler compounds. This can be achieved either by synthesizing new materials or finding out a route to manipulate the MR behavior of the existing MT materials, for better applications. We have attempted to explore a convenient route to control the MR behavior of a given martensite compound, by manipulating the phase volume fractions of austenite and martensite phases across the MT under different magnetic fields. As mentioned earlier the austenite and martensite phases have different crystal structures and consequently, the source of electron scattering and the density of scattering sources are different, which leads to the distinct magneto-resistive behavior of these phases. Therefore, tuning of the phase fractions within the MT is one of the key parameters to control the MR in these type of compounds. Now to quantify the phase volume fractions of austenite and martensite phases over the TW of MT, resistivity option has been selected as our main tool. With this said motivation, reported martensite Heusler compound $Ni_{44}Cu_2Mn_{43}In_{11}$ [58] has been considered as a representative of all martensite Heusler compounds, which show large MR across the MT [118–123]. These type of compounds make transition from ferromagnetic austenite to nearly paramagnetic or antiferromagnetic martensite phases. $Ni_{44}Cu_2Mn_{43}In_{11}$ compound exhibits MT from body-centred cubic (Fm-3m) austenite to non modulated tetragonal (I4/mmm) martensite phase around MT temperature (T_M=) 270 K [58]. The phase volume fractions of martensite ($f_M(T,H)$), austenite ($f_A(T,H)$) and field induced austenite ($f_{IA}(T,H)$) phases are quantified across the TW of MT under different applied magnetic fields (H) [127]. Furthermore, The role of this different phase fractions on the observed MR have been studied.

Chapter 2

Experimental details

This section includes the preparation of various polycrystalline intermetallic samples and characterization techniques along with the experimental methods, used for crystal structure determination and investigation of various physical properties, e.g. magnetic, electrical, thermal properties and heat capacity.

2.1 Sample preparation

All the intermetallic alloy samples were prepared in an arc melting furnace under high purity inert argon gas atmosphere. The working of arc melting furnace in short with sample preparation are described below.

2.1.1 Arc melting furnace

Centorr Vacuum Industries make 5TA tri-arc furnace (shown in Fig. 2.1) [128] has been used to prepare samples for the present study. This furnace

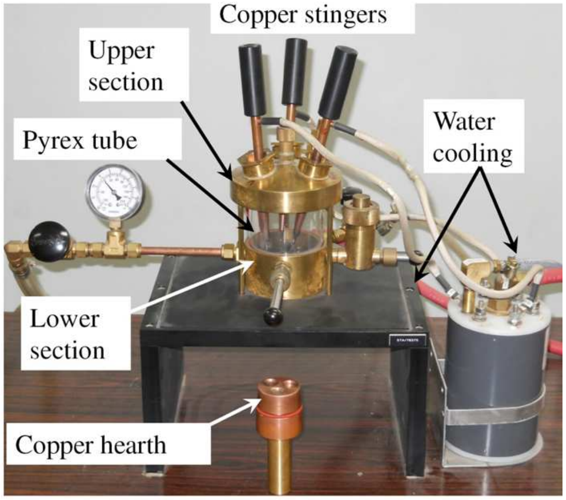

Figure 2.1: Arc melting furnace model 5TA.

consists of two main sections, upper and lower, with water cooling arrangements, and separated by a pyrex observation tube. A copper hearth, with starting materials for a sample placed on it, is attached to the lower section and connects to one electrical polarity. Three copper stinger rods penetrating the top section (through swivel ball for vertical and angular movement) which carry tungsten electrodes, they are of opposite electrical polarity. A mechanical pump is attached for evacuation prior to inert gas backfilling. Separate ports are provided for inert gas inlet and outlet valve also.

Constituent elements (Alfa Aesar), in stoichiometric proportion, of at least 99.9 % purity for rare earth metal and 99.995 % minimum purity for the other, were loaded on the water cooled copper hearth in a purified argon gas environment, and purged the chamber several times. Thereafter, the melting has been carried out by discharging an electrical arc between the two electrodes (pointed tungsten rod to the copper hearth) in the chamber, under the continuous flow of argon gas. The resulting ingots were flipped upside down and remelted four to five times to ensure the homogeneity. The weight losses have been strictly monitored at end of the melting process. Iff the loss is less than 1 % of the total weight before melting, the samples are considered for performing heat treatment and further characterization.

2.1.2 Heat treatment

The as-cast samples were encapsulated in evacuated quartz tubes. The tubes were flushed several times with argon gas, and a vacuum of 10^{-5} torr were ensured before the sealing. The sealed samples were then annealed at a specific temperature for a certain period of time. Whereas, the annealing temperature and time varies for different systems. This process helps to eliminate any micro-segregation of secondary phases by solid state diffusion and allow the systems to establish better chemical homogeniety with full structural order. The annealed samples have been cut into small pieces using slow speed diamond saw and proceed for structural characterizations.

2.2 Powder X-Ray diffraction

X-Ray diffraction (XRD) is a versatile technique for structural characterization (i.e. crystal structure, phase composition, lattice spacing) of a material. Incident x-ray beam on a crystal lattice are scattered from the parallel crystal planes and wherever interfere constructively, appears as a peak in the diffraction pattern. The condition for the constructive interference is given by the Braggs formula, $2d_{hkl}sin\theta = n\lambda$. where, λ is the wavelength of the incident x-ray beam, n is the order of diffraction, θ is the angle between the incident x-ray and the scattered plane, and d_{hkl} is the inter-planar spacing between the parallel crystal planes, where (hkl) are the Miller indices [2,129,130]. It describes the orientation of the crystal planes in a lattice, and the parallel planes are defined by the same Miller indices. It should be noted that each crystalline material has a unique atomic structure, thus it will produce a characteristic diffraction pattern.

X-ray lab source

The structural and phase purity analysis of the annealed samples were performed by collecting the room temperature (RT) powder XRD patterns, obtained using Cu-k_α radiation ($\lambda = 1.54182$ Å) in a Philips PW-3020 diffractometer. A small piece of sample was finely grounded in a ceramic mortar-pestle to make powder. Thereafter, the XRD data were collected at constant step in scattering angle 2θ.

X-ray synchrotron source

RT and temperature dependent XRD of some of the samples (powder) have been carried out using Synchrotron radiation in BL-12, INDUS-II, RRCAT, India and Indian Beamline, PF, KEK, Japan. Synchrotron radiation (also known as synchrotron light) is electromagnetic radiation that is emitted when moving charged particles, at close to the speed of light, are forced to change direction by a magnetic field. Synchrotron is an extremely powerful source of X-rays, and produced by high energy electrons as they circulate in the storage ring around the synchrotron. It is useful in the form of x-rays for a wide frequency range, high brightness (many orders of magnitude brighter than conventional lab sources), highly polarized, tunable and collimated. Because of its high brilliance/brightness the measurement can be carried out at very short time. This helps in studying the dynamic processes as a function of external physical parameters such as temperature, pressure or magnetic field.

Rietveld refinement of the XRD patterns have been performed using *Fullprof* software to determine the phase purity (also detection of any impurity phases) and to calculate the lattice parameters of the samples. In the *Rietveld* method the least squares refinements are carried out until the best fit is obtained between the entire observed diffraction pattern for the lattice parameters and crystal structures.

2.3 Energy dispersive X-Ray spectroscopy

Energy Dispersive X-ray Spectroscopy (EDS) is one of the primary analytical technique to determine the relative concentrations of the atoms present in a sample , i.e., to provide a rough estimation of the elemental composition [131]. When a high energy electrons beam incident on a sample, there is a finite probability that one incident electron expels a bound electron of an atom, and creates a vacancy in the particular level. If the ejected electron is from an inner shell, the electrons from the outer shell jump into the level to fill the vacancy by emitting energy in the form of electromagnetic radiation. For the ejection of an electron from the k shell results the characteristic x-ray emission of that element. Hence, the number of the x-ray and energy both are measured with the energy dispersive analyzer. Therefore, from the energy of the emitted x-rays, the elements present in the sample are identified and from the intensity of the emitted x-rays, the relative fraction of the elements in the sample are determined. The information, we obtained from the EDS, is used for qualitative analysis of the elemental composition of the sample.

2.4 Magnetization measurement

To study the magnetic properties of a material, Experimental measurement of magnetic moment is required to find out the magnetization. Magnetization (M) is defined as the magnetic moment per unit volume. Directly, magnetic moment of a specimen can be measured by two techniques. (i) Force technique, which determines the force/torque on a magnetized sample and (ii) flux technique, which involves determining either the magnetic flux or the rate of change of the magnetic flux linked with the magnetized material [22]. The examples of force techniques are Faraday balance, torque magnetometer etc., while the flux techniques includes vibrating sample magnetometer (VSM), Superconducting Quantum Interference Device (SQUID) magnetometer etc. There are various indirect methods to determine the magnetic moments, through the known relationships of some physical phenomena, associated with the magnetic properties of the specimen; such as, Hall Effect, magneto-optical Kerr effect, Faraday effect, nuclear magnetic resonance, ferromagnetic resonance, Mossbauer effect, neutron scattering, muon spin resonance etc. In the present work, for DC and AC magnetization measurements, we have used a VSM attached with Physical Property measurement system (PPMS), and SQUID-VSM (SVSM), both are under the category of flux measurement technique. Temperature (T, 2 to 300 K) and magnetic field dependencies of DC magnetization data have been collected in several measurement protocols, such as zero field cooled warming (ZFCW), field cooled cooling (FCC) and field cooled warming (FCW).

ZFCW: In ZFCW protocol, initially, the materials are cooled down to lowest possible temperature without applying any magnetic field, then the measuring magnetic field is applied and $M(T)$ has been started to record during warming.

FCC: In this protocol, The $M(T)$ data are taken during cooling from room temperature or from the paramagnetic state, under a given applied field.

FCW: In FCW mode, materials are cooled under a certain H and the $M(T)$ data are measured in subsequent warming the material, while keeping the cooling H on.

ZFC MH: For zero field cooled (ZFC) M-H measurements, each time, the samples are first cooled down to the required temperature from paramagnetic region in absence of any H, then $M(H)$ is measured isothermally with varying H up to a certain value of positive and negative applied field (five quadrant).

2.4.1 Vibrating sample magnetometer (VSM)

Most of the DC magnetization measurements of the thesis have been carried out using a commercial VSM attached with PPMS (Quantum Design (QD), Model 6000). In PPMS, the magnetic field is generated by a superconducting solenoid, immersed in liquid Helium, with maximum achievable field ±90

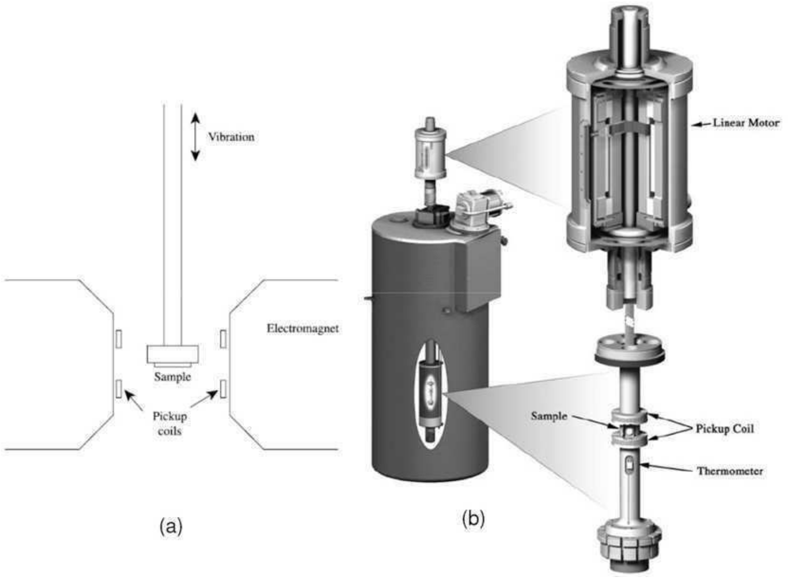

(a) (b)

Figure 2.2: Schematic diagram of VSM probe of PPMS (QD).

kOe. The working principle of a VSM is based on the Faraday's law of electromagnetic induction [132]. The sample is attached to one end of a nonmagnetic rod and kept in the vicinity of a detection coil or pick up coil; the other end is attached to mechanical vibrator. A periodic vibration of a magnetized sample causes a periodic change in magnetic flux linked with the detection coil and this change in flux induces an ac voltage in the detection coil. The magnitude of the produced ac signal is proportional to the magnetic moment of the sample, the amplitude and the frequency of the oscillation, the distance between the sample and the detection coil. However, to separate the contribution of magnetic moment from the picked up ac signal, pick-up voltage is fed to one of the inputs of a differential amplifier. This is a universally accepted technique for magnetization measurement, developed by Foner [133]. A schematic representation of a VSM configuration in PPMS is shown in Figure 2.2. Basic set up of VSM consists a VSM linear motor transport to oscillate the sample, a detecting coil puck, an electronics module for driving the linear motor and to analyze the response from the pickup coils, and the whole application is automated through software control. Usually, the frequency of the oscillation is $\sim$ 40 Hz and amplitude is normally $\sim$ 2 mm (could be ranged from 0.5 to 5 mm). This system provides very fast measurements with enough sensitivity to detect the DC magnetization of the sample down to $\sim 10^{-6}$ emu.

2.4.2 SQUID-VSM (SVSM)

In the present work AC magnetic susceptibility with some of the DC magnetic measurements have been carried out using Magnetic Properties Measurement System, MPMS SQUID-VSM, QD. The SVSM used in this work provides a temperature range of 1.8-400 K and maximum fields upto 70 kOe. SQUID magnetometer is based on the tunneling of superconducting electrons across the Josephson junction, a very thin insulting gap between two superconductors, that supports a super current below a critical value I_c. It deals with the properties of electron-pair wave coherence throughout the junction to detect very small magnetic field or magnetization. The basic element of a SQUID magnetometer is a superconducting metal ring consisting of two Josephson junctions, as shown in Figure 2.3(a). Applying a small current (I) to the SQUID, allows Cooper pairs of electrons to tunnel through the junctions. If magnetic flux is passed through the loop, it changes the relation between the phase difference of the super current across the two junctions, and as a

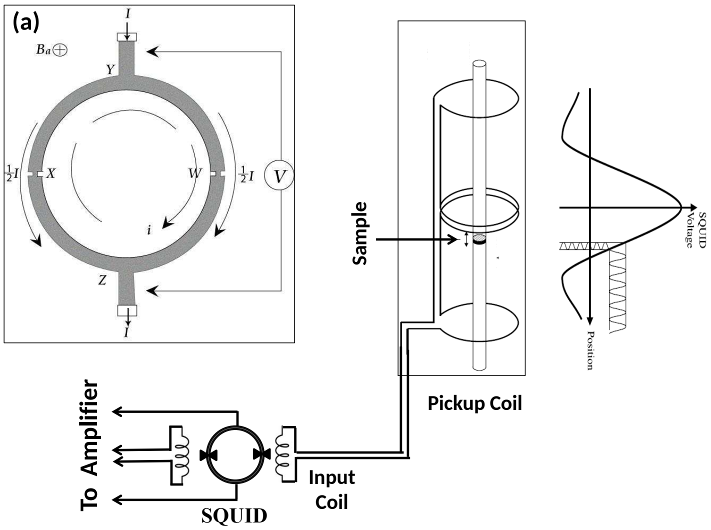

Figure 2.3: Schematic diagram to represent the working principle of SQUID in SQUID-VSM. Inset shows A SQUID with two Josephson junction as a simple magnetometer [134].

result I_c is also changed. This gives rise to a voltage across the loop that can be detected. Another important fact is that the critical current for the array of two Josephson junctions is periodic in field units of $h/2e$ due to the quantum interference effects of the electron pair wave functions. A simple SQUID can detect incredibly small magnetic flux, therefore it would detect the flux from the earths magnetic field, as well as any flux from the magnet of the magnetometer or nearby magnetic systems. Hence, to use the SQUID more efficiently, a gradiometer (pickup coil) is used to detect the gradient of the magnetic flux and the gradiometer is connected using superconducting wires with the SQUID, which is protected by superconducting shielding [134–136]. A schematic diagram of SQUID magnetometer is shown in Figure 2.3. In SVSM, using the same techniques of producing ac voltage in the pick up coil (gradiometer) of VSM by oscillating a magnetized sample, a superconducting gradiometer is used. A superconducting gradiometer measures the induced ac signal which is proportional to the magnetic moment of the sample only, and has quadratic dependence on the amplitude of the oscillation and is frequency independent. The signal from the pickup coil is fed to SQUID through the superconducting input coil. The variations of current in the detection coils produce corresponding variations in the SQUID output voltage. This voltage is then amplified and read out by the MPMS electronics and obtains the magnetic moment of the sample. SVSM can take magnetic measurements at the speed of VSM with sensitivity $\sim 10^{-8}$ emu and it typically runs at a fixed frequency of about 14 Hz.

2.4.3 AC magnetic susceptibility

AC susceptibility is a versatile method to measure the dynamic magnetic response of a material in the presence of a small ac magnetic field, superimposed on the dc field. Dynamic response of susceptibility yields information about the magnetization dynamics of different classes of magnetic materials such as spin-glass, cluster-glass, ferromagnetic and antiferromagnetic materials. To reveal various magnetic phase transitions, the study of dynamic susceptibility is important as a function of frequency (f) and amplitude to ac magnetic field. The change in flux due to the time dependent moment induces a current in the pick-up coil (the same for dc magnetization measurement in SVSM), allowing measurement without sample motion. In the case of very low frequencies and very low field, the ac magnetic measurement is very similar to the dc measurement and in this case, the magnetic moment of the sample follows the same $M(H)$ curve obtained in a dc experiment. The detecting signal $\frac{dM}{dH}$, the slope of the M(H) curve, is proportional to χ_{ac} (ac susceptibility). When the ac field is small, the induced ac moment can be written as

$$M_{ac} = \frac{dM}{dH} H_{ac} sin(\omega t) \tag{2.1}$$

where H_{ac} and ω are the amplitude and frequency of the ac field, respectively. At higher frequencies, the ac moment of the sample does not follow the dc $M(H)$ curve due to the dynamic field effects in the sample and the magnetization lags behind the driving field. Hence, another quantity ϕ, the phase difference with respect to the driving field signal, has to be introduced in χ_{ac}. Therefore, χ_{ac} corresponds to the combination of a real or in phase component (χ') and an imaginary or out of phase component (χ''), expressed as

$$\chi' = \chi_{ac} cos\phi, \tag{2.2}$$

$$\chi'' = \chi_{ac} sin\phi. \tag{2.3}$$

The imaginary component indicates any dissipative process in the sample. Relaxation and irreversibility in spin glass give rise to a nonzero χ''. In ferromagnets, a nonzero χ'' is an indication of irreversible domain wall movement or absorption due to permanent moments. In the present thesis, χ_{ac} was measured for some samples in SVSM with different frequencies.

2.5 Electrical resistivity

Electrical resistivity (ρ) of a material at any temperature arises due to the scattering of conduction electron-phonon along with electron-electron, atomic and magnetic disorder with strain, band structure, etc. Temperature and magnetic field variation of resistivity of a magnetic material can provide us important information about its magnetic state. Resistivity changes during any magnetic transition due to reduction of scattering in magnetically ordered state or vice versa and the same occurs for any structural transition also. Magnetoresistance (percentage change in resistivity due to presence of a magnetic field) can reveal the information about existing magnetic interactions, because the change in resistivity with magnetic field depends on the nature of magnetic order in the material.

Linear four-probe resistivity measurement is a very common, standard and accurate experimental technique for electrical resistivity measurement. This method provides low resistance at the contacts and leads at the time of measurement [137]. Four independent electrical contacts are made on the any one surface of a (rectangular bar shaped) sample along a line, using silver epoxy paint. A constant electric current is allowed to flow through the two outer terminals and the resistance (R) is calculated between the two inner terminals by measuring the voltage drop across them. Now the resistivity of the material can be obtained from the following relation

$$\rho = \frac{td}{l} R. \tag{2.4}$$

Where t is sample thickness, d is width of the sample, and l is the spacing of the two inner terminals. Resistivity measurements of some of the samples were carried out in PPMS in the temperature range $T = 2{-}300$ K in a magnetic field up to 50 kOe.

2.6 Heat capacity

Heat capacity measurement is a necessary technique to reveal the lattice, electronic, and magnetic properties of materials for the study of bulk samples. It also explores several important informations regarding magnetic ordering, entropy, phase transition, etc. The heat capacity of some of the samples at constant pressure have been carried out in PPMS by relaxation method, in the temperature range 2−120 K and with applied magnetic field up to 50 kOe. The heat capacity at constant pressure is given by $C_p = (\frac{dQ}{dT})_P$, where Q is the heat energy put into the sample system and T is the sample temperature at constant pressure P. In thermal relaxation technique the sample is heated for a fixed time length providing a constant heating power and then allowed to cool for the same duration, keeping the heater power off. The PPMS heat

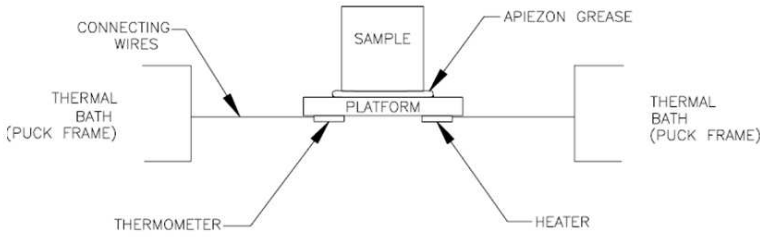

Figure 2.4: Schematic diagram of the thermal connections for heat capacity measurements in PPMS [138].

capacity option controls the amount of heat applied to and removed from the sample; it also records the sample temperature throughout the heating and cooling cycle and performs the fitting with the thermal relaxation model [139] to extract the heat capacity of the sample.

As described in Figure 2.4, a platform heater and a platform thermometer are attached to the bottom of the calorimeter chip which basically acts as the sample platform. The sample is mounted on the platform by using a thin layer of standard cryogenic grease/adhesive, such as Apiezon N grease for measurement $\leq$ room temperature and H grease for $>$ room temperature, for good thermal contact to the platform. Electrical connections to the platform heater and platform thermometer have been provided through eight small wires and they also assure the thermal connection to the heat bath (puck frame) and structural support for the platform. During the measurement the set up should be kept at high vacuum ($\sim 10^{-5}$ Torr), which is usually maintained by cryopumping in PPMS, to ensure that the thermal conduction between the sample platform and the thermal bath is purely dominated by the conductance of the connecting wires. So that it can build a reproducible heat link to the bath with enough large time constant, which allows both the platform and the sample to achieve good thermal equilibrium at the time of the measurement [138]. For heat capacity measurement at any temperature, at first the sample platform temperature and puck temperature are stabilized at that initial temperature. Then power is applied to the platform heater for a predetermined time period to rise the sample platform temperature. Then the power is terminated and the temperature of the sample platform is allowed to relax towards the heat bath (puck) temperature.

The sample platform temperature is monitored throughout the heating and cooling process and provides the raw data of the heat capacity calculation. The raw data is analyzed by simple single τ model, which assumes perfect thermal coupling between the sample and the sample platform. It considers the thermal relaxation time period (τ) between the sample platform and the puck. A second analysis is also performed using the two-τ model, which has been developed assuming that the sample is not in good thermal contact with the sample platform. In this model, the first time constant (τ_1) represents the thermal relaxation time period between the sample platform and the puck, and the second time constant (τ_2) represents the relaxation time period between the sample platform and the sample itself. The obtained values of the heat capacity and other physical parameters are optimized with the agreement between the measured data and the two-τ model. The heat capacity software determines which model fits best to the measured data. It should be noted that, before mounting the sample on the platform, addenda measurement is necessary, where a small amount of grease is applied on the centre of the platform and the heat capacity of that small amount of grease and the sample platform is measured. Finally, the heat capacity of the sample is determined by subtracting the addenda from the total heat capacity, measured with placing the sample on the platform.

2.7 Hall effect

From the Hall coefficient study, the density and type of the charge carriers in a material can be determined. Often, the type of the charge carriers or the

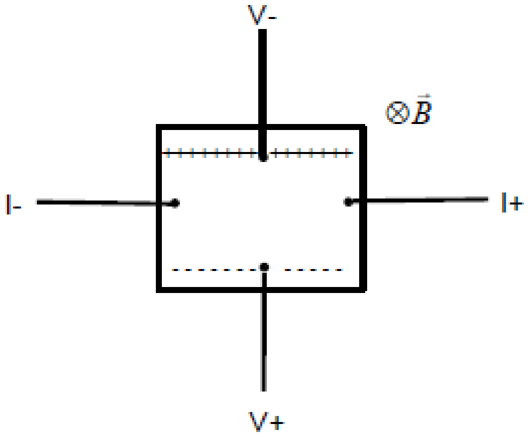

Figure 2.5: Schematic of Four probe Hall effect measurement for regular shaped sample with negative charge carriers. Picture taken from Ref [140].

density exhibits drastic changes across some kind of phase transitions (e.g. metal to insulator transition in pyrochlore iridates). Therefore, it becomes necessary to study the Hall effect for a good physical interpretation. For measurements, a transverse current is allowed to pass through a sample in a longitudinal magnetic field. The charge carriers often gather on one edge of the sample and disappear from the other edge, leading to a potential difference (Hall potential) across the sample, see Figure 2.5. The sign of the Hall potential generally indicates the type of the charge carriers (electron or hole), and the magnitude of the Hall potential is related to the density of charge carriers in the sample, as described in the following equation

$$R_h = E_h/jB = V_hA/IlB \tag{2.5}$$

Here E_h is the generated Hall electric field, V_h is the Hall potential, j is the current density given by I/A (current divided by the sample cross section), and l is the separation of the transverse voltage leads. It can be shown that $R_h = \frac{1}{nq}$, where n represents the carrier density, and q representing the charge of the carriers. Hall coefficient has been measured in PPMS using AC transport option.

2.8 Seebeck coefficient

Thermal conductivity (κ) and Seebeck coefficient (S) Can provide considerable information about the electronic as well as the ionic lattice structure of a material. The κ is a measure of the heat conduction ability of a material, so measuring this quantity one can get information about scattering of heat-carrying phonons and electrons. The S describes the thermal diffusion of free charge carriers (electrons or holes), which creates an electric field inside a material when a temperature gradient is sustained. Much like the electrical resistivity, this property is very sensitive to subtle changes in the electronic scattering processes and can be a powerful probe to study magnetic ordering. Seebeck coefficient measurement has been carried out in PPMS using the thermal transport option (TTO). The thermal and electrical connections for an idealized TTO sample are shown in Figure 2.6. For thermal conductivity and Seebeck coefficient measurements, heat is applied to one end of the sample by running current through the heater (Q+/−). The temperatures T_{hot} and T_{cold} are measured at the thermometer shoes and ΔT ($= T_{hot} - T_{cold}$) has been obtained. Also during the heat pulse, the Seebeck voltage ($\Delta V = V_+ - V_-$) is monitored. Heat exits from the sample to the cold foot. By definition $S = -\frac{\Delta V}{\Delta T}$. Time traces of ΔT and ΔV during

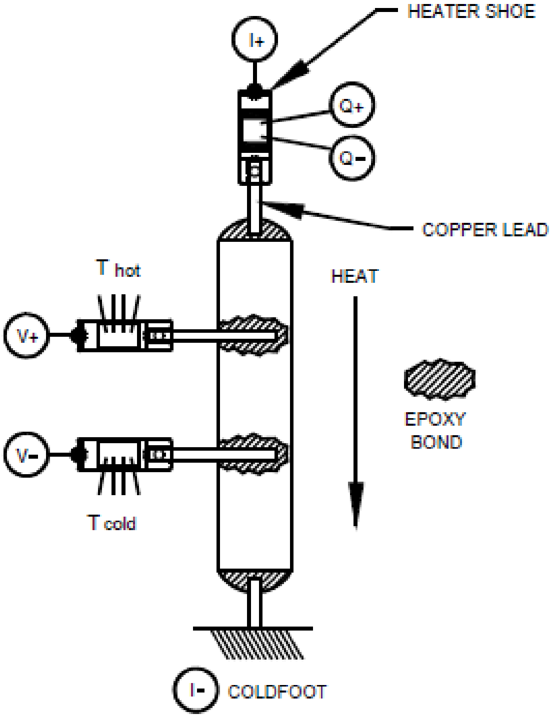

Figure 2.6: Schematic diagram of the thermal and electrical connections to the samples with heater and sensors for Seebeck coefficient measurements in PPMS. T_{hot} and T_{cold} are the temperatures of the two Cernox chip thermometers. V+ and V− are the two voltage leads, I+ and I− are the two current leads and Q represents the heater terminal. Picture taken from Ref [141].

the heat pulse are measured and a linear least-squares routine fit to the data obtains the Seebeck coefficient [141].

Chapter 3

Spin-orbital magnetic moment compensation in (Sm,Gd)Ag

In this chapter, the unique magnetic compensation behavior of Gd doped SmAg has been represented. SmAg undergoes a ferromagnetic transition around 50 K, with a small Gd doping the system shows partial magnetic compensation in the magnetically ordered region. This phenomena has been studied through AC magnetic susceptibility, heat capacity, resistivity, thermal and magneto-transport properties.

3.1 Structural analysis

It is evident from the room temperature (RT) XRD pattern (FIG. 3.1(a)) of the annealed samples (at 600° C for 175 h) that most of the peaks could be indexed with a simple cubic (SC) crystal structre (CsCl type, space group Pm$\bar{3}$m), except for few tiny peaks corresponding to the unreacted Sm phases,

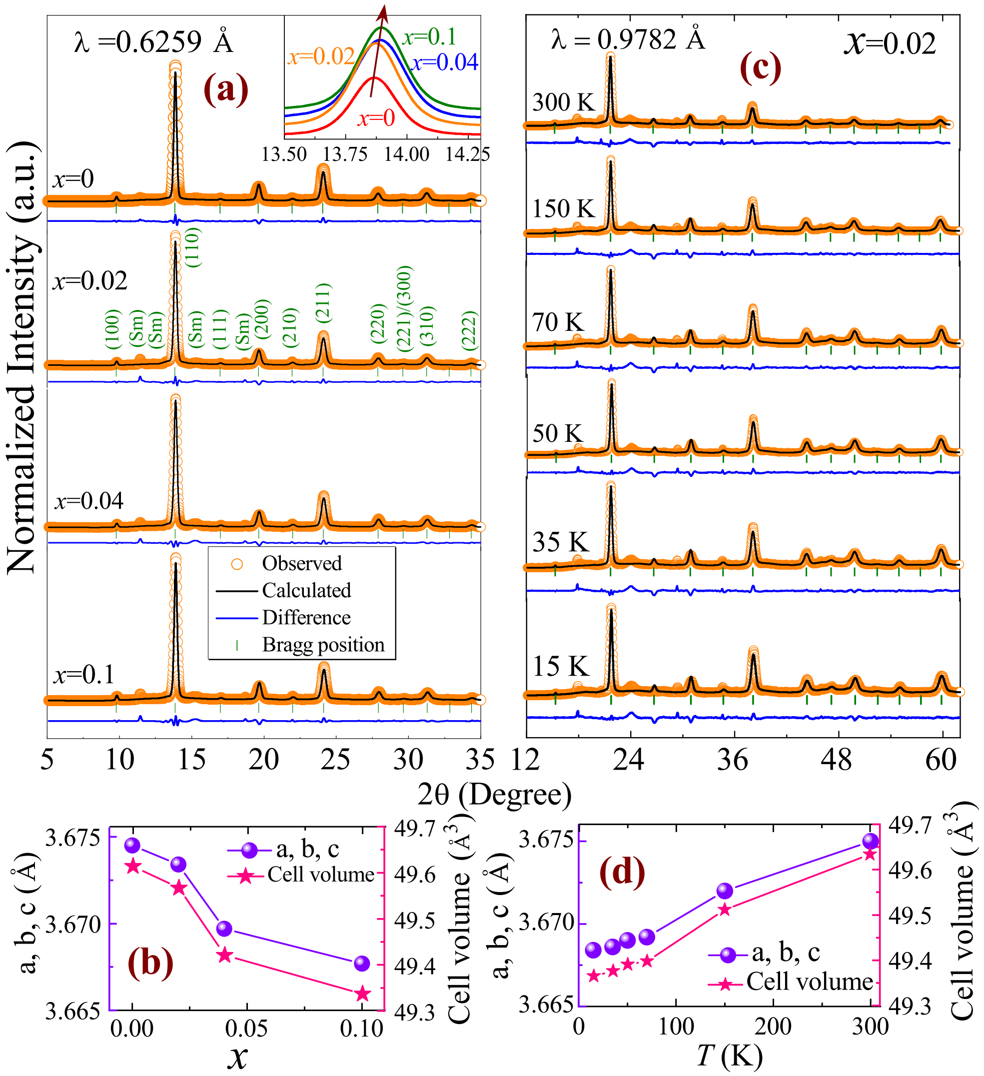

Figure 3.1: XRD using synchrotron radiations. (a) Room temperature XRD data of the annealed samples for various Gd concentrations (x) and inset shows the shift of the main peak with x near $2\theta = 13.8°$. (b) Variation of lattice parameters with x. (c) Temperature dependent XRD data of the $x = 0.02$ composition (unannealed) and (d) the shift of lattice parameters with temperature.

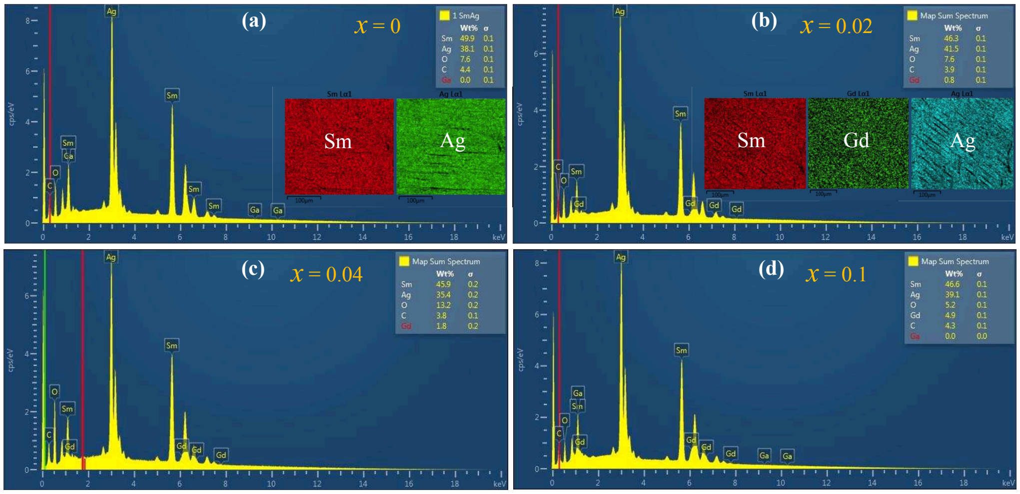

Figure 3.2: Energy dispersive X-ray spectra of all the samples indicating the weight percentage of the constituent elements. Observed C and O may have come from the polisher needle and from the oxide layer, which may form on the sample even if it has been kept in air for few minutes, respectively.

which are found in greater amount in the temperature dependent XRD (Figure 3.1(b)) of the unannealed $x = 0.02$ sample. 3.1 % unreacted Sm impurity has been calculated for the parent $x = 0$ compound and for the other it is $\lesssim 6$ %. Such impurity phases may be reduced by optimizing the annealing procedure. As shown in the inset of Figure 3.1(a), the most intense (110) peak near 13.8° has a prominent shift to higher angle with increase of Gd concentrations (x). Rietveld refinement study yields the lattice parameters are slightly decreasing with x, as shown in Figure 3.1(b). This behavior is expected due to the smaller atomic radius of Gd. For all the profile fitting the χ^2 values were lied between 8 to 10. Furthermore, no prominent peak shift or peak modification in the temperature dependent XRD (RT to 15 K) of the $x = 0.02$ compound confirms that, no structural transition has been occurred in that temperature regime. The observed reduction in lattice

Table 3.1: Calculated atomic percentage (AP) value from the weight percentage (WP) of the constituents in Figure 3.2.

Comp.	$x = 0$		$x = 0.02$		$x = 0.04$		$x = 0.1$	
Const.	WP	AP	WP	AP	WP	AP	WP	AP
Sm	49.9	21.74	46.3	20.56	45.9	17.09	46.6	22.35
Gd	0	0	0.8	0.34	1.8	0.64	4.9	2.25
Ag	38.1	23.13	41.5	25.69	35.4	18.37	39.1	26.14
C	4.4	24.02	3.9	21.7	13.2	17.72	4.3	25.84
0	7.6	31.11	7.6	31.72	3.8	46.18	5.2	25.43

Table 3.2: Obtained Gd concentration from the EDS study.

Composition	calculated Gd %	Experimental Gd %
$x = 0.02$	2	1.67
$x = 0.04$	4	3.77
$x = 0.1$	10	9.47

parameter with decreasing temperature (in Figure 3.1(d)) is thought to be of thermal lattice contraction. The doping concentration of Gd have been verified from the Energy dispersive X-ray spectroscopy analysis (EDS), presented in Figure 3.2. The atomic percentage of the constituent elements have been calculated from the weight percentage and represented in table 3.1. Elemental analysis shows the homogeneity of the constituent elements over the sample and the obtained doping concentrations of Gd are in well agreement with our calculated starting Gd concentrations as presented in table 3.2.

3.2 Magnetic properties

Zero field cooled warming (ZFCW) and field cooled warming (FCW) magnetization curves of all the samples as a function of temperature, under an applied field 100 Oe, are shown in Figure 3.3. In the ZFCW and FCW curves

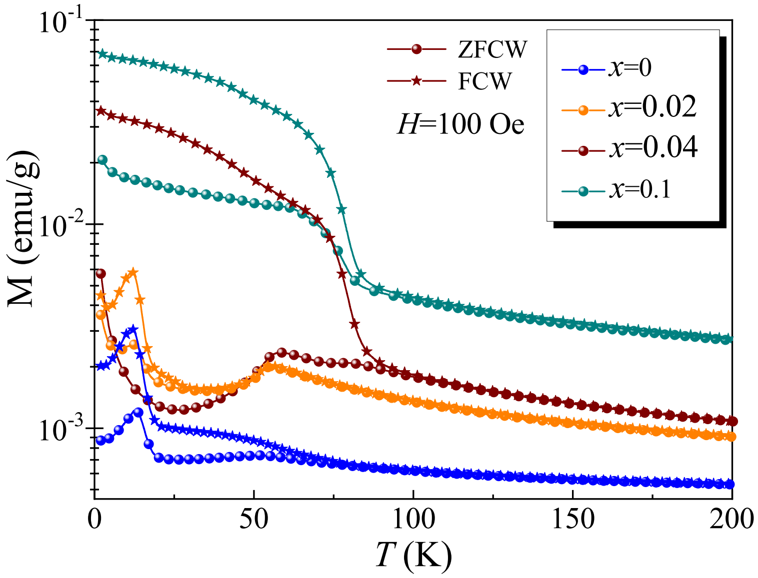

Figure 3.3: Magnetization $M(T)$ as a function of temperature for various x.

of the parent $x = 0$ compound, an FM ordering starts below 55 K and an prominent anomaly near 15 K are observed with a small bifurcation. For $x = 0.02$ compound, the magnetic ordering at the same temperature getting prominent with a notable dip around 35 K with the similar anomaly below 15 K, for both the ZFCW and FCW curves. It seems like occurring multiple magnetic transitions or a feature of partial spin-orbit compensation. For the second possibility, below the magnetic ordering temperature, the orbital counterpart of M i.e. μ_o starts to dominate the spin component μ_s, as a result the trend of M get reversed and further lowering of temperature (below 35 K), μ_s conquering again. For this, the exact FM transition temperature is inconclusive. ZFCW curve of the $x = 0.04$ compound follows the same nature of $x = 0.02$ with a dip. However, The FCW curve depicts FM like behaviour with a bifurcation from the ZFCW curve below 85 K but does not exhibit any dip in M. Because, at this x value the μ_s and μ_{cep} have such enhanced that they dominates μ_o over the whole region, cause the μ_s and μ_{cep} both align parallelly to the applied magnetic field during cooling. In case of $x = 0.1$, both the ZFCW and FCW M are showing ferromagnetic behavior with large bifurcation under 85 K with no dip. This large Gd concentration in the system increases the CEP to a certain level that the change in CEF allows the Sm/Gd spin contribution with μ_{cep} to overcome the μ_o. Hereby, the $x = 0.02$ compound has been found to be most interesting among the series and need to be studied more to reveal the suspected spin-orbit compensation behaviour in the thermo-magnetization curve. Possibility of any structural transition has been declined from temperature dependent XRD analysis, now the feasible magnetic origin need to be further investigated. It should be mentioned that, none of the susceptibility data of all the studied compound in this series has been found to follow the Curie-Weiss behavior.

Several FCW $M(T)$ curves of the $x = 0.02$ compound have been measured at various H to study the effect of it on the observed magnetic transition, as shown in Figure 3.4(a). In FCW protocol the samples are initially cooled under H and $M(T)$ is measured in subsequent warming under the same cooling H. No shift in the magnetic ordering transition has been observed, even at high field but the dip is getting profound with higher H and the minima is observed at 35 K. One more engrossing phenomenon has been perceived that the pronounced anomaly below 15 K has been faded out with increasing magnetic field, and above 1 kOe it has been completely disappeared. Figure 3.4(b)-(c) display the temperature variations of the in phase ($\chi'(T,\omega)$) and out of phase ($\chi''(T,\omega)$) component of the ac magnetic susceptibility (χ_{ac}),

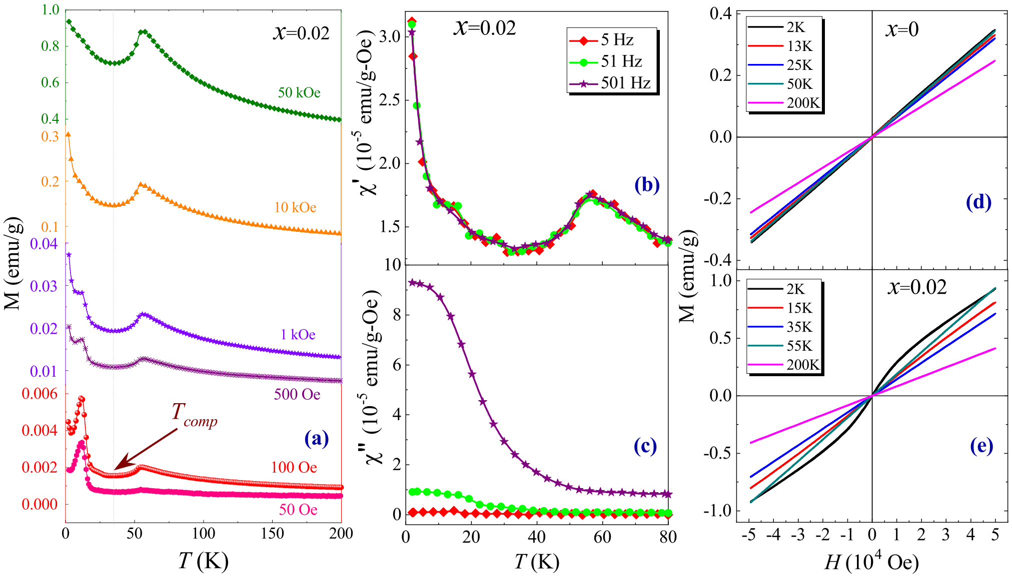

Figure 3.4: (a) FCW magnetization curves under different applied H. (b) Real (χ') and (c) imaginary (χ'') component of ac magnetic susceptibility (χ_{ac}) at various frequencies of the x=0.02 compound. (d−e) ZFC $M(H)$ at several temperature for the parent ($x = 0$) and $x = 0.02$ compound.

measured in the region of interest from 2 K to 80 K for the frequency ($\omega/2\pi$) range 5 Hz to 551 Hz. During the χ_{ac} measurement the ac magnetic field H_{ac} set at 5 Oe while the dc magnetic field H_{dc} kept at zero. It is clear from the $\chi'(T, \omega)$ curve, that the detected strong peak near 55 K is highly frequency independent, which indicates a magnetic ordering associated with the FM-PM (paramagnetic) transition. Zero field cooled (ZFC) M-H curves at different temperatures of the parent compound and $x = 0.02$ compound are presented in Figure 3.4(d) and (e), respectively. For both the samples no saturation tendency in M has been observed upto 50 kOe even at low temperatures. For the $x = 0.02$ compound at 2 K, initially M increases with H, then varies almost linearly in a comparatively slow manner at higher fields. At other temperatures the isothermal $M(H)$ varies linearly with H for both the compounds, the linear nature of $M(H)$ curves are associated to the pseudo ferrimagnentic spin structures of the compounds. No pronounced hysteresis leads to the presence of very minimal magnetocrystalline anisotropy.

3.3 Heat capacity

The temperature dependent heat capacity $C(T)$ of the two samples $x = 0$, 0.02 are measured in the temperature range 2.1−100 K during warming under zero and 50 kOe magnetic field, presented in Figure 3.5(a−b). The zero field $C(T)$ curves exhibit only single peak around 50 K and 51 K for the $x = 0$ and 0.02 compounds respectively, indicating the FM to PM transition. No significant anomaly has been observed in the region corresponding to the suspected multiple magnetic transitions. Therefore, we confirm that the appeared M reversal and the dip at 35 K evidences the partial spin-orbit magnetic compensation. We fitted the low temperature (4−10 K) region of $C(T)$ data using the formula $C(T) = \gamma T + \beta T^3$, where the first and second terms correspond to the electronic and lattice contributions to C. Fitted data are represented in terms of C/T vs. T^2 in the insets of Figure 3.5 (a-b). A negligible Schottky contribution has been observed below 4 K, this has not been taken into account due to lack of data points and the region has been excluded during fitting. A large increment in the electronic contribution term (γ) has been found for the $x = 0.02$ compound from the parent, which can be attributed to the enhancement of CEP upon Gd doping in the system. No prominent deviation of the peak in the $C(T)$ data has been noticed between the $H = 0$, 50 kOe data of the $x = 0.02$ compound. Though an increment

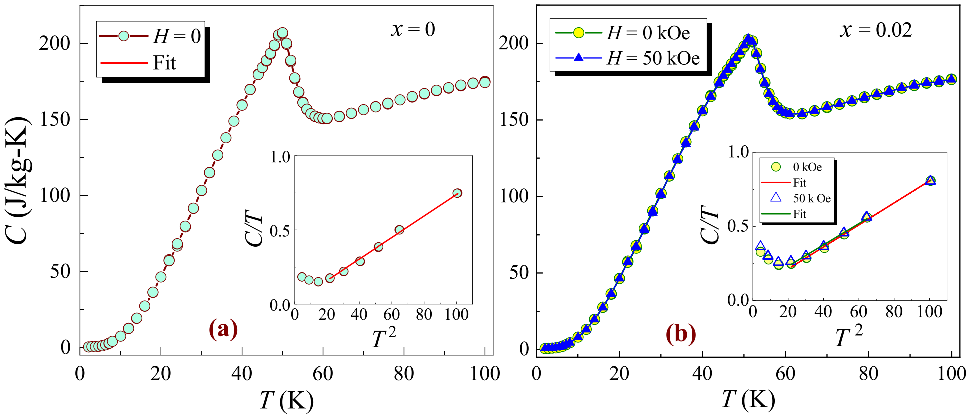

Figure 3.5: (a) Zero field specific heat ($C(T)$) as a function of temperature for $x = 0$ compound. (b) Zero field and with field ($H = 50$ kOe) $C(T)$ data for the $x = 0.02$ compound. Insets show the C/T vs. T^2 data with fitting.

Table 3.3: The parameters are obtained from the fitting of $C(T)$ data

x	γ (mJ/mol-K^2)	β (mJ/mol-K^4)
0	14.2 ± 0.87	7.25 ± 0.21
0.02 (0 kOe)	64.7 ± 1.71	7.42 ± 0.12
0.02 (50 kOe)	89.0 ± 0.61	7.15 ± 0.10

in γ has been observed for $H = 50$ kOe, indicating the increase of density of states (DOS) with field, which is usual for metallic systems.

3.4 Transport properties

The exact magnetic state in the partial compensation region, subject to further analyze by zero field and with field ($H = 50$ kOe) electrical resistivity ($\rho(T)$) measurements (in Figure 3.6(a)). The $\rho(T)$ data of $x = 0$ and 0.02 compounds show a slope change near their ordering temperatures, above which its exhibit purely metallic nature. No extra anomaly has been seen anywhere, even at T_{comp}, revealing the materials are in magnetically ordered

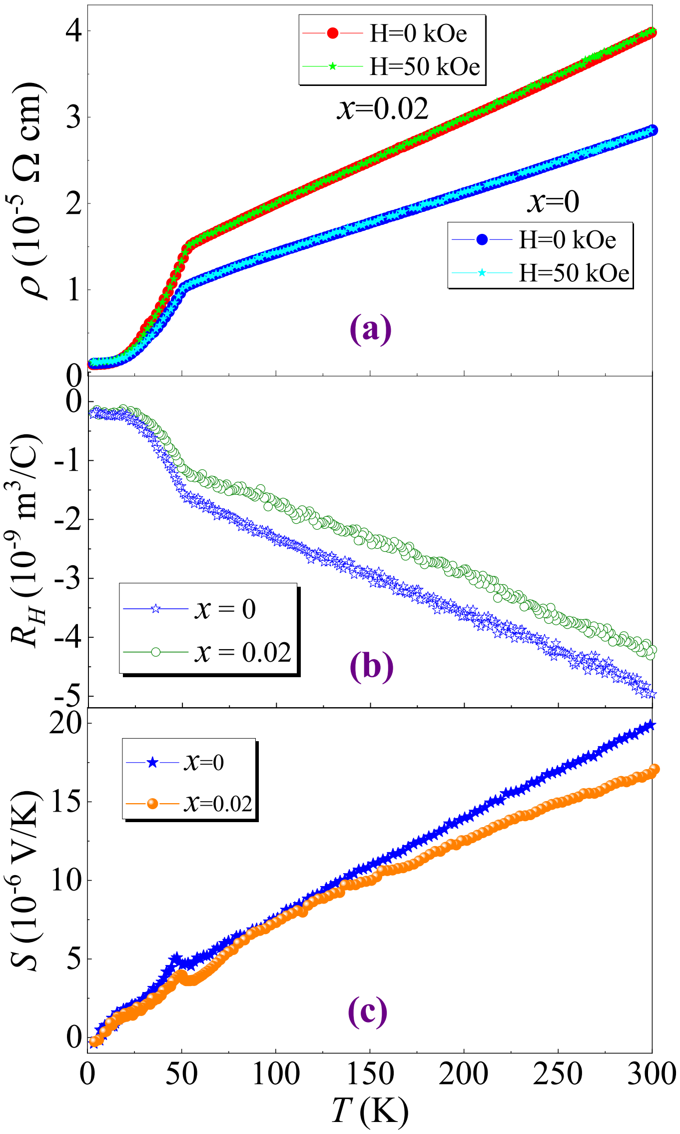

Figure 3.6: (a) Zero field and with field (H = 50 kOe) resistivity ($\rho(T)$), (b) Hall coefficient $R(H)$ as a function temperature and (c) temperature variation of Seebeck coefficient (S) of the $x = 0$, 0.02 compounds.

state at T_{comp}. No prominent deviation has been observed in the 50 kOe $\rho(T)$ curves even at their ordering temperatures or at T_{comp}. Furthermore, the Hall coefficient (R_H) as a function of temperature has been studied under 90 kOe applied magnetic field, as shown in Figure 3.6(b). Only a deviation from the linear nature is observed below the ordering temperature, no other change in the type of charge carrier has been found in the compensation region. In Figure 3.6(c), the Seebeck coefficient S(T) as a function of temperature for both the compounds show the respective FM transition temperatures in terms the change of the electronic scattering during the FM ordering. For better understanding of the partial spin-orbit magnetic compensation phenomena, we have to reveal the proper spin indication. Some sellective techniques such as, magnetic Compton scattering experiment and X-ray magnetic circular dichroism (XMCD) could be the appropriate, cause it can directly measure the magnitude of μ_s. Although, the samples carry a small value of net M in the compensation region, so by changing the external magnetic field direction we can reverse the spin arrangements, and it would help us to extract the exact spin informations.

3.5 Discussions

From the above experimental results, we have found that for $x = 0.02$ compound, the system enters to ferromagnetic state at $T_C = 51$ K and goes through a smooth minimum near $T_{comp} = 35$ K, followed by an another anomaly below 15 K, which is possibly due to the freezing of spin at low temperatures. Specific heat data do not indicate any additional sign of magnetic transition apart from that at T_C. Resistivity and AC susceptibility data also agree with the heat capacity. This implies that the system remains essentially in the ferromagnetic state through T_{comp} down to the lowest measured temperature. The dip in the thermomagnetic curve is therefore the indication of magnetic compensation at T_{comp}, where the μ_o and μ_s are presumably equal and opposite, and thus the total M is just the moment due to the polarized conduction electron. It has been well established through experiment as well as theory that the conduction electron moments (μ_{cep}) align along the same direction as the spin moments of Sm^{3+} ions. Hence, it enhances the total spin part of the magnetic moment. As the cooling field increases the overall $M(T)$ curves shift upward as the μ_{cep} is proportional to the applied field. The shape of the $M(T)$ curves remain almost unaltered with the cooling field, except the anomaly at low temperature, which gradually wash out with field. Like other Sm alloys, the μ_s takes over μ_o above T_{comp} and it is just opposite below T_{comp}. However, it is of interest to note that total M never attains negative unlike (Sm,Gd)Al_2 compound, in which $M(T)$ curves measured at low fields have crossover to the negative M axis. This negative magnetization in (Sm,Gd)Al_2 system is attributed to the continuous decrease of M as μ_o (aligns opposite to the field direction) grows continuously with lowering of temperature and it overpower μ_s below T_{comp}. However, the cooling field greater than 20 kOe is required to overcome the strong magnetocrystalline anisotropy energy (MCAE) and realigned the magnetization along the field direction; results a dip in the $M(T)$ curve instead of a crossover near T_{comp}. On the contrary, negligible coercive field in $M(H)$ isotherm suggests very weak magnetocrystalline anisotropy (MCA) in the present system. Obviously, a low cooling field (~ 50 Oe) can even overcome the MCAE and realign the magnetization along the field direction, Which makes absence of any diamagnetic effect below T_{comp} in the studied systems. As can be seen for the higher Gd concentrations ($x \geq 0.04$) $M(T)$ curves show typical ferromagnetic nature. This implies the sum of μ_s^{Sm}, μ_s^{Gd} and μ_{cep} contributions exceed the Sm orbital moment throughout the temperature range.

3.6 Conclusions

Temperature dependencies of magnetization, AC susceptibility, heat capacity and transport behavior reveal the exotic thermomagnetic behavior in Gd doped SmAg system. There is a prominent minimum in the $M(T)$ curve inside the ferromagnetic ordered state for $x = 0.02$ compound. This feature can be well explained in terms of the different temperature dependencies of antiparallelly coupled spin and orbital moments of the Sm^{3+} ions. Conduction electron contribution and the pure spin moments of the Gd^{3+} ions found to strengthen the total spin moment of the system. Magnetocrystalline anisotropy also plays an important role in deciding the nature of the thermomagnetic curve in the present system.

Chapter 4

Role of Cr in magnetic properties of $\mathrm{ErRu}_{2-x}\mathrm{Cr}_x\mathrm{Si}_2$

In this chapter, the observations in the magnetic and magnetocaloric properties upon Cr dopping (for $x = 0$, 0.15, 0.3, 0.5) in $\mathrm{ErRu}_{2-x}\mathrm{Cr}_x\mathrm{Si}_2$ are presented [105]. Existing antiferromagnetic (AFM) interaction becomes weak when a small amount of Cr is replaced in place of Ru, resulting in magnetic transition from AFM to doping induced ferromagnetic (FM) transition. The associated change in transition (AFM to FM) is coupled with the inter atomic distance along c axis. Above certain concentration, the nature of the transition is also modified to second order from first order.

4.1 Structural analysis

The room temperature (RT) powder XRD patterns of the annealed samples (800°C for 170 h) with rietveld refinement are presented in Figure 4.1(a-d),

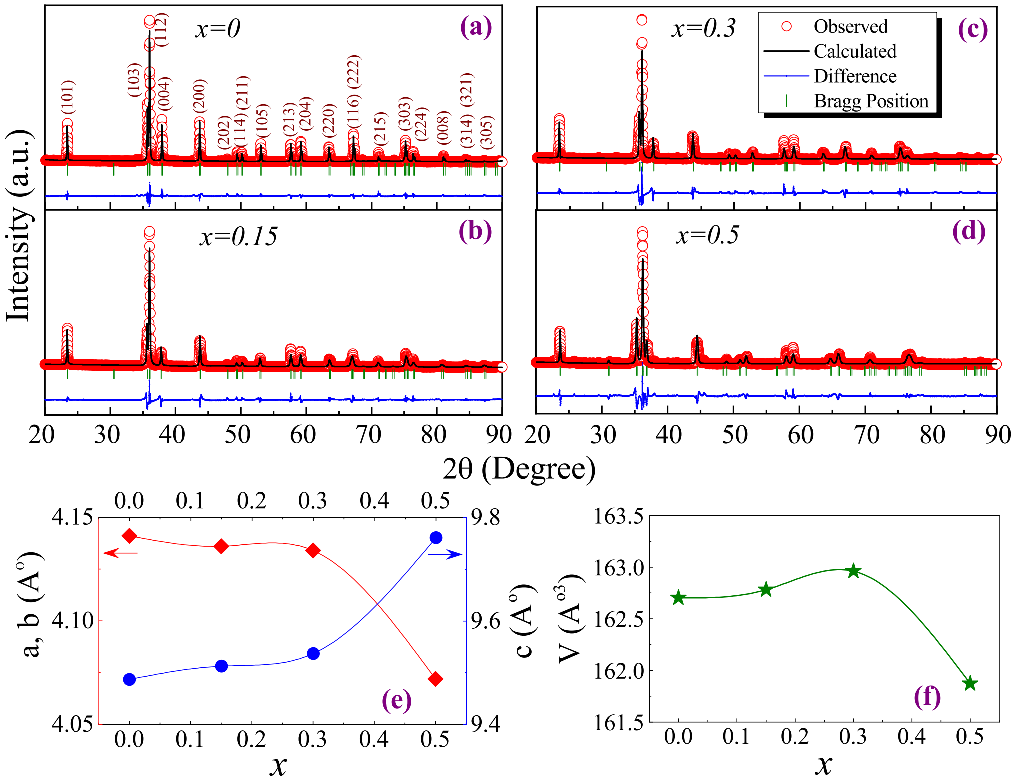

Figure 4.1: (a–d) Room temperature XRD pattern of $ErRu_{2-x}Cr_xSi_2$ ($x = 0 - 0.5$), with rietveld refinement, χ^2 values are in between 15–17. (e–f) The variation of the lattice parameters and unit cell volume with x, obtained from the fitting.

confirm that all the samples are in single phase except some minor unreacted Er impurity phases < 2 %. The crystal structures are found to be $ThCr_2Si_2$ type (space group I4/mmm) body centered tetragonal (BCT). Figure 4.1(e-f) show the variation of lattice parameter and cell volume, obtained from rietveld refinement. With increase of Cr concentration (x) in the system, lattice parameter a decreases where as c increases and a slight variation ($\approx$ 0.6 %) has been observed in the cell volume (v). We have already described previously (in introduction) that the structures of RT_2X_2 compounds are composed of a sequences of parallel planes (constituting identical atoms) along tetragonal c axis, and the present magnetic interactions (FM or AFM) in those systems are strongly coupled with the interlayer R-R/T-T distances [82, 83]. Hereby, with increasing x, increment in c anticipates to amend the existing magnetic properties.

4.2 Magnetic properties

The temperature variation of magnetization data of the $\mathrm{ErRu_{2-x}Cr_xSi_2}$ ($x =$ 0, 0.15, 0.3, 0.5) compounds have been collected in 500 Oe magnetic field under ZFCW and FCW conditions. No prominent differences has been observed in the corresponding ZFCW and FCW magnetic susceptibility ($\chi(T)$) curves of any of the samples, therefore to avoid complications only ZFCW $\chi(T)$ data are represented in Figure 4.2(a). It exhibits that the parent compound ($x = 0$) undergoes an AFM transition at its Néel temperature ($T_N =$) 6 K. However, introducing Cr in the system, for $x = 0.15$ compound the existing AFM transition seems to be occurred below 6 K. Thereafter, beyond $x =$ 0.15, no AFM transition is clearly evident down to 3 K, whereas, an abrupt enhancement in $\chi(T)$ is observed at low temperature in the curve of $x = 0.3$ compound. This signifies a weak ferromagnetic (FM) correlation has been developed due to Cr doping, which helps to induce additional magnetic moments in the systems. With further increase of Cr, $x = 0.5$ compound exhibits that the weakly developed FM phase has been stabilized at low temperature. Surprisingly, the observed $\chi(T)$ behavior of the $\mathrm{ErRu_{2-x}Cr_xSi_2}$ ($x = 0{-}0.5$) compounds have been found very similar to the magnetic field dependent nature in the $\chi(T)$ of parent $\mathrm{ErRu_2Si_2}$ compound, reported by T. Samanta

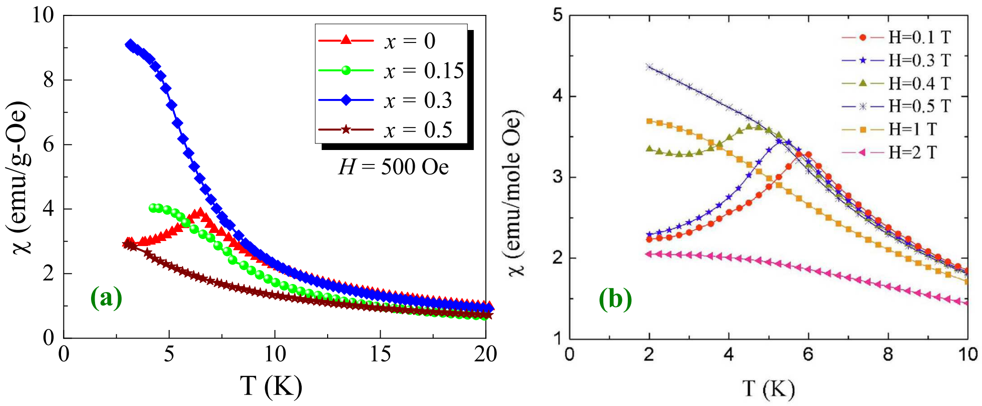

Figure 4.2: (a) The temperature dependency of dc magnetic susceptibility ($\chi(T)$) of ErRu$_{2-x}$Cr$_x$Si$_2$ ($x = 0 - 0.5$) using ZFCW protocol with 500 Oe measuring field. (b) ZFC $\chi(T)$ of the parent ErRu$_2$Si$_2$, for different applied magnetic fields (picture taken from Ref. [90].)

et al. [90] and their data has been represented in Figure 4.2(b) for resemblance. They have observed that the AFM transition temperature (T_N) for ErRu$_2$Si$_2$ is around 5.5 K for 1 kOe magnetic field. With increase in measuring field, T_N is reducing and above a certain magnetic field of 4 kOe no AFM transition was observed down to 2 K i.e. the existing AFM phase has been modified to field induced FM state. Therefore, we would like to anticipate that the Cr doping and application of magnetic field has the similar effect on the magnetism of ErRu$_2$Si$_2$ compound. In the exchange Hamiltonian, which measures the magnetic ordering, increase in the inter-layer R-R/T-T distances or magnetic field are providing same effect, as we have observed for both the cases that the existing AFM ordering is supressed by newly developed FM ordering.

Inverse susceptibility ($1/\chi(T)$) curves with Curie-Weiss fitting in the temperature regime 80−150 K using the Curie-Weiss formula: $\chi = C/(T - \theta_P)$, are presented in Figure 4.3, where θ_P is the paramagnetic Curie temperature

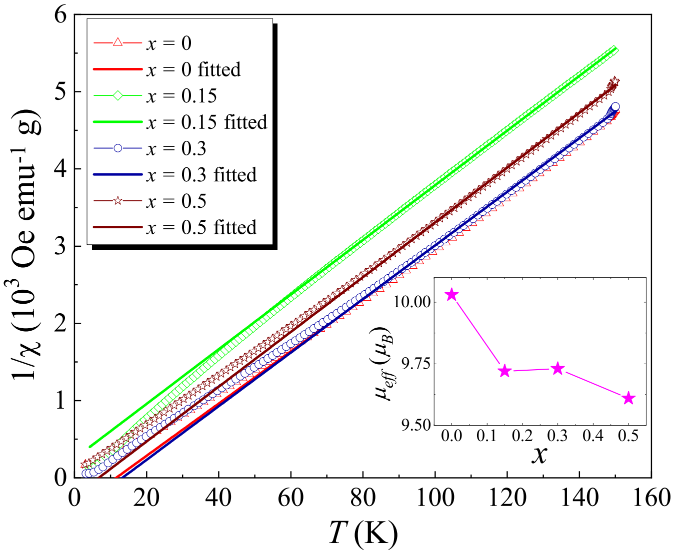

Figure 4.3: Temperature variation of inverse susceptibility ($1/\chi(T)$), fitted with Curie-Weiss law in the high temperature region; inset shows the change of experimental μ_{eff} with increasing x .

and C is the Curie-Weiss constant. The calculated effective paramagnetic moment (μ_{eff}) per Er^{3+} ion has comes out to be 10.03 μ_B, 9.72 μ_B, 9.73 μ_B and 9.61 μ_B for $x = 0$, 0.15, 0.3 and 0.5 samples, respectively. Experimental μ_{eff}/Er^{3+} values are observed to be little higher than its theoretical free ion value (9.59 μ_B/Er^{3+}), for all the samples. This indicates that both Ru and Cr has their magnetic contributions to the net magnetization of $ErRu_{2-x}Cr_xSi_2$ system, apart from the main contributor Er. It should be noted down that the Cr^{3+} (3.87 μ_B) has lower free ion μ_{eff} than the Ru^{3+} (5.92 μ_B), therefore the observed reduction of μ_{eff} with increasing Cr concentration in the system in expense of Ru is attributed, as shown in the inset of Figure 4.3.

As evident from the previous study, the parent compound possesses an FOMT around $T = 6$ K. For further analysis, to see whether there is any change in the order of the magnetic transitions due to doping of Cr, we have

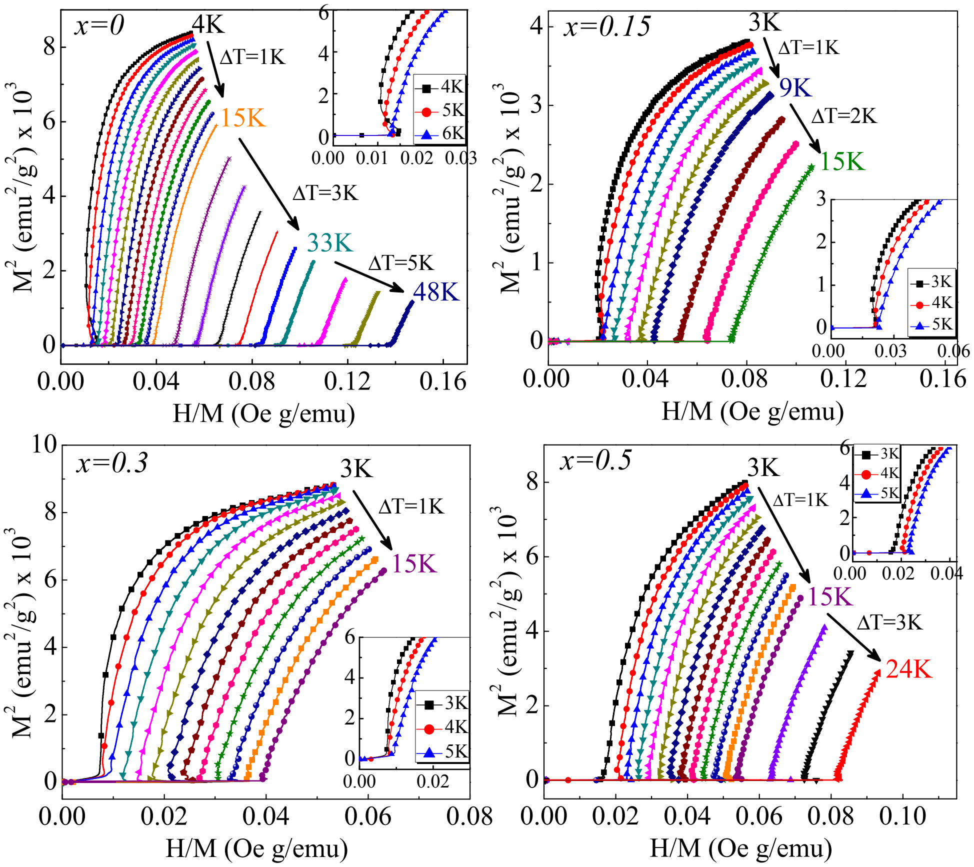

Figure 4.4: Arrot plots (M^2 vs H/M plot), indicating the change in transition nature with increasing x; insets are showing the low temperature zoomed data.

measured isothermal ZFC $M(H)$ curves at various temperatures below and above of the transition region of each compound, and construct the Arrot plot (M^2 vs. H/M plot), as shown in Figure 4.4. It is well accepted from the Banerjee criteria that any negative slope of the H/M versus M^2 plot corresponds to an FOMT, in contrast of a positive slope relies to occur a second order magnetic transition (SOMT) in the system. Therefore, as we can observe in the insets of Figure 4.4, negative slopes at low temperature for $x = 0$ and 0.15 samples confirm the presence of FOMT. Though, in case of $x = 0.15$ a little deviation from FOMT has been identified. Whereas, with further Cr doping, for $x = 0.3$, 0.5 samples, the FOMT completely disappeared. Hence one would anticipate that above a critical concentration of Cr doping in $\mathrm{ErRu}_{2-x}\mathrm{Cr}_x\mathrm{Si}_2$ system expands the T-T/R-R distances along the c axis to a critical value, beyond which the magnetic transitions are no longer behaves as FOMT. Due to the same, the observed AFM nature in the parent member is promoted to weak FM in the doped compounds of the series. Our explanations about the observed change in nature and order of magnetic transition are based on magnetic measurements only, which only account the moments in macroscopic scale.

4.3 Magnetocaloric properties

To study the effect of Cr doping on the MCE properties, magnetic entropy change ($-\Delta S_M$) of these compounds have been obtained form our already measured isothermal $M(H)$ curves. The temperature variation of $-\Delta S_M$ curves upto 20 K of all the samples for magnetic filed change (ΔH) of 50 kOe

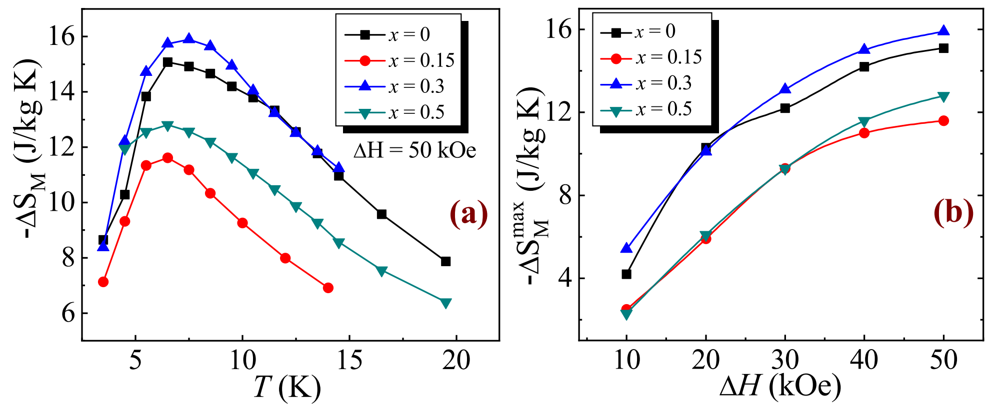

Figure 4.5: (a) The temperature dependence of magnetic entropy change ($-\Delta S_M$) for the field change of 50 kOe, (b) variation of $-\Delta S_M^{max}$ with increasing field change (ΔH) for various x.

are shown in Figure 4.5(a). It should be noted that for certain Cr concentration x = 0.3, the $-\Delta S_M$ value increases and remains consistently higher than the other compositions for all the ΔH, as depicted in Figure 4.5(b). The maximum value of $-\Delta S_M$ ($-\Delta S_M^{max}$) = 15.9 J/kg-K is achieved for x = 0.3 sample around 6 K, which is slightly better than its parent compound $ErRu_2Si_2$ (15.1 J/kg-K), for the field change of 50 kOe. It is ought to be mentioned that this observation is consistent with the $\chi(T)$ curve for x = 0.3 compound (Figure 4.2(a)), where a rapid increase in $\chi(T)$ was observed. Furthermore, if we observe the $-\Delta S_M^{max}$ values of all the samples for ΔH = 50 kOe, for x = 0.15 the obtained value is less than the parent compound. Engraining a small percentage of FM doping (Cr) in an AFM compound may create disorder or canted AFM like structure, which causes the decrease in AFM transition temperature and the overall $-\Delta S_M$. To measure the corresponding relative cooling power (RCP), the full width half maximum (δT_{FWHM}) of the -$\Delta S_M(T)$ curve for ΔH = 50 kOe of x = 0.3 sample, has been found as 16 K. Therefore, the RCP value has been estimated to 254 J/kg, which is quite good with respect to the same for reported SOMT materials having transitions in low temperature (detail example of SOMT compounds are in next chapter). Our MCE study reveals that among the various doped member, $x = 0.3$ compound i.e. $ErRu_{1.7}Cr_{0.3}Si_2$ delivers comparable $-\Delta S_M^{max}$ value with some of the MCE materials, such as $ErRCr_2Si_2$, $HoMn_2Si_2$, $PrFe_2Si_2$, $NdFe_2Si_2$ [142–144] etc. in the similar transition temperature region. Therefore, it could be a potential compound for using in magnetic refrigeration for hydrogen, helium liquification and other purposes.

4.4 Chapter summary

In this chapter, the effect of Cr doping in magnetic and magnetocaloric properties of $ErRu_{2-x}Cr_xSi_2$ system have been discussed. One of the most important observation is, with increasing Cr concentration (x) in the system, $\chi(T)$ mimics the field dependent magnetic susceptibility behaviour of the parent $ErRu_2Si_2$ compound. From the structural analysis (from XRD data) we have evidenced that the doping of Cr modifies the c/a ratio, which affects the exchange interaction between the magnetic ions and induces weak FM correlation in the system, and justifies the mimicking of $\chi(T)$ behaviour. Arrot plot of all the samples anticipates that above certain critical concentration of Cr the transitions are no longer FOMT, tending to SOMT. Therefore, Cr not only modifying the existing magnetic interactions (AFM to FM) but also the order of magnetic transition. Additionally, our findings also reveal the obtained magnetocaloric value $-\Delta S_M^{max} = 15.9$ J/kg-K for $\Delta H = 50$ kOe in $x = 0.3$ compound is slightly higher than the parent one, and the corresponding RCP value has been achieved to 254 J/kg, which can be useful for practical applications.

Chapter 5

Study of magnetic and magnetocaloric properties in Er_3Pd_2 compound

In this chapter, the magnetic properties and the magnetocaloric effect of a binary intermetallic compound Er_3Pd_2 are discussed from magnetization and heat capacity measurements. It usually exhibits a paramagnetic (PM) to antiferromagnetic (AFM) transition at its Néel temperature ($T_N =$) 10 K with no obvious thermal or magnetic hysteresis loss. A large reversible MCE have been observed, which is related to a second order magnetic transition from PM to AFM state.

5.1 Structural analysis

The room temperature (RT) powder XRD pattern of the annealed Er_3Pd_2 sample (800°C for 175 h) have been shown in Figure 5.1. It is evident from Rietveld refinement of the XRD spectra using Full-prof software that all the

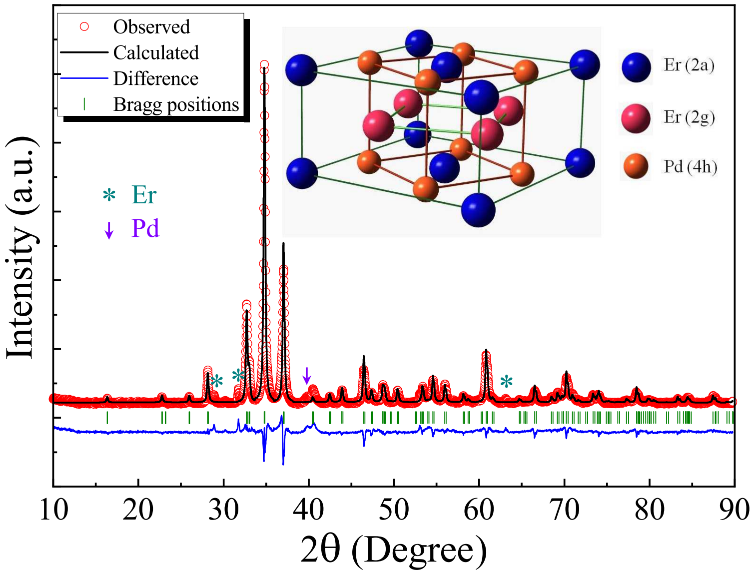

Figure 5.1: Room temperature XRD pattern of Er_3Pd_2 with Rietveld refinement, χ^2 value is 4.7. Asterisks and arrows indicate the unreacted Er and Pd impurity phases respectively. The unit cell structure, displaying 2a and 4 h Wyckoff sites are occupied by Er and 4 g are occupied by Pd atoms.

peaks can be indexed with U_3Si_2 type tetragonal structure of space group P4/mbm. Few unreacted Er (6.6 %) and Pd (5.1 %) tiny peaks have been identified in the samples even after annealing. Such impurity phases might be reduced by optimizing the annealing procedure and stoichiometry ratio of the starting materials. From refinement analysis, the evaluated lattice parameters are $a = b = 7.678$ Å, $c = 3.908$ Å. As shown in the inset of Figure 5.1, in an Er_3Pd_2 unit cell, Er atoms seat in 2a and 4 h Wyckoff sites, whereas the 4 g sites are occupied by Pd atoms.

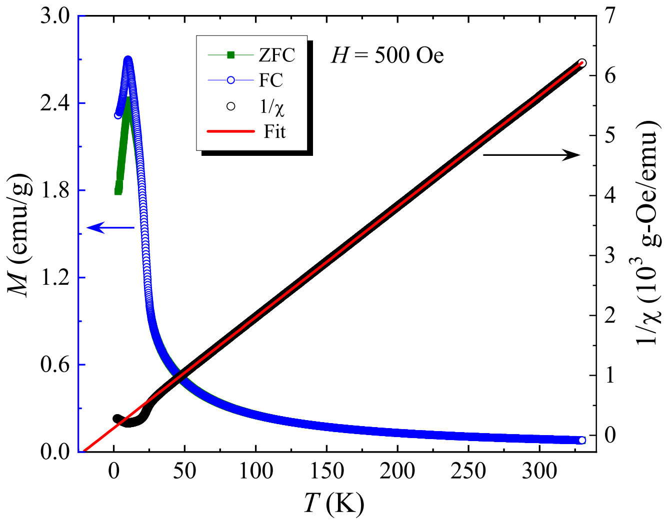

Figure 5.2: Temperature dependency of $M(T)$ under ZFCW and FCW measuring protocols at 500 Oe magnetic field (left axis). Temperature variation of the inverse dc susceptibility ($1/\chi(T)$) fitted to the CurieWeiss law (right axis).

5.2 Magnetic properties

Temperature dependent magnetization ($M(T)$) curves using different modes of measurement, ZFCW and FCW, under an applied field $(H) = 500$ Oe are plotted in Figure 5.2. An AFM to PM transition is clearly evident during warming at Néel temperature ($T_N =$) 10 K. No prominent thermal hysteresis between the cooling (FCC) and warming (FCW) data has been observed around T_N, this screened the transition to be possibly second order, and forgoing complexity only the FCW data have been provided here. In the PM region the corresponding inverse susceptibility data ($1/\chi(T)$) follows the Curie-Weiss behaviour and the Curie-Weiss fitted experimental data is shown in Figure 5.2 and indexed to the right axis. From the fitting, the obtained paramagnetic Curie temperature (θ_p) is -6 K, the negative sign of

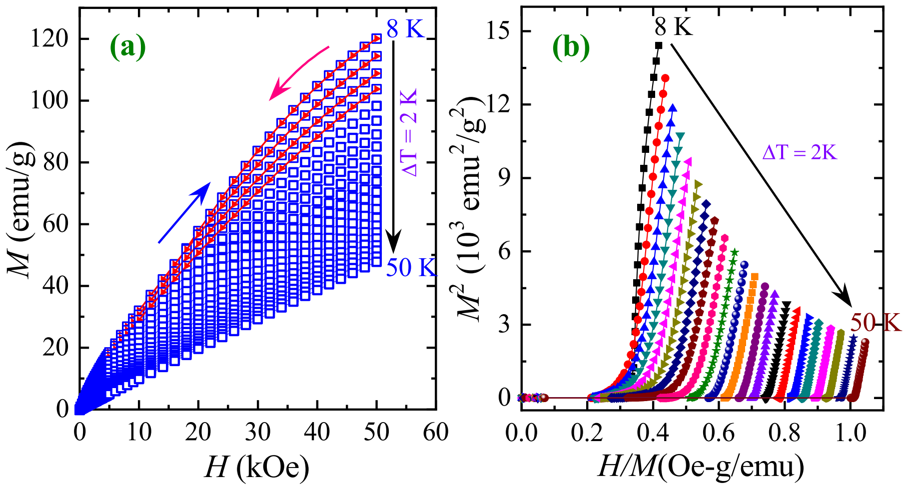

Figure 5.3: (a) $M(H)$ isotherms upto 50 kOe at various temperatures and (b) Arrott plots (M^2 vs. H/M plots), in the temperature range 8 K to 50 K.

θ_p reveals that the present magnetic interacion in Er_3Pd_2 material is AFM. Further, we have calculated the effective paramagnetic moment (μ_{eff}) per Er^{3+} ion, has been obtained as 10.16 μ_B which is notably higher than the free ion value of Er^{3+} (9.59 μ_B). This indicates that Pd^{2+} ions also have some magnetic contribution, apart from the main contributor Er^{3+} in the net magnetization of the Er_3Pd_2 system. Therefore, our observations reveal that the rare-earth ion is not only the emerging factor for the present magnetic interactions and the corresponding magnetic properties in this compound, constituent transition metal ions also have sustainable influence on the same. Isothermal $M(H)$ curves within the temperature range 8 K to 50 K have been measured at 2 K interval upto 50 kOe magnetic field, as shown in Figure 5.3(a). Near T_N $M(H)$ data are recorded in both way, with increasing and decreasing H; no notable hysteresis have been observed between them. Therefore, above 14 K $M(H)$ isotherms have been taken only for increasing

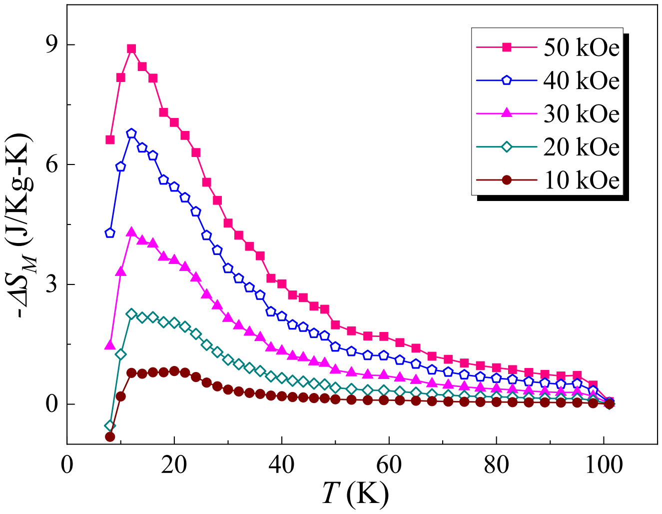

Figure 5.4: Temperature dependent magnetic entropy change (-ΔS_M) for different magnetic field variations up to 50 kOe.

H. Measuring field directions are marked with arrow using the same colour of the corresponding data points. In order to reveal the nature of the undergoing AFM transition, we have constructed the Arott plot (M^2 vs. H/M graph) from the previously measured isothermal $M(H)$ curves. In Arott plot, as in Figure 5.3(b), at transition region no inflection or negative slope have been observed, this corresponds to a pure SOMT. Hence our priliminary assessment about the nature of the undergoing transition from $M(T)$ data, consisting no temperature hysteresis behaviour, has been affirmed as SOMT.

5.3 Magnetocaloric properties

As the material Er_3Pd_2 confirms SOMT around 10 K with no thermal and magnetic field hysteresis, it attracts our attention for MCE study. Consequently, the magnetic entropy change (-ΔS_M) has been calculated from the previously measured $M(H)$ isotherms using Maxwell's relation [145]. The temperature dependence of obtained -ΔS_M curves for various magnetic field changes up to 50 kOe are represented in Figure 5.4. The maximum -ΔS_M value (-ΔS_M^{max}) has been acheived to 8.9 J/kg-K at 12 K for a field change of 50 kOe. Though this appreciated -ΔS_M^{max} value is inadequate in contrast to the widely studied FOMT materials [90, 99–105], however comparable with several SOMT compound, such as $PrCo_2B_2$, $GdPd_2Si$, PrNi, $(Ho, Tb, Dy)_2In$ etc. [146–151].

5.4 Heat capacity

Heat capacity ($C(T)$) measurement is one of the best tool to confirm the exact transition temperature. The temperature variation of $C(T)$ of Er_3Pd_2 under zero and 50 kOe magnetic field are shown in Figure 5.5(a). It is clearly evident that the zero field $C(T)$ curve displays pronounce anomoly in the form of a λ-shape peak around 10 K, indicating a typical SOMT correlated to an AFM to PM transition. Corresponding T_N has been obtained from the $C(T)$ data is 9 K, which is found consistent to the same determined from $M(T)$ measurement. A high magnetic field of 50 kOe diminishes the $C(T)$ peak height along the transition region, following the change in entropy during the phase transition due to applied magnetic field.

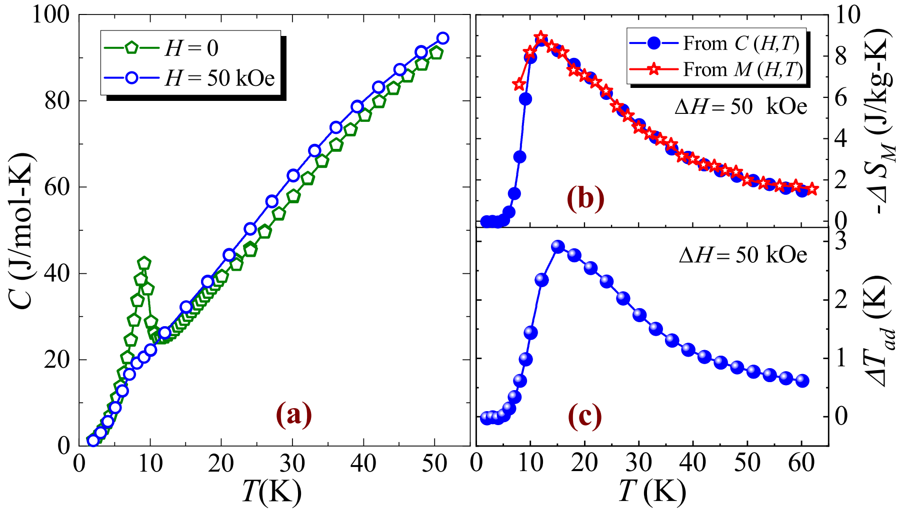

Figure 5.5: (a) Heat capacity C as a function of temperature at magnetic field 0 and 50 kOe. (b) Temperature variation of magnetic entropy change -ΔS_M, obtained from heat capacity and magnetization measurements for the field change of ΔH = 50 kOe. (c) Adiabatic temperature change, ΔT_{ad}, for the ΔH = 50 kOe.

5.5 Discussion

Using the zero field and with field $C(T, H)$ data, the change in magnetic entropy (-ΔS_M) can be estimated using equation (1.27) for the field change of (ΔH =) 50 kOe. The temperature dependence of -ΔS_M, obtained from the heat capacity data, has been plotted in Figure 5.5(b). Temperature variation of the same for field change of 50 kOe, received from the magnetization measurements, has been provided in the same figure. It is evident that the both -$\Delta S_M(T)$ graphs, obtained from the magnetization and heat capacity measurements, are almost similar over the measured temperature regime. The temperature variation of calculated ΔT_{ad} for ΔH = 50 kOe, using equation (1.28) are presented in Figure 5.5(c). It should be noted that the temperature variation of -ΔS_M and ΔT_{ad} graphs have shown almost similar nature, except a slight temperature shift of the peak positions. Hereby the maximum value of -ΔS_M (-ΔS_M^{max}) and ΔT_{ad} (ΔT_{ad}^{max}) value for ΔH = 50 kOe have been achieved as 8.9 J/kg-K and 2.9 K, respectively. To estimate the RCP value, full width half maximum (δT_{FWHM}) of the -$\Delta S_M(T)$ curve for ΔH = 50 kOe, has been found as 22.8 K. Corresponding RCP value has been reached to 201 J/kg. For our studied Er_3Pd_2 compound, the obtained value of RCP, and -ΔS_M^{max}, ΔT_{ad}^{max} are reliable with compared to some of the MCE materials undergoing SOMT in the similar temperature region [111,152–155].

5.6 Chapter summary

In this chapter, the priliminary observation is that the Er_3Pd_2 compound undergoes paramagnetic to antiferromagnetic transition at ($T_N =$) 10 K on cooling, and does not exhibit any thermal or magnetic hysteresis around T_N. T_N has been also evidenced from the heat capacity measurement, with zero and 50 kOe magnetic field. The second order nature of the transition is also verified from the Arott plots. -$\Delta S_M(T)$ curves are obtained from both the magnetization and heat capacity data, and they are in good agreement (almost overlapped) over the measured temperature region. Therefore, one can rely on the obtained parameters. -ΔS_M^{max}, ΔT_{ad}^{max} and RCP values are estimated to be 8.9 J/kg-K and 2.9 K, 201 J/kg, respectively, for the field change of 50 kOe. Absence of any hysteresis around the transition temperature qualifies the sample to produce large and reversible MCE, for which it can be a potential compound for practical applications.

Chapter 6

Origin of magnetoresistance across the martensitic transformation in $Ni_{44}Cu_2Mn_{43}In_{11}$ Heusler alloy

In this chapter, we have revealed the possible origin of the large magnetoresistance (MR), observed across the first order martensite transformation (MT) of $Ni_{44}Cu_2Mn_{43}In_{11}$ Heusler alloy. Various phase fractions have been calculated from the resistivity data along with its dependency with temperature and magnetic field, considering the MT region as binary coexisting phase. Among them, the field induced austenite phase fraction (f_{IA}) has been found as the most significant for the large MR, compared to the other factors, i.e. the parent austenite or martensite phase fractions. The temperature dependent growth of austenite and martensite phases within the MT region are also evidenced from the temperature dependent XRD data, performed using synchrotron radiation. Phase purity analysis, structural study and magnetic properties of the sample have been reported previously [58], therefore not discussed here.

6.1 Resistivity

The temperature dependent resistivity ($\rho(T)$) curves, measured under ZFC and ZFCW protocols, are presented in Figure 6.1(a). As evident, the ZFCW $\rho(T)$ curve starts to drop rapidly at austenite start temperature (T_{as}) and continues to drop upto the austenite finish temperature (T_{af}), while the $\rho(T)$ curve of ZFC mode start to increase at martensite start temperature (T_{ms}) until the martensite finish temperature (T_{mf}). The rapid increment in $\rho(T)$ below T_{ms} may arises from the enhanced conduction electrons scattering due to development of differently oriented martensite variants along with the other significant factors e.g. presence of microcrack, modification of Brillouin zone boundary during MT etc [126, 156–159]. The differences of obtained characteristic transition temperatures in cooling and warming $\rho(T)$ curves leave a thermal hysteresis within the MT region. The ZFCW $M(T)$ curve has been represented in Figure 6.1(a) to compare the characteristic transition temperatures from magnetization data, and it is in well agreement with the same obtained from the ZFCW $\rho(T)$ curve. Now, being a disorder influenced first order phase transition, the region of thermal hysteresis is highly metastable, and both the austenite and martensite phases can coexist together. However, beyond the MT region, cooling and warming $\rho(T)$ curves follow almost same temperature dependency. Since, our primary motivation has been focused to correlate the existing different phase fractions with the

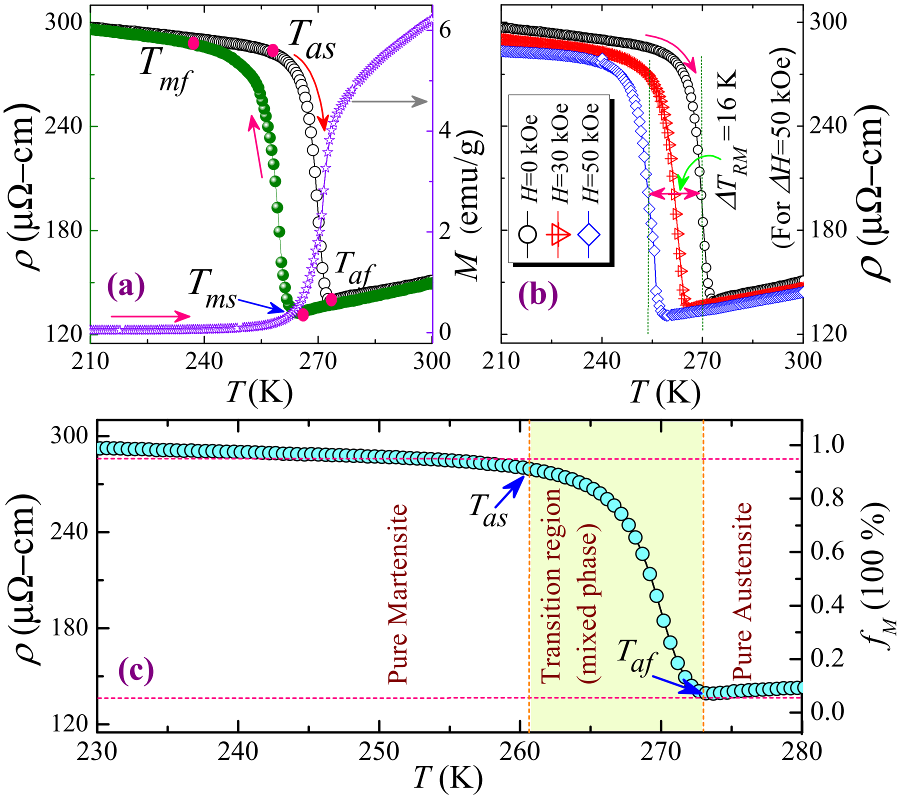

Figure 6.1: (a) The temperature dependency of $\rho(T)$ and $M(T)$ curve using ZFC and ZFCW protocol [58], (b) FCW $\rho(T)$ curves at different applied field. (c) Pink dashed line is the linear extrapolation of ZFCW $\rho(T)$ curve at T_{as} and T_{af}.

magnetoresistance ($\Delta\rho/\rho_0$) across the MT, so various $\rho(T)$ data has been further measured at different applied magnetic fields (H) using the FCW protocol (Figure 6.1(b)). It should be noted that, for the measurement of $\rho(T)$ using FCC and FCW protocols, the $\rho(T)$ is recorded in subsequent cooling and warming of the material in presence of magnetic field. Here, to avoid complexity in the analysis of different phase fractions within the MT region, we purposefully considered only $\rho(T)$ curves of FCW mode. Another important characteristic temperature, reverse martensite temperature (T_{RM}), is calculated by drawing vertical line, that divides the transition width (TW) into two nearly equal parts, is needed to explain the observed large MR behavior. It is clearly evident in Figure 6.1(b) that the application of magnetic field, the T_{RM} is being shifted towards lower temperature side. This shift in T_{RM} is a consequence of the fact that upon application of magnetic field close to T_{as} enables to transform the martensite structure to austenite, at that temperature [59, 64, 65]. Thus, an application of magnetic field close to/across the MT has a significant role in altering the phase volume fractions in isothermal condition which in turn alter the MR in these compounds. A large shift in T_{RM} (ΔT_{RM}) = 16 K has been observed for the application of 50 kOe magnetic field and this high $\Delta T_{RM}(H)$ is one of the prerequisite condition to achieve large MR across the MT for these type of compounds. Figure 6.1(c) is to guide the presence of different phases over the temperature range. Isothermal $\rho(H)$ curves at several temperatures around the MT region have been measured and presented later on.

6.2 Discussion: Phase fractions

Now to quantify the different phase fractions within the MT region, we have used the conductivity expression, proposed by Landauer [160] for two coexisting phases. If the resistivity values of the austenite (ρ_A) and martensite phases (ρ_M) are considered as constant, this equation will enable us to estimate the different phase fractions along the MT from the knowledge of conductivity (σ) at any given temperature and field, the parent equation can be written in the following refined form:

$$\sigma(T) = \frac{1}{4}[(3f_A-1)\sigma_A+(3f_M-1)\sigma_M+[((3f_A-1)\sigma_A+(3f_M-1)\sigma_M)^2+8\sigma_A\sigma_M]^{\frac{1}{2}}] \tag{6.1}$$

where $\sigma_M(T)$ and $\sigma_A(T)$ are the conductivities; $f_M(T)$ and $f_A(T)$ are the phase volume fractions, of martensite and austenite phases, respectively. One can easily estimate the $\sigma_M(T)$ and $\sigma_A(T)$ from the $\rho_M(T)$ and $\rho_A(T)$, while ρ_A and ρ_M can be determined by drawing parallel line from few Kelvin above T_{af} and few Kelvin below T_{as} respectively (as shown by the pink dashed line in Figure 6.1(c)). Further more, it is also quite straightforward to represent the total phase fraction in terms of f_M and f_A for a given temperature and field within the MT region as

$$f_M(T,H) + f_A(T,H) = 1. \tag{6.2}$$

Now substituting the value of σ_M and σ_A for a given temperature and field in equation (6.1) and then solving equation (6.1) with the help of equation (6.2), one can quantify the $f_M(T,H)$ and $f_A(T,H)$ at that temperature and field. Therefore, by solving the above two equations, the $f_M(T,H)$ curves have been generated for our studied compound around its MT region, and displayed in Figure 6.2. From the knowldge of $f_M(T,H)$ we have further quantified the $f_{IA}(T,\Delta H)$ using the following equation (6.3):

$$f_{IA}(T,\Delta H) = f_M(T,0) - f_M(T,H) \tag{6.3}$$

where f_{IA} represents the magnetic field induced austenite phase fraction

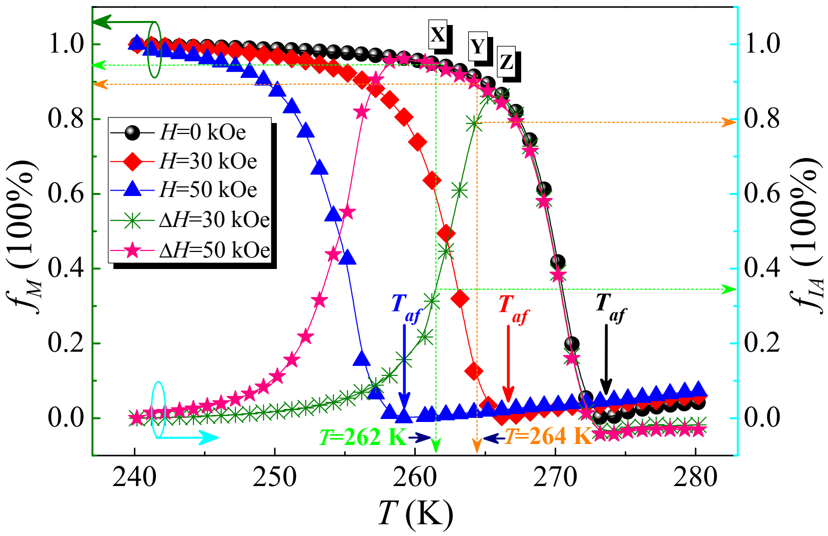

Figure 6.2: The temperature variation of f_M and f_{IA} for different applied field, $\Delta H = 30$ and 50 kOe.

when the magnetic field applied isothermally within the martensite phase, and the calculated $f_{IA}(T, H)$ curves are presented in Figure 6.2. One should note that the $f_A(T)$ always refers to the sum of $f_{IA}(T)$ and parent austenite volume fraction ($f_{PA}(T)$) in the discussion, while both f_{IA}, f_{PA} have same physical properties as f_A. It can be observed that $f_{IA}(T, \Delta H)$ attain maximum at their respective T_{af} of $f_M(T, H)$ curve and thereafter (i.e. above T_{af}) f_{IA} follows the same path as $f_M(T, 0)$ curve. Before we get into the detail behaviour of $f_{IA}(T, \Delta H)$ it is convenient to split the whole temperature region of interest into three subparts: **(i)** $T < T_{as}$ **(ii)** $T_{as} \leq T \leq T_{af}$ **(iii)** $T > T_{af}$. It is well established from the plot of Landau free energy expression for the first order transition and already evident from the plot of $f_M(T, H)$, that the martensite and austenite phases are stable in the region **(i)** and **(iii)**, respectively. Whereas in the region **(ii)**, both the phases coexist together in a metastable state [124]. Let first consider a temperature point in the region **(i)**, say $T = 240$ K, i.e. when the system is in deep martensite phase, the stability of martensite phase is high and consequently the application of a large magnetic field of 30 kOe is even insufficient to convert any martensite into austenite, and therefore the f_{IA} become zero in this temperature regime. On the other hand, with increasing temperature, the martensite component looses its stability and the application of same field is now just sufficient to convert some martensite into austenite, and hence f_{IA} starts to increase. When the system just enters into the region **(ii)**, at a temperature point say **X** ($T = 262$ K) on the $f_M(T, 0)$ curve has 95% martensite phase (i.e. $f_M = 95\%$, follow the horizontal green dash line towards the f_M axis) and remaining 5% is metastable austenite phase. Since, the martensite instability increases in this region than that for in the region **(i)**, thus an application of same field (30 kOe) converts 35% of martensite into austenite ($f_{IA} = 35\%$, follow the horizontal green dash line towards the f_{IA} axis) with remaining $f_M = 60\%$ unchanged and f_{IA} starts to increase rapidly with the progress of temperature. While the application of 50 kOe field converts all the available martensite to austenite at this temperature (at point **X**). Now moving onto another temperature point **Y** ($T = 264$ K) within the region **(ii)** contains less volume fraction of martensite $[(f_M)_Y < (f_M)_X]$ but due to the increased instability of martensite phase, the same 30 kOe field produces 79% induced austenite ($f_{IA} = 79\%$) from available 90% martensite while remaining $f_M = 11\%$ unchanged. Interestingly all the available metastable martensite is converted to the austenite by application of 30 kOe field at the point **Z** ($T = 265$ K) and f_{IA} reaches maximum ($f_{IA} = 85\%$) at this temperature. With further increase of temperature, the martensite instability increases but the decrease in available metastable f_M (i.e. the available martensite to be induced) leads to rapid drop in f_{IA}. Above the T_{af} of $f_M(T,0)$, the f_{IA} becomes zero as no martensite phase is available ($f_M = 0$ and $f_{IA} = f_M(T,0)$) to be induced into austenite by the applied field or in another word the field has no effect, only temperature effects to follow. Considering same sequence of explanations, one can also interpret the behavior of f_{IA} curve at $\Delta H = 50$ kOe.

To find out the relation between the $f_{IA}(T,\Delta H)$ and the MR, we have calculated the MR from the already measured FCW $\rho(T,H)$ curves using the following equation $\Delta\rho/\rho_0 = [\rho(T,H) - \rho(T,0)]/\rho(T,0)$. Figure 6.3(a) represents the plot of MR (T,H) and $f_{IA}(T,\Delta H)$. We have observed a MR as large as 49% and 54% for the $\Delta H = 30$ and 50 kOe, respectively. It is evident from our study that the observed MR, for a given applied field, becomes maximum only when the $f_{IA}(T,\Delta H)$ is maximum. Now, bringing back to our previous arguments i.e. the large ΔT_{RM} under applied fields is an essential criteria to obtain a large MR across the transition region, can be understood by expressing the MR in terms of change in resistivity with temperature $(\frac{d\rho}{dT})$ across the phase transition and the field induced shift of the transformation temperature $(\frac{dT}{dH})$. Further, one can approximate the MR as, MR $\propto (\frac{d\rho}{dH}) = (\frac{d\rho}{dT})(\frac{dT}{dH})$. Thus, to observe a huge MR, both the factors have to be large and both factor is directly/indirectly related to the $f_{IA}(T,\Delta H)$. A plot describing the variation of MR with the f_{IA} for different ΔH (30 and 50 kOe) is shown in the inset of Figure 6.3(a). We also found that MR for the ascending and descending branch of f_{IA} follow different paths, producing a hysteresis in MR. This irreversibility in MR for the ascending and

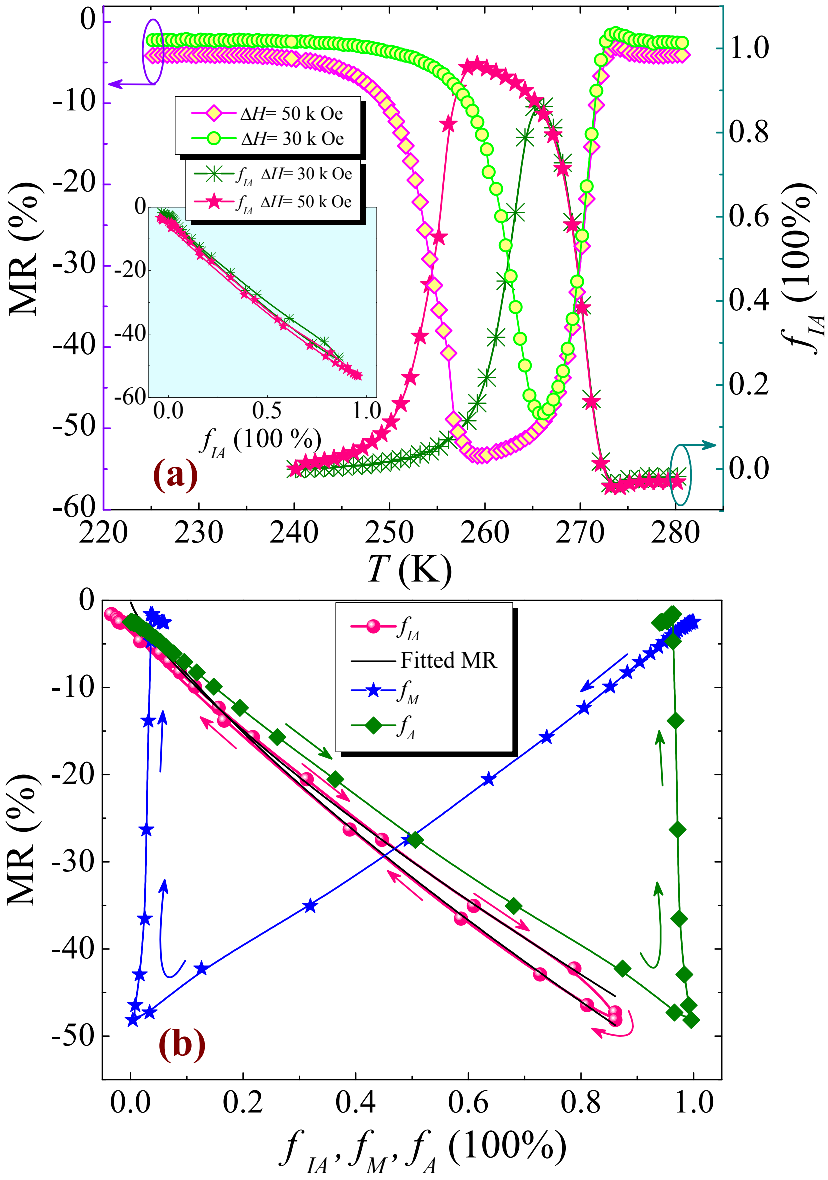

Figure 6.3: (a) Temperature variation of MR and f_{IA} for $\Delta H=$ 30, 50 kOe and inset shows the variation of MR with the f_{IA} for a given ΔH. (b) The variation of MR with the f_{IA}, f_M and f_A for $\Delta H=$ 30 kOe and the black solid curve has been obtained after fitting the MR using equation (6.4).

Table 6.1: The parameters are obtained from the fitting of MR vs f_{IA} curve using equation (6.4).

ΔH(kOe)	Branch	α	n
30	Ascending	50.9±1.06	0.76±0.02
30	Descending	54.8±1.59	0.78±0.05
50	Ascending	54.3±1.02	0.74±0.02
50	Descending	55.8±1.05	0.73±0.06

descending branches of f_{IA} can be understood by recalling Figure 6.2, there one can find that in the ascending branch of f_{IA} the initial phase fraction is stable martensite, while for the descending branch of f_{IA} the initial state is metastable martensite and austenite. Therefore, it is expected that resistivity and hence the MR would be different for two different branch of f_{IA}, due to presence of different amount of phase fractions. But, the fact which has been found more interesting is that the MR does not hold a linear relationship with the f_{IA}, instead it seems to follow a certain power law. To know the MR dependence on f_{IA} we have fitted the ascending and descending branch of f_{IA} with MR using the formula

$$\frac{\Delta\rho}{\rho_0} = -\alpha f_{IA}^{n} \tag{6.4}$$

where α defines the strength of MR. The obtained value of α and n for the ascending and descending branch of f_{IA} are listed in the table 6.1.

The Figure 6.3(b) shows the variation of MR with the f_{IA}, f_M and f_A for ΔH = 30 kOe. It can be seen that as the temperature increases (increasing direction of temperature is shown by the arrow), f_M starts to decrease while f_A increases due the significant increase of f_{IA} by the applied field, the MR

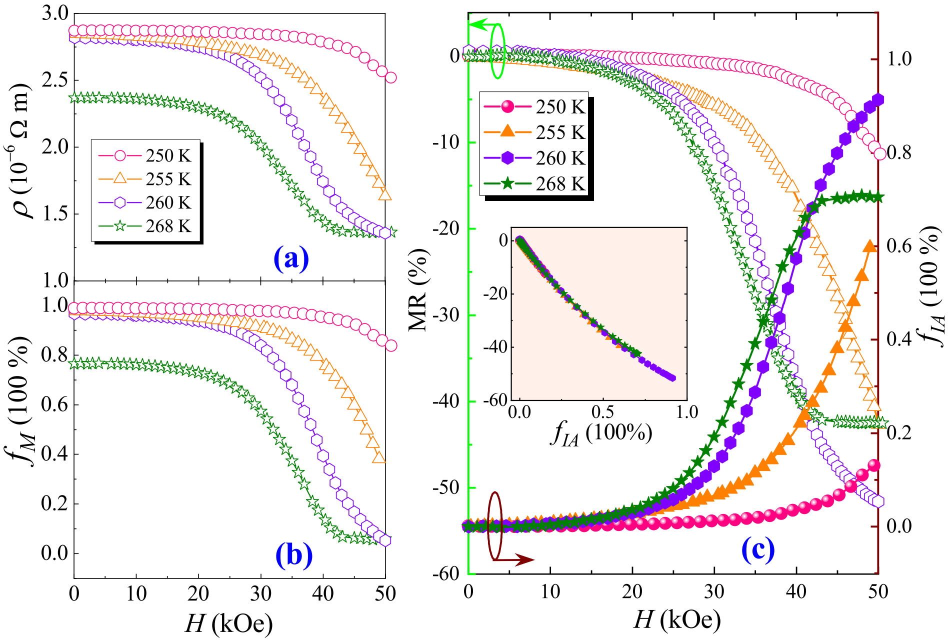

Figure 6.4: (a) $\rho(H)$ with increasing magnetic field upto 50 kOe at various temperatures across the MT region. (b) Extracted $f_M(H)$ curves at different temperatures from the $\rho(H)$ data. (c) The hollow data points represent the magnetic field variation of MR. The solid data points of similar hollow symbols and colours represent the corresponding $f_{IA}(H)$ curves.

also start to increase and attain maximum when the f_{IA} become maximum. Thereafter with the further increase of temperature, MR start to decrease as a consequence of decrease in f_{IA} (though the f_A remains constant: at maximum).

In an alternate way, the phase fractions induced MR behavior are also verified by measuring the isothermal $\rho(H)$ curves at several temperatures around the MT region, as shown in Figure 6.4(a). For this measurement, initially the sample was cooled from 350 K down to 10 K and warmed it back to the temperature of interest without applying any magnetic fields, then the $\rho(H)$ have been recorded by ramping the field 0→ 50 kOe. This protocol has been followed in order to measure the $\rho(H)$ curves at different temperatures. The extracted $f_M(T, H)$ curves from the $\rho(H)$ data have been represented in Figure 6.4(b). To construct the f_M and f_{IA} vs. H graphs from $\rho(H)$ isotherm data, the ρ value at 240 K from the $\rho(T)$ curve of $H = 0$ kOe have been taken as the ρ_M value (Figure 6.1(b)). Whereas, we have considered the ρ value near 261 K from the $\rho(T)$ curve at $H = 50$ kOe as the ρ_A value. The fact should be considered that the application of magnetic field induces austenite phase, and hence the ρ_A for a given field ($H =$ nonzero value) is slightly less than their zero field counterpart, i.e. ρ_A $(H = 0)$. Which means the system at $H = 50$ kOe is tending towards complete austenite phase than that at $H = 0$ kOe. Considering these, we think that the ρ_A value just above T_{af} (at 261 K) on the $\rho(T)$ curve for $H = 50$ kOe is better approximation for extraction of the $f_M(H)$ curves. Furthermore, for the $\rho(T)$ curve measured at $H = 0$ kOe during warming, the $T = 240$ K belongs to the martensite phase, and the resistivity below that temperature is increasing slightly due to various reasons (already discussed previously). So, choosing ρ value at $T = 240$ K on the $\rho(T, 0)$ curve as ρ_M is not going to alter our results/conclusions. Now, a similar explanation, as discussed previously to illustrate the MR(T) behaviour for a given ΔH, is also applicable for the field induced isothermal MR curves in Figure 6.4(c). The temperature $T = 250$ K belongs to the very deep inside of the martensite phase where the martensite phase is much more stable and therefore the resulting MR (-12%) is low and unsaturated for magnetic field of 50 kOe. The MR at this temperature matches fairly well with the same obtained from the $\rho(T)$ curves. As the temperature increases inside the MT region, the critical fields, need to convert the available less stable martensite to austenite, reduces and consequently the MR increases as a results of increase in f_{IA} but no ideal saturation in MR is observed until $T = 268$ K. Therefore, in support with our previous observations, we argue that the f_{IA} is the most important factor, which needs to be tuned to achieve large MR in this type of materials, as the resistivity of metallic martensite or austenite phase do not change significantly under application of magnetic field.

6.3 Structural evolution during MT

An additional evidence of the temperature dependent growth of martensite and austenite phases within the MT region is carried out by measuring the temperature dependent XRD using synchrotron radiation, in absence of magnetic field. In this measurement, a austenite peak (A (422)) at 47.3° and martensite peak (M (422)) around 49.4° are being probed to study the respective peak intensities as a function of temperature during cooling and warming cycle. The Figure 6.5(a) reveals the formation of martensite phase and depletion of austenite phase with cooling; while it is opposite in case of warming, as expected (Figure 6.5(b)). From this study, without being quantitative, we aimed to project the growth dynamics by measuring the intensity of respective austenite and martensite peak. A clear thermal hysteresis between the cooling and warming intensity of austenite (Figure 6.5(c)) and matensite peak (Figure 6.5(d)) are evident. Though a remaining martensite component has been found in the high temperature austenite region. This discrepancy may arises from the closeness of MT to the room temperature

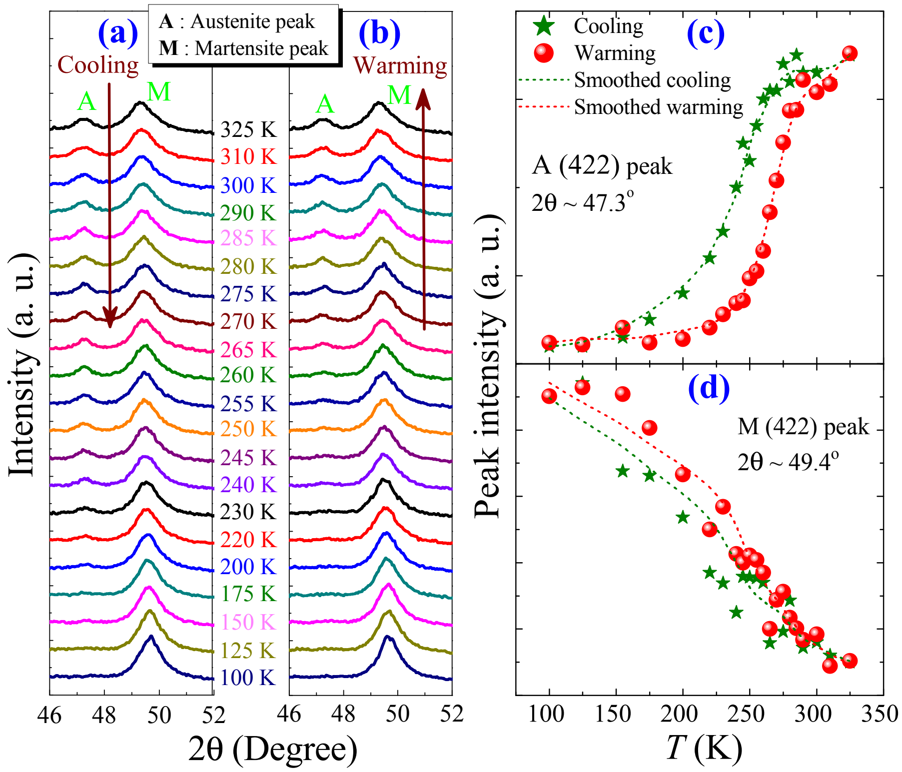

Figure 6.5: Temperature dependent XRD data while (a) cooling and (b) warming using synchrotron radiation ($\lambda = 0.9782$ Å). Normalized peak intensity with temperature of (c) Austenite (422) peak and (d) Martensite (422) peak.

and a preannealing before measuring the XRD could have removed such discrepancy. Therefore, the observed martensite transformation, evident from magnetization and resistivity data, can also be represented through the study of structural evolution with temperature, using temperature dependent XRD. The small deviation between resistivity and structural data (in form of the nature of separated austenite and martensite phases) perceived as the transition properties also depend on the extrinsic parameters such as, applied magnetic field, pressure, rate of heating and cooling, measurement protocols etc.

6.4 Chapter summarry

In this chapter, we have presented a detail estimation of the martensite, austenite and field induced austenite phase fractions within the MT region for a given temperature and field, determined from the $\rho(T)$ data with various field and isothermal $\rho(H)$ curves at different temperatures. The chapter also includes the discussions about the influence of different phase fractions on the observed MR. Our results reveal that the MR for a given field change (ΔH) attained maximum, only when the f_{IA} becomes maximum, and it becomes nearly independent on both the f_M and f_{PA}. Therefore, the f_{IA} has major contribution for the large MR than the other factors, though the f_{IA} at any particular temperature depends on the availability and instability of f_M at that temperature. It is also found that the MR does not hold a linear relationship with the f_{IA}, rather it follows a power law. Moreover its variation is not same for the ascending and descending branches of f_{IA}, i.e. does not follow the same power law, thus giving rise to hysteresis in MR. Furthermore, the temperature dependent XRD data supports the growth of austenite and martensite phases with temperature while warming and cooling, respectively, within the MT region of our studied compound.

Bibliography

[1] S. Blundell, Magnetism in Condensed Matter, Oxford University Press Inc., **2001**.

[2] C. Kittel, Introduction to solid state Physics. J. Wiley & Sons, Inc., eight edition **2005**.

[3] M. Getzlaff, Fundamentals of Magnetism, Springer.

[4] B. D. Cullity, Introduction to Magnetic Materials, IEEE Press, New Jersey, **2009**.

[5] S. Chikazumi, Physics of Ferromagnetism Oxford University Press, New York, **1997**.

[6] N. V. Volkenstein, V.P. Dyakina, and V.E. Startsev, Phys. Status Solidi B, **1973**, 57, 9.

[7] http://en.wikipedia.org/wiki/Bethe-Slater_curve.

[8] K. H. J. Buschow and F. R. de Boer, Physics of Magnetism and Magnetic Materials, Kluwer Academic Publishers, **2004**.

[9] E. Gratz and H.R. Kirchmayr, J. Magn. Magn. Mater., **1976**, 2, 187.

[10] A. Campbell, J. Phys. P: Metal Phys., **1972**, 2, L47-9.

[11] B. D. Cullity, and C. D. Graham, Introduction to magnetic material, A John wiley & sons, Inc.

[12] W.H. Meiklejohn, C.P. Bean, Phys. Rev., **1956**, 102, 1413.

[13] W.H. Meiklejohn, J. Appl. Phys., **1962**, 33, 1328.

[14] J. Nogues, I. K. Schuller, J. Mag. Mag. Mater., **1999**, 192, 203.

[15] C. H. Ho and C. H. Lai, IEEE Trans. Magn., **2006**, 42, 3069.

[16] X. H. Huang, J. F. Ding, G. Q. Zhang, Y. Hou, Y. P. Yao, and X. G. Li, Phys. Rev. B, **2008**, 78, 224408.

[17] Z. P. Li, C. W. Miller, I. V. Roshchin, and I. K. Schuller, Phys. Rev. B, **2007**, 76, 014423.

[18] K. OGrady , L. E. Fernandez-Outon, G. Vallejo-Fernandez, J. Mag. Mag. Mater., **2010**, 322, 883.

[19] C. Tsang, J. Appl. Phys., **1984**, 55, 2226.

[20] B. L*ü*thi, J. Mag. Mag. Mater., **1980**, 15, 1.

[21] J. Jensen, Rare earth magnetism and superconductivity, Lecture notes, University of Copenhagen, **2000**.

[22] J. M. D. Coey, Magnetism and magnetic materials, Cambridge University Press, New York, **2010**.

[23] K. R. Lea, M. J. M. Leask and W. P. Wolf, J. Phys. Chem. Solids, **1962**, 23, 1381.

[24] L.E. Reichl, A modern course in statistical mechanics, University of Texas press, Austin, **1980**.

[25] H. E. Stanley, Phase Transitions and Critical Phenomena, Oxford University Press,New York, **1971**.

[26] P. M. Chaikin, Principles of condensed matter physics Cambridge University Press, Cambridge, **1998**.

[27] V. K. Sharma, Study of magneto-structural transition and associated functional properties in the Ni-Mn-In/Sn alloys, Thesis, **2011**.

[28] R. M. White and T.H. Geballe , Long Range Order in Solids New York: Academic, **1979**.

[29] Y. Imry et al., Phys. Rev. B, **1980**, 19, 3580.

[30] S. B. Roy et al., Phase transit., **2004**, 77, 767.

[31] M. K. Chattopadhyay et al., Phys. Rev. B, **2003**, 68, 174404.

[32] K. H. J. Buschow, Rep. Prog. Phys., **1977**, 40, 1179.

[33] M. S. S. Brooks, Olle Eriksson, and Börje Johansson, J. Phys.: Condens. Matter, **1989**, 1, 5861.

[34] H. S. Li, Y. P. Li, and J. M. D. Coey, J. Phys.: Condens. Matter, **1991**, 3, 7277.

[35] W. E. Wallace, Prog. Rare Earth Sci. Technol., **1968**, 3, 1-37.

[36] H. Adachi and H. Ino, Nature (London), **1999**, 401, 148.

[37] H. Adachi, H. Ino, H. Miwa, Phys. Rev. B, **1997**, 56, R5744.

[38] K. A. Gschneidner, and V. K. Pecharsky, Rev. Mater. Sci., **2000**, 30, 387.

[39] B. F. Yu, Q. Gao, B. Zhang, X. Z. Meng and C. Chen, Int. J. of Refrig., **2003**, 26, 622.

[40] A. M. Tishin and Y. I. Spichkin, The magnetocaloric effect and its application, IOP Publishers, **2003**.

[41] Br̈uck E, J. Phys. D: Appl. Phys., **2005**, 38, R381.

[42] K. A. Gschneidner, V. K. Pecharsky, and A. O. Tsokol, Rep. Prog. Phys., **2005**, 68, 1479.

[43] N.A. de Oliveira, P.J. von Ranke, Phys. Rep., **2010**, 489, 89.

[44] E. Warburg, Ann. Phys., **1881**, 13, 141.

[45] P. Debye, Ann. Phys., **1926**, 81, 1154.

[46] W.F. Giauque, J. Am. Chem. Soc., **1927**, 49, 1864.

[47] V. K. Pecharsky et al., Phys. Rev. B., **2003**, 64, 144406.

[48] M. H. Phan et al., J. Magn. Magn. Mater, **2007**, 308, 325.

[49] V. K. Pecharsky et al., Rep. Prog. Phys., **2005**, 68, 1479.

[50] Verh. D. Deut. Phys, Gesel., **1903**, 5, 219.

[51] M. Khan, I. Dubenko, S. Stadler and Naushad Ali, Appl. Phys. Lett., **2007**, 91, 072510.

[52] K. Oikawa, W. Ito, Y. Imano, R. Kanuima, K. Ishida, S. Okamoto, O. Kitakami and T. Kanomata, Appl. Phys. Lett., **2006**, 88, 122507.

[53] Thorsten Krenke, M. Acet, E. F. Wassermann, X. Moya, Lluís Mañosa and A. Planes, Phys. Rev. B, **2006**, 73, 174413.

[54] V. K. Sharma, M. K. Chattophadhyay, K. H. B. Saheb, Anil Chouhan and S. B. Roy, Appl. Phys. Lett., **2007**, 89, 222509.

[55] M. K. Ray, K. Bagani, R. K. Singh, B. Majumdar and S. Banerjee, J. Appl. Phys., **2013**, 114, 123904.

[56] M. K. Ray, K. Bagani, P. K. Mukhopadhyay and S. Banerjee, Euro. Phys. Lett., **2015**, 109, 47006.

[57] M. K. Ray, B. Maji, M. Modak and S. Banerjee, Journal of Magnetism and Magnetic Materials, **2017**, 429, 110.

[58] M. K. Ray, B. Maji, K. Bagani and S. Banerjee, J. Phys.D: Appl. Phys., **2014**, 47, 385001.

[59] Thorsten Krenke, Seda Aksoy, Eyüp Duman, Mehmet Acet, Xavier Moya, Lluís Mañosa, and Antoni Planes, J. Appl. Phys., **2010**, 108, 043914.

[60] T. Krenke, M. Acet, E. F. Wassermann, X. Moya, L. Mañosa, A. Planes, Physical Review B, **2005**, 72, 014412.

[61] I. Babita, S. I. Patil, S. Ram, Journal of Physics D: Applied Physics, **2010**, 43, 205002.

[62] S. E. Muthu, N. V. R. Rao, M. M. Raja, D. M. R. Kumar, D. M. Radheep, S. Arumugam, Journal of Physics D: Applied Physics, **2010**, 43, 425002.

[63] Y. Sutou, Y. Imano, N. Koeda, T. Omori, R. Kainuma, K. Ishida, K. Oikawa, Applied Physics Letters, **2004**, 85, 4358.

[64] Sudip Kumar Sarkar, Sarita, P.D. Babu, Aniruddha Biswas, Vasudeva Siruguri, Madangopal Krishnan, Journal of Alloys and Compounds, **2016**, 670, 281-288.

[65] Ajaya K. Nayak, K. G. Suresh and A. K. Nigam, J. Phys. D: Appl. Phys., **2009**, 42, 035009.

[66] X. H. Chen, K. Q. Wang, P. H. Hor, Y. Y. Xue and C. W. Chu, Phys. Rev. B, **2005**, 72, 054436.

[67] M. Bersweiler, K. Dumesnil, F. Wilhelm, and A. Rogalev,Phys. Rev. B, **2013**, 88, 054411.

[68] K. Kanematsu, G. T. Alfieri, J. Phys. Soc. Japan, **1969**, 26, 244.

[69] G. F. Li, J. R. Su, C. F. Zhu, Appl. Phys. Lett., **2007**, 90, 172503.

[70] G. T. Alfieri, E. Banks, K. Kanematsu and T. Ohoyama, J. Phys. Soc. Japan, **1967**, 23, 507.

[71] B. Maji, K. G. Suresh, A. K. Nigam, Appl. Phys. Lett., **2011**, 98, 152506.

[72] J. W. Taylor, J. A. Duffy, A. M. Bebb, M. R. Lees, L. Bouchenoire, S. D. Brown, and M. J. Cooper, Phys. Rev. B, **2002**, 66, 161319R.

[73] M. Da Silva, K. Dumesnil, C. Dufour, M. Hehn, D. Pierre, D. Lacour, F. Montaigne, G. Lengaigne, and S. Robert, Appl. Phys. Lett., **2011**, 98, 232504).

[74] J.R. Su, C.F. Zhu, B. Wolf, M. Lang, Journal of Alloys and Compounds, **2007**, 431, 45.

[75] F.L. Pratta, S.J. Blundell, T. Lancaster, M.L. Brooks, C.A. Steer, H. Adachi, Physica B, **2006**, 374-375, 34.

[76] A. K. Grover, S. K. Malik, R. Vijayaraghavan and K. Shimizu, J. Appl. Phys., **1979**, 50, 7501.

[77] S. Venkatesh, Ulhas Vaidya, Veer Chand Rakhecha, S. Ramakrishnan and A. K. Grover, J. Phys.: Condens. Matter, **2010**, 422, 96002.

[78] S. S. Dhesi, G. van der Laan, P. Bencok, N. B. Brookes, R. M. Galra and P. Ohresser Phys. Rev. B, **2010**, 82, 180402R.

[79] H. Adachi, H. Kawata, H. Hashimoto, Y. Sato,2I. Matsumoto and Y. Tanaka, Phys. Rev. Lett., **2001**, 87, 127202.

[80] A. Avisou, K. Dumesnil, C. Dufour, J. Magn. Magn. Mater., **2007**, 316, 317.

[81] M. Ungureanu, K. Dumesnil,1 C. Dufour, N. Gonzalez, F. Wilhelm, A. Smekhova, and A. Rogalev, Phys. Rev. B, **2010**, 82, 174421.

[82] M. F. M. Din, J. L. Wang, Z. X. Cheng, S. X. Dou, S. J. Kennedy, M. Avdeev, S. J. Campbell, Sci. Rep., **2015**, 5, 11288.

[83] A. Szytula, Journal of Alloys and Compounds, **1992**, 178, 1-13.

[84] D. Gignoux, D. Schmitt, in Handbook of the Physics and Chemistry of Rare Earths, edited by K.A. Gschneidner Jr, L. Eyrings, Elsevier Science, **1995**, Vol. 20, Chap. 138, pp. 293-424.

[85] D. Gignoux, D. Schmitt, in Handbook of Magnetic Materials, edited by K.H.J. Buschow, North Holland, **1997**, Vol. 10, pp. 239-414.

[86] A. Blaise, R. Kmiec, B. Malaman, E. Ressouche, J.P. Sanchez , K. Tomala, G. Venturini, Journal of Magnetism and Magnetic Materials, **1994**, 135, 171.

[87] A. Garnier, D. Gignoux, B. Ouladdiaf, D. Schmitt and T. Shigeoka, Eur. Phys. J. B, **2000**, 16, 423-427.

[88] B. Maji, K. G. Suresh, and A. K. Nigam, Appl. Phys. Lett., **2013**, 102, 062406.

[89] B. Maji, M. K. Ray, K. G. Suresh, and S. Banerjee, J. Appl. Phys., **2014**, 116, 213913.

[90] T. Samanta, I. Das, and S. Banerjee, Appl. Phys. Lett., **2007**, 91, 152506.

[91] Vinh Hung Tran, Zbigniew Bukowski, J. Phys. Condens. Matter, **2014**, 26, 255602.

[92] S. Holtmeier, P. Haen, A. Lacerda, P. Lejay, J.L. Tholence, J. Voiron, J. Flouquet, Physica B, **1995**, 204, 250-254.

[93] R. Movshovich, T. Graf, D. Mandrus, J. D. Thompson, J. L. Smith, and Z. Fisk, Phys. Rev. B, **1996**, 53, 8241.

[94] Gernot W. Scheerer, Zhi Ren, Gerard Lapertot, Gaston Garbarino, Didier Jaccard, Physica B, **2018**, 536, 150154.

[95] F.M. Grosche, S.R. Julian, N.D. Mathur, G.G. Lonzarich, Physica B, **1996**, 223 & 224, 50-52.

[96] J. Budzioch, A. Jezierski, V. Ivanov, B. Penc and A. Szytu, J. Phys.: Condens. Matter, **1999**, 11, 8069.

[97] M. Slaski, A. szytula, J. Leciejewicz, A. Zygmunt, Journal of Magnetism and Magnetic Materials, **1984**, 46, 114.

[98] A. Szytula, J. Leciejewicz;Journal of Magnetism and Magnetic Materials, **1989**, 80, 200.

[99] V.K. Pecharsky, K.A. Gschneidner Jr., Phys Rev. Lett., **1997**, 78, 4494.

[100] F.X. Hu, B.G. Shen, J.R. Sun, Z.H. Cheng, G.H. Rao, X.X. Zhang, Appl. Phys. Lett., **2001**, 78, 3675.

[101] A. Fujita, S. Fujieda, Y. Hasegawa, K. Fukamichi, Phys Rev. B, **2003**, 67, 104416.

[102] J. Lyubina, K. Nenkov, L. Schultz, O. Gutfleisch, Phys Rev. Lett., **2008**, 101, 177203.

[103] A. Yan, K.H. Mller, L. Schultz, O. Gutfleisch, J. Appl. Phys., **2006**, 99, 08K903.

[104] O. Tegus, E. Brck, K.H.J. Buschow, F.R. de Boer, Nature, **2002**, 415, 150.

[105] M. Modak. B. Maji, S. Mondal, M.K. Ray, S. Banerjee, Physica B: Condensed Matter, **2019**, 572, 195198.

[106] S.B. Gupta, K.G. Suresh, Appl. Phys. Lett., **2013**, 102, 022408.

[107] B. Maji, M.K. Ray, K.G. Suresh, S. Banerjee, J. Appl. Phys., **2014**, 116, 213913.

[108] L. Li, B. Saensunon, W.D. Hutchison, D. Huo, K. Nishimura, J. Alloys Compd., **2014**, 582, 670.

[109] L. Li, Y. Yuan, Y. Zhang, T. Namiki, K. Nishimura, R. Potgen, S. Zhou, Appl. Phys. Lett., **2015**, 107, 132401.

[110] Ling-Wei Li, Chin. Phys. B, **2016**, 25, 037502.

[111] Y. Zhang, L. Hou, Z. Ren, X. Li, G. Wilde, J. Alloys Compd., **2016**, 656, 635639.

[112] Y. Yang, Y. Zhang, X. Xu, S. Geng, L. Hou, X. Li, Z. Ren, G. Wilde, J. Alloys Compd., **2017**, 692, 665669.

[113] A. Chaturvedi, S. Stefanoski, M.H. Phan, G.S. Nolas, H. Srikanth, Appl. Phys. Lett., **2011**, 99, 162513.

[114] R. Caballero-Flores, V. Franco, A. Aonde, K.E. Knipling, M.A. Willard, Appl. Phys. Lett., **2011**, 98, 102505.

[115] L. Li, M. Kadonaga, D. Huo, Z. Qian, T. Namiki, K. Nishimura, Appl. Phys. Lett., **2012**, 101, 122401.

[116] L. Li, T. Namiki, D. Huo, Z. Qian, K. Nishimura, Appl. Phys. Lett., **2013**, 103, 222405.

[117] L. Li, O. Niehaus, M. Kersting, R. Pttgen, Appl. Phys. Lett., **2014**, 104, 092416.

[118] V. K. Sharma, M. K. Chattophadhyay and S. B. Roy, Phys. Rev. B, **2007**, 76, 140401(R).

[119] S. Chatterjee, S. Giri, S. Majumdar and S. K. De, J. Phys. D: Appl. Phys., **2009**, 42, 065001.

[120] T. Chabri, A. M. Awasthi, Kartik C. Ghosh, A. Venimadhav and T. K. Nath, Mater. Res. Express, **2018**, 5, 086511.

[121] D. H. Wang, C. L. Zhang, Z. D. Han, H. C. Xuan, B. X. Gu, and Y. W. Du, J. Appl. Phys., **2008**, 103, 033901.

[122] T. Chabri, A. Venimadhav, T. K. Nath, Journal of Magnetism and Magnetic Materials, **2018**, 466, 385.

[123] H. C. Xuan, Y. Deng, D. H. Wang, C. L. Zhang, Z. D Han and Y. W. Du, J. Phys. D: Appl. Phys., **2008**, 41, 215002.

[124] S. Chatterjee, S. Giri and S. Majumdar, Phys. Rev. B, **2008**, 77, 012404.

[125] S. Chatterjee, S. Giri, S. Majumdar and S. K. De, Phys.Rev. B, **2008**, 77, 224440

[126] J. M. Barandiaran, V. A. Chernenko, P. Lazpita, J. Gutierrez and J. Feuchtwanger, Phys. Rev. B, **2009**, 80, 104404.

[127] M. Modak, M. K. ray, S. Mondal, B. Maji, M. K. Ray K. Bagani, A. Bhattacharyya and S. Banerjee, J. Phys. D: Appl. Phys., **2020**, 53, 205301.

[128] Users Manual, Tri-arc Furnace Model 5TA (Centorr Vacuum Industries, USA).

[129] A. J. Dekkar, Solid State Physics, Prentice-Hall, **1957**.

[130] N. W. Ashcroft and N. D. Mermin, Solid State Physics, Holt, Rinehart and Winston, **1987**.

[131] J. I. Goldstein, *et al.*, Scanning Electron Microscopy and X-Ray Microanalysis, Springer, **2003**.

[132] J. D. Jackson, Classical electrodynamics, John Willy and Sons, Singapur, **1999**.

[133] S. Foner, Rev. Sci. Instrum., **1959**, 30, 548.

[134] M. McElfresh, Fundamentals of Magnetism and Magnetic Measurements, Quantum Design, **1994**.

[135] J. Clarke, A. I. Braginski, The SQUID Handbook Vol. I & II , Wiley-VCH, **2006**.

[136] Quantum Design. SQUID-VSM Options Manual.

[137] L. J. Vanderpauw et al., Philips Res. Repts., **1961**, 16, 187.

[138] B.F. Woodfield et al., Phys. Rev. Lett., **1997**, 78, 3201.

[139] J. S. Hwang et al. Rev Sci Instrum., **1997**, 68, 94.

[140] Quantum Design, PPMS AC Transport Option Users Manual

[141] Quantum Design, PPMS Thermal Transport Option Users Manual

[142] L. Li, W. D. Hutchison, D. Huo, T. Namiki, Z. Qian, K. Nishimura, Scripta Materialia, **2012**, 67, 237-240.

[143] J.C. Debnath, J. Wang, Intermetallics, **2016**, 78, 50-54.

[144] Y. Ma, X. Dong, Y. Qi, L. Li, Journal of Magnetism and Magnetic Materials, **2019**, 471, 25-29.

[145] V.K. Pecharsky, K.A. Gschneidner Jr., J. Appl. Phys., **1999**, 86, 565.

[146] L. Li, K. Nishimura, J. Appl. Phys., **2009**, 106, 023903.

[147] R. Rawat, I. Das, J. Phys.: Condens. Matter, **2001**, 13, L57.

[148] A.O. Pecharsky, Yu. Mozharivskyj, K.W. Dennis, K.A. Gschneidner Jr., R.W. McCallum, G.J. Miller, V.K. Pecharsk, Phys. Rev. B, **2003**, 68, 134452.

[149] Q. Zhang, X.G. Liu, F. Yang, W.J. Feng, X.G. Zhao, D.J. Kang, Z.D. Zhang, J. Phys. D: Appl. Phys., **2009**, 42, 055011.

[150] Q. Zhang, J.H. Cho, J. Du, F. Yang, X.G. Liu, W.J. Feng, Y.J. Zhang, J. Li, Z.D. Zhang, Solid State Commun., **2009**, 149, 396.

[151] Q. Zhang, J.H. Cho, B. Li, W.J. Hu, Z.D. Zhang, Appl. Phys. Lett., **2009**, 94, 182501.

[152] Y. Zhang, D. Guo, Y. Yang, S. Geng, X. Li, Z. Ren, G. Wilde, J. Alloys Compd., **2017**, 702, 546550.

[153] Y. Zhang, D. Guo, Y. Yang, J. Wang, S. Geng, X. Li, Z. Ren, G. Wilde, Intermetallics, **2017**, 88, 6164.

[154] L. Li, D. Huo, K. Su, R. Pöttgen, Intermetallics, **2018**, 93, 343.

[155] L. Li, K. Nishimura, G. Usui, D. Huo, Z. Qian, Intermetallics, **2012**, 23, 101.

[156] T. Chabri, A. Ghosh, Sunil Nair, A. M. Awasthi, A. Venimadhav and T. K. Nath, J. Phys. D: Appl. Phys., **2018**, 51, 195001.

[157] A. K. Nayak ,K. G. Suresh and A. K. Nigam, Acta. Mater., **2011**, 59, 3304.

[158] V. K. Sharma, M. K. Chattopadhyay and S. B. Roy, Phys. Rev. B, **2007**, 76, 140401(R).

[159] V. V. Khovaylo, T. Omori, E. Endo, X. Xu, R. Kainuma, A. P. Kazakov, V. N. Prudnikov, E. A. Ganshina, A. I. Novikov, Y. O. Mikhailovsky, D. E. Mettus and A. B. Granovsky, Phys. Rev. B, **2013**, 87, 174410.

[160] Rolf Landauer, Journal of Applied Physics, **1952**, 23, 779.